THE EXCITATION OF ISOVECTOR GIANT RESONANCES VIA THE ^{60}Ni(^{3}He, t) REACTION AT 140 MEV/U

By

Felix Ndayisabye

A DISSERTATION

Submitted to
Michigan State University
in partial fulfillment of the requirements
for the degree of

Physics—Doctor of Philosophy

2024

ABSTRACT

Nuclear charge-exchange reactions at intermediate energies are powerful probes of the isovector response of nuclei. They provide an opportunity to study isovector giant resonances, such as the Gamow-Teller resonance and the isovector giant monopole and dipole resonances. The properties of these giant resonances provide important insights into the bulk properties of nuclear matter and have important implications for neutrino and astrophysics. In this work, the focus is on the investigation of the properties of isovector giant resonances excited via the ^{60}Ni(^{3}He,t) reaction at 140 MeV/u up to excitation energies of 60 MeV to study the Gamow-Teller resonance, isobaric analog state, isovector (spin) monopole, dipole, and quadrupole giant resonances.

The (^{3}He,t) reaction was used as an isovector probe to investigate the properties of isovector giant resonances in ^{60}Cu. To investigate these isovector giant resonances, the analysis was done through a multiple decomposition analysis (MDA). The differential cross sections were fitted with a linear combination of the distorted wave Born approximation (DWBA) angular distributions associated with different angular momentum transfer ΔL. The angular distributions were calculated in DWBA by using the code package FOLD code. Different giant resonances were seen at different excitation energies. The results were compared with shell-model, and normal-mode calculations.

It was found that the Gamow-Teller strengths extracted from the experiment could be reproduced reasonably well by the shell-model calculations. The extraction of the isovector dipole and monopole resonances was complicated by the presence of the quasi-free continuum. A detailed extraction of the isovector monopole resonances was not possible. For isovector dipole resonance, a reasonable consistency was found with the normal-mode calculations, after applying a simple estimate for the contributions from the quasifree continuum.

Overall, this work provides valuable insights into the properties of isovector giant resonances, highlights the importance of continuum subtraction, and provides a detailed analysis of the (^{3}He,t) reaction for probing these resonances at high excitation energies.

This thesis is dedicated to my parents, who have been a constant source of love and support despite their distance, and to my uncle Pius MASUMBUKU, whose inspiration has shaped me into the person I am today.

"Ikivi cyawe ndacyushije ukiriho"

ACKNOWLEDGEMENTS

The completion of this Ph.D. journey was made possible through standing on the collective shoulder of giants. I've been incredibly fortunate to have the backing of colleagues, friends, family, and my church community throughout my graduate studies at Michigan State University, within the Department of Physics and Astronomy, and particularly at the Facility for Rare Isotope Beams (FRIB). The graduate school presented numerous challenges, both academic and personal, as I balanced my roles as a student, parent, and father of two wonderful children, Abia Curie ILISA (7 years old) and Happy Austin TUZO (4 years old). I owe an immense debt of gratitude to all those who helped me navigate this journey.

First and foremost, I would like to give a special and wholehearted appreciation to my advisor, **Remco Zegers**. Your support, guidance, and unwavering encouragement have been instrumental throughout this research endeavor. Your mentorship has been the cornerstone of my academic journey, and I deeply value the dedication you've shown. I'll always remember your daily check-ins and your willingness to respond to emails, even during weekends and late nights. I'll always remember your evening visits to my desk before you go home with words of encouragement and were truly uplifting. Thank you for accepting me as one of your mentees, irrespective of my background, and for allowing me to prioritize my family during challenging times. Your support and advocacy will forever hold a special place in my heart. I am equally grateful to the members of my thesis committee, Paul Gueye, Filomena Nunes, Danny Caballero, and Tyce DeYoung, for your invaluable guidance, insightful discussions, questions, and feedback during our yearly meetings, which significantly enriched the quality of this work.

Special thanks are owed to Pawel Danielewicz, Scott Pratt, and Kirsten Tollefson for your unwavering efforts in securing my admission to the Department of Physics and Astronomy at Michigan State University. It was not easy due to VISA issues, but you made it possible. I'll never forget the dedication and training I received from Pawel Danielewicz during my first semester at MSU.

My gratitude extends to all past and current members of the FRIB charge-exchange (CE) group,

including R. G. T. Zegers, D. Bazin, S. Noji, J. Pereira, C. J. Zamora, S. Giraud, A. Mustak, J. Schmitt, C. Maher, Z. M. Rahman, and J. Rebenstock. Special thanks to Shumpei, Juan, and Simon for your invaluable contributions to graduate and undergraduate students in the CE group during our weekly research group meetings and for patiently addressing our questions. To J. Schmitt, thank you for your friendly assistance and guidance regarding DWBA input parameters during your time in the CE group. The list of appreciations goes on, but a special mention to C. Maher for creating the initial Python code to run MDA files; it proved immensely helpful in my analysis processes.

I am profoundly grateful to Mornetka Guèye, Paul Guèye, and Rachel Younger, whose unwavering support has extended far beyond the academic realm. They have not only been pillars of strength in my scholarly pursuits but have also provided invaluable emotional and social support to both my family and myself during the extraordinary challenges we've confronted in dealing with my wife's critical health condition during my academic journey.

I'd like to express my sincere gratitude to the Professors and instructors who guided me throughout my Ph.D. studies, including Michael Thoennessen (my first Advisor at NSCL/FRIB), Daniel Bazin (Master's Advisor), Vladimir Zelevinsky, Mohammad Maghrebi, Luke Robert, Andreas Von Manteuffel, Witold Nazarewicz, Yamazaki Yoshishige, Danny Caballero, Filomena Nunes, Alex Brown, Carlo Piermarocchi, Artemis Spyrou, David J. Morrissey, and Sean Liddick.

A special note of appreciation goes to the dedicated staff in the Department of Physics and Astronomy, with a heartfelt thank you to Kim Crosslan and her exceptional team. Your unwavering support, and treating students like your own, have been truly remarkable. I'm also grateful to the entire team at FRIB, where I've had the privilege to learn. I extend my gratitude to FRIB lab directors, Thomas Glasmacher and Brad Sherrill, and Heiko Hergert, for their exceptional leadership in creating a safe and enriching scientific environment that operates around the clock. I'm also appreciative of the financial assistance I received from both FRIB and the Department of Physics and Astronomy during the challenging times I encountered. The financial support from the U.S. National Science Foundation Grant No: PHY-2209429, Windows on the Universe: Nuclear Astrophysics at FRIB, greatly contributed to making this work possible.

I acknowledge the bridge connection between the African Institute for Mathematical Sciences (AIMS) and MSU, specifically at FRIB, which paved the way for my Ph.D. pursuit. Lastly, I want to express my deep appreciation to the members of the Spartan Chapter of NSBP at MSU; you've been an essential part of my journey, and I'm proud to have been a member. My heartfelt thanks also go to my fellow graduate students, officemates, and friends who provided invaluable support along the way, including Pierre Nzabahimana, Chi-En (Fanurs) Teh, Timilehin Ogunbeku, Yani Udiani, Jean Pierre Twagirayezu, Sylvester Agbemava, Linda H'lophe, Avik Sarkar, and anyone reading this message! Your support has meant the world to me. To all the friends I met during this journey, their company means a lot to me. **THANK YOU!**.

TABLE OF CONTENTS

CHAPTER 1

INTRODUCTION

1.1 Motivation

Charge-exchange (CE) reactions involve the exchange of charge between a target nucleus and a nucleus of the incoming beam. CE reactions studies at intermediate beam energies ($\sim$ 100 MeV/u) provide insight into isovector excitations, and isovector giant resonances in particular. These CE reactions are associated with a change in isospin ($\Delta T = 1$). By selecting specific types of CE reactions, such as (n,p) or (p,n)-type CE reactions, one can define the projection of the isospin quantum number as $T_z = \pm 1$. A variety of excitations, associated with the transfer of different units of angular momentum and spin, can be probed. Measurements of the properties of isovector giant resonances are of interest for a variety of reasons:

- The experimental data can be used to test microscopic models of nuclei up to high excitation energies and, therefore, test the underlying assumptions made for these models [1].

- The characteristics of isovector giant resonances are also useful to constrain macroscopic properties of nuclei and nuclear matter. In particular, isovector giant resonances are associated with out-of-phase oscillations of the proton and neutron "fluids" inside the nucleus. Therefore, experimental data constrains the restoring forces when neutrons and protons are displaced relative to each other and thus provide insight about asymmetric nuclear matter.

- The microscopic and macroscopic properties of isovector giant resonances have interesting applications. For example, the properties of allowed and forbidden isovector transitions play important roles in nuclear astrophysics and neutrino physics, as they determine stellar reaction roles mediated by the weak interaction. In additions, macroscopic properties of the isovector giant resonances reveal properties of the nuclear equation of states, with implications for stellar phenomena such as neutron stars.

Experimentally, there are few data sets where spectra are obtained up to high excitation energies.

The motivation behind the present work is to investigate the ^{60}Ni(^{3}He,t) reaction at 140 MeV/u up to excitation energies of 60 MeV to study the:

- Gamow-Teller Resonance and Isobaric Analog State,
- Isovector (spin) monopole resonances,
- Isovector (spin) dipole resonances.

1.2 Thesis Organization

This work is divided into 6 chapters. Chapter 2 provides an overview of both microscopic and macroscopic perspectives on giant resonances. It discusses the isospin structure of nuclei and its significance in the isovector response. The chapter delves into the properties of isovector giant resonances as they serve as tests of the microscopic model of nuclei at high excitation energies. Additionally, it introduces the hydrodynamic model of giant resonances as a macroscopic model describing a nucleus as a liquid drop of the proton and neutron fluids oscillating in different modes around its equilibrium shape. The chapter further explores isovector giant resonances within the charge-exchange spectrum. and concludes with an overview of the charge-exchange reaction probes.

Chapter 3 discusses a brief overview of the theoretical tools used to extract information about charge-exchange (CE) excitations and the properties of the isovector giant resonances using the distorted wave Born approximation in the code package FOLD. A brief overview of the Eikonal approximation and the unit cross section for GT and IAS will be discussed in this chapter.

Chapter 4 provides an overview of the experimental setup and procedures used to investigate isovector giant resonances in ^{60}Ni up to excitation energy of 60 MeV by using the (^{3}He,t) reaction at 140 MeV/u. The experiment was performed with the Grand Raiden Spectrometer (GRS) at the Research Center for Nuclear Physics (RCNP) in Osaka University. Furthermore, this chapter describes the procedures used to extract the differential cross sections from the three rigidity settings (low, medium, and high) of the GRS.

Chapter 5 presents the results from the multiple decomposition analysis (MDA), where the spectra were decomposed into contributions from resonances with different angular momentum

transfers. It shows the location of the isovector giant resonances investigated via the ^{60}Ni(^{3}He, t) reaction. This chapter details the findings for the Gamow-Teller strength, B(GT), and the study of the B(GT) for the T_0 + 1 states at 14.4 MeV and above in ^{60}Cu, compared with known T_0 + 1 states from ^{60}Ni(p, p') and ^{60}Ni(e, e') reactions. It elucidates the techniques for subtracting a quasifree-continuum from the measured data. It underscores the significance of the continuum subtraction. Finally, it delves into the extraction of isovector spin giant monopole and dipole strengths. Comparisons with theoretical calculations are made

Chapter 6 marks the conclusion of the thesis with a general summary and future outlook.

CHAPTER 2

GIANT RESONANCES

2.1 Definitions and Classification of the Giant Resonances

2.1.1 Microscopic View of the Giant Resonances

In the microscopic picture, giant resonances are described as a coherent superposition of one-particle one-hole (1p-1h) transitions excited from the ground state[2, 1], where the particle is a proton (neutron), and the hole is neutron (proton). Charge-exchange reactions are associated with the transfer of isospin ($\Delta T = 1$). The projection of the isospin quantum number (ΔT_z) can be lowered ($\Delta T_z = -1$) or raised ($\Delta T_z = +1$) in the (p, n) or (n, p)- type charge-exchange reactions, respectively. This is illustrated in Figure 2.1. The transitions to excited states from the ground state for a certain giant resonance are characterized by the operator O^{μ}_{JM} [3]:

$$O^{\mu}_{JM} = r^{\lambda}[\overrightarrow{\sigma} \otimes \overrightarrow{Y_L}]^{J}_{M}\tau_{\mu} \tag{2.1}$$

where J is the total angular momentum transfer ($\overrightarrow{J} = \overrightarrow{L} + \overrightarrow{S}$) and M is the projection of J, L is the orbital angular momentum transfer, λ defines the radial operator and is defined by $\lambda = \Delta L + 2\Delta n$, where ΔL is the orbital angular momentum transfer, and n is the change in the major oscillator for transition. If the excitation goes across a major oscillator shell, λ will be increased by 2. This is, for example, the case for the isovector giant monopole resonance (IVGMR) and its spin-transfer partner, the isovector spin-transfer giant monopole resonance (IVSGMR). $\overrightarrow{Y_L}$ is the spherical harmonic associated with L, $\overrightarrow{\sigma}$ is the spin-transfer operator, and τ is the isospin operator, with $\mu = \pm 1$ for charge-exchange reactions, where μ is the isospin projection.

The total transition strength is constrained by the most coherent superposition of the particle-hole excitations associated with a specific one-body operator as described through [1, 3, 4, 5, 6, 7]. The strength function described the response of a nucleus to an arbitrary one-body operator O connecting the ground state of a nucleus to the excited states:

$$S_O = \sum_{f} \left|\langle \Phi_f | O | \Phi_i \rangle\right|^2 \delta(E_f - E_i) \quad \text{MeV} \tag{2.2}$$

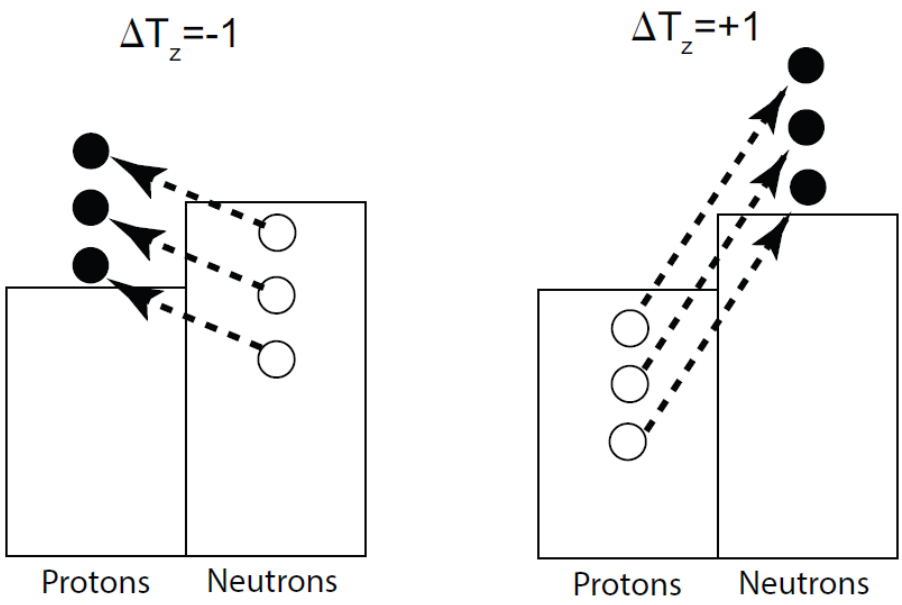

Figure 2.1 Schematic representation of collective one-particle one-hole (1p-1h) excitations of the isovector giant resonances for $\Delta T_z = -1$ reactions (e.g., (p,n), (^{3}He,t)) (left) and $\Delta T_z = +1$ reactions (e.g., (n,p), (t,^{3}He)) (right). The arrows correspond to a constructive contribution from each p-h component. Figure taken from [3].

where $|\Phi_i\rangle$ and $|\Phi_f\rangle$ stands for the ground (i) and final (f) states respectively. For continuum states, the sum turns into an integral.

2.1.2 Macroscopic View of the Giant Resonances

In the macroscopic picture, giant resonances are defined as a collective motion of nucleons involving many if not all the particles in the nucleus, causing density oscillations in the proton and neutron nuclear fluids [8]. Such collective oscillations are categorized into two types: isoscalar ($\Delta T = 0$) if the proton and neutron fluids oscillate in-phase, and isovector ($\Delta T = 1$), if they oscillate out-of-phase. In addition, the collective motion can be associated with spin. If nucleons with opposite spin oscillate in phase the resonances are referred to as electric ($\Delta S = 0$). If nucleons with opposite spin oscillate out-of-phase, the oscillations are referred to as magnetic ($\Delta S = 1$). They are depicted schematically in Figure 2.2. In this work, we will focus on the isovector giant resonances. Table 2.1 lists the acronyms used to describe these resonances in this thesis, although other variations exist (for example, the acronym SDR can represent the IVSGDR). The table also includes the relevant quantum numbers for each of these giant resonances. The list of isovector giant

resonances in Table 2.1 can be extended to resonances of higher multipolarity, but identifying such excitations is difficult since they are situated on top of the continuum background and their angular distributions are not very distinctive. The IAS and GTR cannot be associated with a hydrodynamic motion as there is no radial component to the operator ($r^{\lambda} = 1$).

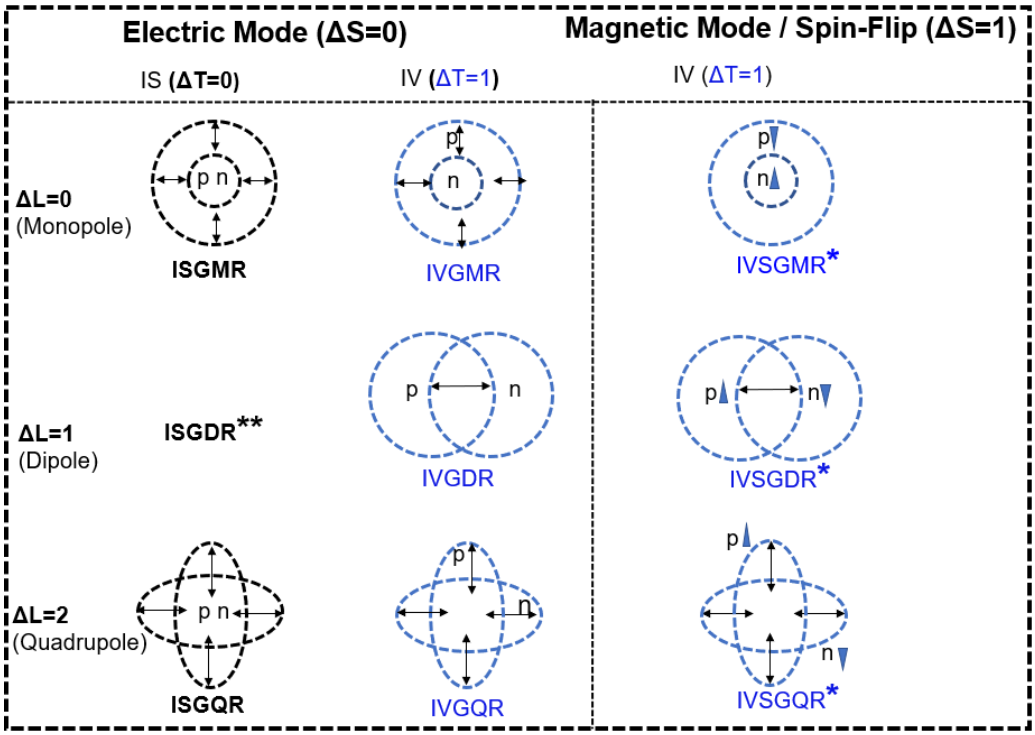

Figure 2.2 Schematic of the macroscopic depiction of giant resonance modes. The symbols p and n represent proton and neutron fluids, and the small triangles indicate spin direction and refer to either up or down. The arrows show the direction of motion of the fluid components. Single asterisks indicate resonances for which a second contribution exists in which spin directions are reversed. The double asterisk indicates that this resonance does not exist in first order. The figure was modified from Ref [3].

Table 2.1 Overview of the isovector giant resonances and their quantum numbers. ΔT stands for isospin-transfer, ΔL for angular momentum, ΔS for spin, ΔJ for total angular momentum transfer ($\Delta J = \Delta L + \Delta S$), and π for the charge in parity. If the charge-exchange reaction is associated with angular momentum and spin transfer, the excited giant resonance has several components with different total spins. Δn is the change in the major oscillator shell, and $\Delta\lambda = \Delta L + 2\Delta n$.

Transition name	ΔT	ΔL	ΔS	ΔJ^π	Δn	$\Delta\lambda(\hbar w)$
Fermi/Isobaric Analog State (Fermi/IAS)	1	0	0	0^+	0	0
Gamow-Teller Resonance (GTR)	1	0	1	1^+	0	0
Isovector Giant Monopole Resonance (IVGMR)	1	0	0	0^+	1	2
Isovector Spin Giant Monopole Resonance (IVSGMR)	1	0	1	1^+	1	2
Isovector Giant Dipole Resonance (IVGDR)	1	1	0	1^-	0	1
Isovector Spin Giant Dipole Resonance (IVSGDR)	1	1	1	$(0,1,2)^-$	0	1
Isovector Giant Quadrupole Resonance (IVGQR)	1	2	0	2^+	0	2
Isovector Spin Giant Quadrupole Resonance(IVSGQR)	1	2	1	$(1,2,3)^+$	0	2

2.2 Isospin Picture

The symmetry between protons and neutrons can be described by using the isospin operator **t**, which is a vector quantity that behaves identically to the ordinary spin vectors. The protons are defined as having isospin projection $t_z = -1/2$, while neutrons have $t_z = +1/2$. The total isospin **T** of a nucleus is the vector sum of the isospins of its constituent nucleons ($\mathrm{T} = \sum_{\mathrm{t=i}}^{\mathrm{A}} \mathrm{t_i}$) [9]. The isospin projection T_z, calculated by $T_z = \frac{N-Z}{2}$ can be positive, for $N > Z$, or negative, for $N < Z$. The value of T_z determines the states that can be populated in the daughter nucleus. The concept of isospin is key for describing charge-exchange reactions as isovector probes. There are two types of charge-exchange reactions. The first one is β^--type or (p,n)-type, for which the change in isospin projection $\Delta T_z = -1$. In the $\Delta T_z = -1$ direction, for nuclei with $N > Z$, states in residual nucleus (with $T_z = T_0 - 1$, where T_0 is the ground state isospin of another nucleus i.e. ground state of the target nucleus) with isospin $T_0 - 1$, T_0, and $T_0 + 1$ can be populated. The second one is β^+-type or (n,p)-type charge-exchange reaction. For nuclei with $N > Z$ states in the residual nucleus (with $T_z = T_0 + 1$) have isospin $T_0 + 1$; this occurs because the minimum isospin in the residual nucleus is equal to T_z. This is shown in Figure 2.3. Here we focus on (^{3}He,t) reactions, which are of β^--type or (p,n)-type. It is possible to write the transition strength to the final states in terms of reduced matrix elements for which the dependence on isospin quantum numbers is made explicit. These isospin factors are $\frac{1}{(2\mathrm{T_0}+1)(\mathrm{T_0}+1)}$ for final states with isospin $T_0 + 1$, $\frac{1}{T_0+1}$ for final states with isospin

T_0 and $\frac{2T_0-1}{2T_0+1}$ for states with final isospin of $T_0 - 1$. In the case of ^{60}Ni, the isospin of the target nucleus is 2, and the isospin weights are $\frac{1}{15}$, $\frac{1}{3}$ and $\frac{3}{5}$ for final states with isospin $T_0 + 1$, T_0 and $T_0 - 1$, respectively.

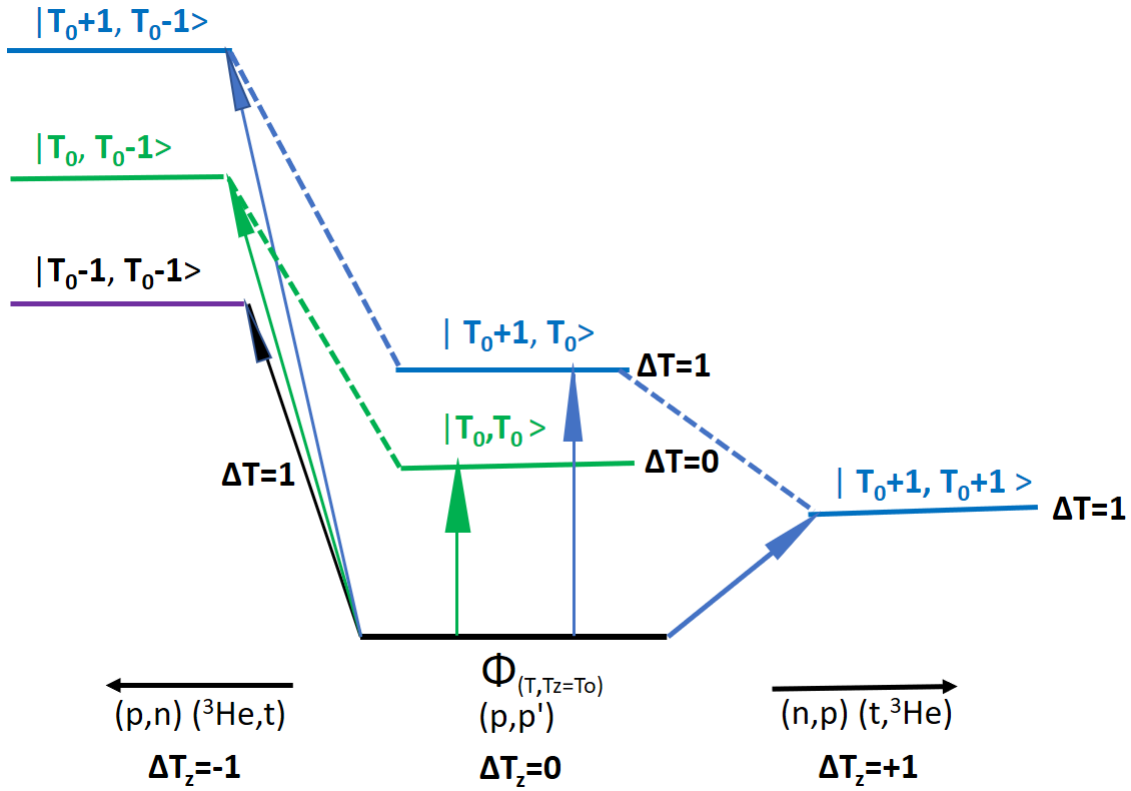

Figure 2.3 Schematic depiction of the isospin scheme associated with charge-exchange reactions for the excited states in both (p,n) and (n,p) directions. The dotted lines indicate the analog states and the arrows show the possible transitions. For charge-exchange reactions with $N = Z$ ($T = T_z = 0$) nuclei, only final states with $T = 1$ can be populated in both $\Delta T_z = \pm 1$ directions. Figure modified from Ref [3].

As discussed for the IAS (section 2.3.1), because of isospin symmetry, analogs of states with the same isospin can be found in isobaric nuclei. Besides the analog of the ground states, other states can have analogs as well. This is illustrated in Figure 2.4. $\Delta T_z = -1$ charge-exchange reactions on a target nucleus with isospin T_0 will populate states with $T_0 - 1$, T_0, and $T_0 + 1$. States with isospin T_0, and $T_0 + 1$ have analogs in the target nucleus. These analogs can be populated through inelastic scattering reactions. States with isospin $T_0 + 1$ have analogs in the nucleus that can be reached through $\Delta T_z = +1$ charge-exchange reactions. Hence, in principle, it is possible to learn about the

$T_0 + 1$ states by performing $\Delta T_z = +1$ and $\Delta T_z = -1$ charge-exchange reactions. Unfortunately, it is not easy to study the $T_0 + 1$ states in $\Delta T_z = -1$ charge-exchange reactions, in part because they are disfavored due to the clebsch-Gordan isospin coefficients for $N > Z$ discussed above. In addition, they are situated at excitation energies where there are many states that have lower isospin. Still, the studies of analog states have been used to extract GT strengths for β^+ direction from (p,n) charge-exchange data, including for the case of ^{60}Ni(^{3}He,t) reaction. In this work, it is attempted to improve on that previous effort.

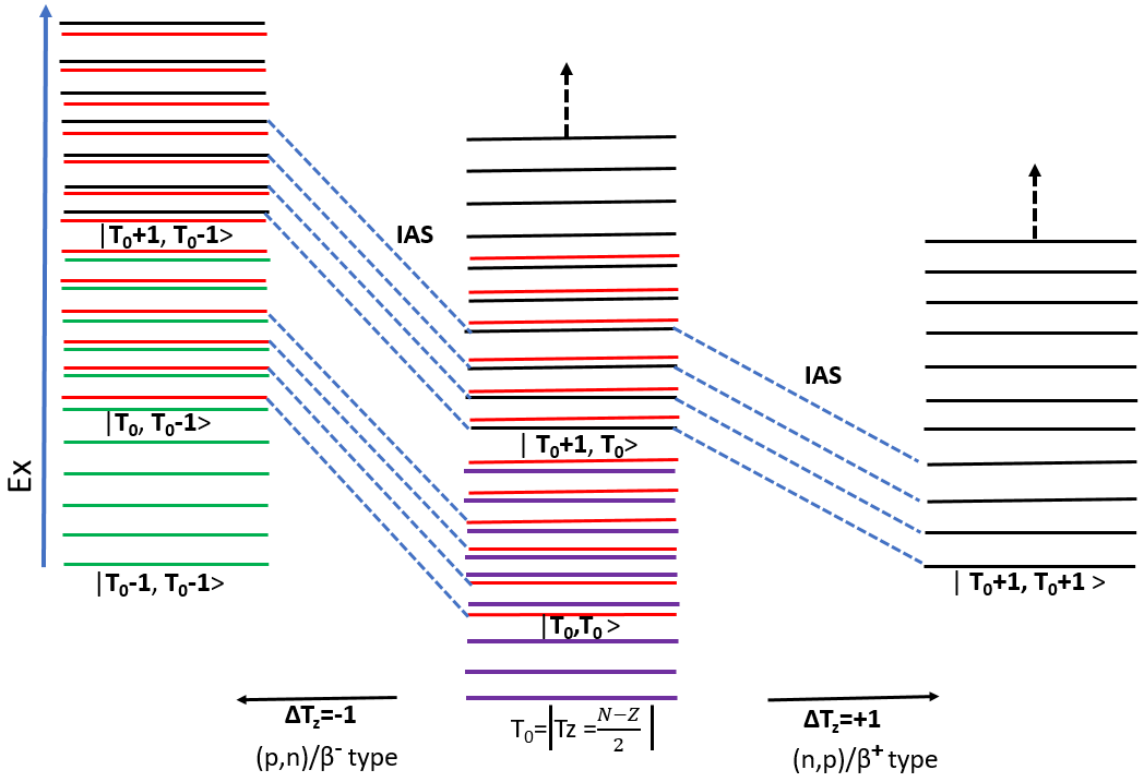

Figure 2.4 Schematic depiction of isospin symmetry in charge-exchange reactions. The dotted lines indicate states of like isospin (analog states) in both $\Delta T_z = \pm 1$ directions. In the $\Delta T_z = -1$ direction, the IAS is populated from T_0 to T_0 transition, but no such transition can occur in $\Delta T_z = +1$ direction.

2.3 Isovector Giant Resonances

2.3.1 Isobaric Analogue State

The experimental measurements of nuclear spectra have shown that families of isobaric nuclei, which have the same mass number (A), but different neutron (N) and proton (Z) numbers have

analog energy levels. The neutron and proton have similar masses and are up/down states of a system with isospin $1/2$ and have approximately identical behavior under the strong nuclear force. Ignoring the electromagnetic and weak interactions, nuclear spectra with identical spins are therefore similar, which is known as isospin symmetry. The IAS excited in charge-exchange reactions is the analog of the ground state of the mother nucleus. It has the same structure, but with one neutron (proton) replaced by a proton (neutron). The states have the same isospin T_0, but differ by one unit in T_z, same quantum numbers, and the same microscopic properties.

Focusing on nuclei with $N > Z$, the IAS of the mother ground state can only be excited in $\Delta T_z = -1$ charge-exchange reactions: in the $\Delta T_z = +1$ direction, no states with isospin identical to that of the mother ground state are available, as shown in Figure 2.3. The excitation of the IAS is characterized with the transfer of quantum numbers $\Delta J = \Delta L = \Delta S = 0$ and $\Delta T = 1$. In terms of the shell-model, to excite the IAS, a target neutron is replaced with a proton that fills the same single-particle orbit. The excitation strength of IAS exhausts the model-independent Fermi sum rule [10] given by:

$$\mathrm{S}(\beta^-) - \mathrm{S}(\beta^+) = \mathrm{N} - \mathrm{Z}, \tag{2.3}$$

where $S(\beta^-)$ and $S(\beta^+)$ indicate the total strength of the β^- and β^+ decays for the Fermi transitions, respectively. For $N - Z > 0$, $S(\beta^+) = 0$. The simple structure of IAS can help in the understanding of the neutron skins [11] and the nuclear equation of state [12].

For charge-exchange reactions at intermediate energies ($\sim$ 100 MeV/u and above), it has been shown [13] that the differential cross section at small momentum transfer is proportional to the Fermi strength, B(F):

$$\left(\frac{\mathrm{d}\sigma}{\mathrm{d}\Omega}(\mathrm{q}=0)\right)_{\mathrm{IAS}} = \hat{\sigma}_\tau \mathrm{B}(\mathrm{F}), \tag{2.4}$$

where $\hat{\sigma}_\tau$ is the unit cross section. Since this excitation is due to the central isospin transfer (V_τ) component of the nucleon-nucleon interaction (see Chapter 3), the measurement of the IAS provides direct information about this component of the interaction [13].

The IAS has an attraction property: it can be used to measure the charge-exchange cross section at forward momentum transfers that are proportional to the $N - Z$ transition strength. It provides a

direct probe of the strength of the isospin component of the nucleon-nucleon.

2.3.2 Gamow-Teller Resonances

Over the past decades, Gamow-Teller (GT) transitions have been one of the main motivations for performing charge-exchange experiments at intermediate beam energies. The GT transition populated through charge-exchange reactions are associated with the $\sigma\tau$ operator and have $\Delta L = 0$, and $\Delta S = 1$, and $\Delta T = 1$. The GT transitions populates the same final states as in allowed β/electron-capture (β/EC) decays. Due to the proportionality between cross section at $q = 0$, and B(GT), the Gamow-Teller transition strength can be extracted from charge-exchange reactions (see section 5.3.1), even though CE reactions are mediated by the strong nuclear force, and β/EC decay is mediated by the weak nuclear force. However, by using charge-exchange reactions, one can populate states that are outside of the Q-value window available for β/EC decay (more details seen [1, 4, 14, 15, 16, 17, 18]).

The ability to extract the GT transition strength model-independently from charge-exchange reactions allows for a stringent test of nuclear structure models. This ability has many applications in nuclear astrophysics and neutrino physics. The well-known model-independent proportionality relationship between GT transitions cross section and B(GT) from the charge-exchange reactions [19, 13, 20] is given by:

$$\left(\frac{\mathrm{d}\sigma}{\mathrm{d}\Omega}(\mathbf{q}=0)\right)_{\Delta\mathrm{L}=0} = \hat{\sigma}_{\mathrm{GT}}\mathrm{B(GT)} \tag{2.5}$$

where $\hat{\sigma}_{\mathrm{GT}}$ is the Gamow-Teller unit cross sections, and on the left-hand side, the Gamow-Teller cross section is extracted at zero momentum transfer ($\mathbf{q} = 0$, where $\mathbf{q} = \mathbf{k_f} - \mathbf{k_i}$), from theoretical calculations by setting the Q-value of the reaction used to 0 MeV and considering the cross section at zero degrees. Experimentally, the measured cross section is the combination of all possible charge-exchange transitions. Multiple decomposition analysis (MDA) is performed to extract the $\Delta L = 0$ component by fitting the experimental angular distribution with a linear combination of various curves (this will be discussed in more details, see Chapters 3 and 5).

The total amount of Gamow-Teller strength, including both the β^+ and β^- directions for a

particular nucleus, is constrained by the model-independent sum rule [10]:

$$S(\beta^-) - S(\beta^+) = 3(N - Z), \tag{2.6}$$

where N is the number of neutrons present in the target nucleus, and Z is the number of protons. In nuclei in which N is appreciably larger than Z, Equation 2.6 reduces in a shell-model picture to :

$$S(\beta^-) \approx 3(N - Z), \tag{2.7}$$

since $S(\beta^+) \sim 0$ due to Paul blocking [1]. Experimentally, only 50-60% of the estimated sum-rule strength can be accounted for in the excitation-energy range including the GTR. This is known as the quenching of the sum rule [21, 22, 23, 24].

2.3.3 Isovector-Spin & Non-Spin-Transfer Giant Monopole Resonances

The IVGMR and IVSGMR resonances can be described as breathing modes in which the proton and neutron fluids oscillate out-of-phase. They are of fundamental interest as collective excitations at high excitation energies that are described microscopically by coherent $2\hbar\omega$, $1p - 1h$ excitations [25, 26, 27]. Their properties serve as tests for microscopic model calculation with effective nucleon-nucleon interactions [28]. The excitation energy of the IVGMR and IVSGMR can be used to understand the bulk properties of nuclei and nuclear matter [2, 1, 28, 29, 30, 31]. The strength distribution of the IVGMR provides a useful tool for better understanding the neutron skin properties from which the density dependence of the symmetry energy for asymmetric nuclear matter can be constrained [32, 33].

The isovector giant monopole resonance (IVGMR) is characterized by no change in the orbital angular momentum ($\Delta L = 0$), non-spin-transfer ($\Delta S = 0$), and isospin-transfer of one unit ($\Delta T = 1$). The properties of the IVGMR resonance provide insight into the fundamental understanding of the isovector part of the residual nuclear interaction and isospin symmetry breaking and isospin mixing in nuclei [31]. The IVGMR and IAS differ by the change in principal quantum number (n) between the particles and holes. The IVGMR ($2\hbar w$ excitation) is the overtone of the IAS ($0\hbar w$). To investigate the IVGMR experimentally, a probe for non-spin-transfer excitations is required, because

its spin-flip partner has a much larger cross section than the IVGMR at intermediate beam energies [34, 35, 36, 37, 38, 39, 40, 41]. Therefore, the experimental evidence for the IVGMR is limited to the results from the small number of charge-exchange experiments. Convincing evidence for the IVGMR has been found via the spinless pion charge-exchange reaction (π^+, π^0) [42, 43, 44, 45]. In addition, evidence for the IVGMR has been reported in ^{60}Ni(^{7}Li, ^{7}Be) charge-exchange reaction [46]. Recently, the (^{10}Be, ^{10}B + γ[1.74 MeV]) charge-exchange reaction at E(^{10}Be)=100 AMeV was reported as a new probe for isolating the isovector non-spin transfer excitations, and thus a useful probe for studying the IVGMR, as evidenced by the successful extraction of the IVGMR and IVGDR cross sections from ^{28}Si(^{10}Be, ^{10}B + γ) [29].

For probes that are not selective for spin-transfer, the spin-transfer partner of the IVGMR, the IVSGMR is much more strongly excited than the IVGMR at intermediate beam energies ($100 < E_x < 300$ AMeV) [34, 37]. This is because the spin-isospin ($\sigma\tau$) component of the nucleon-nucleon interaction is much stronger than the isospin (τ) component [3, 37, 41]. The operator of the IVSGMR carries the same $\Delta L, \Delta S$, and ΔT as the operator of the GTR. However, the IVSGMR is a $2\hbar\omega$ excitation, and the GT excitation is of $0\hbar\omega$ nature. So far, the progress in the experimental studies of the IVSGMR is more advanced than for the IVGMR due to the much higher cross section, which makes it easier to identify charge-exchange experiments with light ion probes. [47, 48]. In general, isolating and observing the IVSGMR in $\Delta T_z = +1$ charge-exchange reactions is easier than in the $\Delta T_z = -1$ charge-exchange reactions. This is because the IVSGMR in the $\Delta T_z = +1$ direction is located at lower excitation energies, where the continuum background is lower [35, 49]. The exothermic heavy-ion charge-exchange reactions have been applied to enhance the signature of the IVSGMR through ^{90}Zr(^{12}N, ^{12}C) reaction at 175 MeV/u [50]. The exothermic nature of this reaction reduces the momentum transfer for excitations at high excitation energy which is beneficial for enhancing the cross section for the $\Delta L = 0$ giant resonances.

2.3.4 Isovector-Spin & Non-spin-Transfer Giant Dipole Resonance

Significant effort to investigate the other isovector giant resonances through charge-exchange reaction has been made, including the isovector spin giant dipole resonances (IVSGDR, $\Delta L =$

1, $\Delta S = 1$, $\Delta T = 1$) and non-spin-transfer giant dipole resonances (IVGDR, $\Delta L = 1$, $\Delta S = 0$, $\Delta T = 1$). The IVGDR was the first resonance that could be explained in a macroscopic picture in which the neutron fluid oscillates against the proton fluid [51].

The IVSGDR consists of 3 components associated with the three possible couplings from its spin transfer and angular momentum transfer: $J_f^\pi = 0^-, 1^-, 2^-$, assuming $J_i^\pi = 0^+$, as shown in Table 2.1. In the experimental data analysis, it is not easy to isolate the three spin-parity components of the IVSGDR. All three components are associated with angular momentum transfer $\Delta L = 1$. Their angular distributions are therefore similar, and they peak approximately at the same scattering angle. It is beneficial to separate the three components to perform a detailed test of the theoretical calculations, but it requires the measurement of polarization observables, which has only been done a few times (see e.g., [52]). The IVSGDR is more strongly excited in charge-exchange reactions at intermediate beam energies compared to the IVGDR. This is because the spin-isospin ($\sigma\tau$) component of the nucleon-nucleon interaction is much stronger than the isospin (τ) component [3, 37, 41]. However, there is no well-established proportionality between transition strength and differential cross section for dipole resonances. There is also no model-independent sum rule for the IVSGDR that can be used to characterize the amount of strength found in spectra [35, 36].

2.4 Hydrodynamic Model of Giant Resonances

The hydrodynamic or macroscopic model that has been applied to isovector giant resonances describes a nucleus as a liquid drop of the proton and neutron fluids oscillating in different modes around its equilibrium shape. The spins of the nucleons serve as an additional degree of freedom. When describing a nucleus as an oscillation of a liquid drop, two main modes can be distinguished: a surface-vibrational mode and a compressional mode. It is worth noting that a vibrating drop can have a superposition of both modes [3]. The amplitude of the oscillations is small. For the surface-vibrational mode, harmonic oscillations about a mean spherical shape are assumed (see more theoretical discussions of the surface-vibrational and compressional modes for giant resonances in the References [3, 53, 6, 54, 55]).

The macroscopic description of giant resonances provides a picture that connects to the bulk

properties of the nucleus and nuclear matter. Therefore, the study of giant resonances can help constrain models of these bulk properties. An example is the simple vibrational giant resonance mode known as the ISGMR observed for the first time in 1977 by Harakeh et al. [56, 57] and confirmed in the same year by Youngblood et al.[58, 59]. They used inelastic α-scattering measurements at forward scattering angles. This properties of the ISGMR yields insights into the bulk properties of the nucleus, in particular the incompressibility of nuclear matter (K_{nm}) [60, 55]. The location of the excitation energy of the ISGMR was estimated for the first time by Bohr and Mottelson [6]. The energy of the isoscalar giant monopole resonance was determined as a function of the mass of nucleus (A) [61] to be:

$$E_{1,0} = \frac{\hbar k_{1,0}}{1.2}\sqrt{\frac{K_{nm}}{9m}}A^{-1/3} \quad \text{MeV} \tag{2.8}$$

where $k_{1,0}$ stands for eigenvalues of the motion for principal quantum number $n = 1$ and multi-polarity $l = 0$, and m is the nucleon mass. K_{nm} was not known at the time of derivation, and was estimated to be $K_{nm} = 135$ MeV [6]. The solution for the ISGMR ($E_{1,0}$) is:

$$E_X^{ISGMR} = 65A^{-1/3} \quad \text{MeV} \tag{2.9}$$

When the experimental data became available, the value of k_{nm} was determined to be 231 ± 5 MeV [60, 55].

For the IVGMR, assuming that a nucleus consists of two inter-penetrating, incompressible fluids [51, 3, 53, 6, 54, 55] of protons and neutrons, the restoring force is proportional to the surface of the nucleus (R^2). The frequency of the resulting harmonic oscillations is proportional to the square root of a constant force over mass parameter (A). Therefore, this assumption leads to a behavior that is linear with $R^{-1/2}$ or linear with $A^{-1/6}$, since $R = r_o A^{1/3}$ [3].

In general, the vibrational frequency and excitation energy of a particular giant resonances can be determined come from linearized Navier-Stokes equations [62]. For example, solving for the IVGMR, the excitation energy is:

$$E_x^{IVGMR} = 170A^{-1/3} \quad \text{MeV} \tag{2.10}$$

However, this model with volume terms only does not accurately describe the excitation energies of the isovector giant resonances. A study by Bowman et al. [30] indicated that besides the volume terms, surface tension effects must be taken into account as well to describe the properties of isovector giant resonances. Therefore, a more precise estimate of the excitation energy of the IVGMR was found to be:

$$E_x^{IVGMR} = 88A^{-1/6}\left(1 + \frac{14}{3}A^{-1/3}\right)^{-1/2} \quad \text{MeV} \tag{2.11}$$

and the systematic study of experimental results for nuclei gives the excitation energy of the IVGDR as a function of mass umber (A) [3, 63] to be:

$$E_x^{IVGDR} = 31A^{-1/3} + 20A^{-1/6} \quad \text{MeV} \tag{2.12}$$

2.5 Isovector Giant Resonances in the Charge-Exchange Spectrum

In the microscopic picture, the excitation energies of giant resonances can be estimated from the energy differences between the shells in which the particles and holes that participate in the coherent one-particle one-hole (1p-1h) excitations are located. The excitation energy for giant resonances is related to the difference in the major shell (ΔN) of the particles and the holes. The energy difference between each major shell is estimated to be $\hbar\omega = 41A^{-1/3}$. This simple approximation provides a basic understanding of the relative excitation energies of the isovector giant resonances. This is illustrated in Figure 2.5(a), which displays the excitation-energy spectrum in ^{60}Cu obtained from the ^{60}Ni(^{3}He,t) reaction at 140 MeV/u for 3 ranges in scattering angle, as discussed in more detail in Chapter 4 and 5. Different giant resonances appear at different excitation energies. The angular distribution provides a characteristic of the angular momentum transfer associated with a particular excitation.

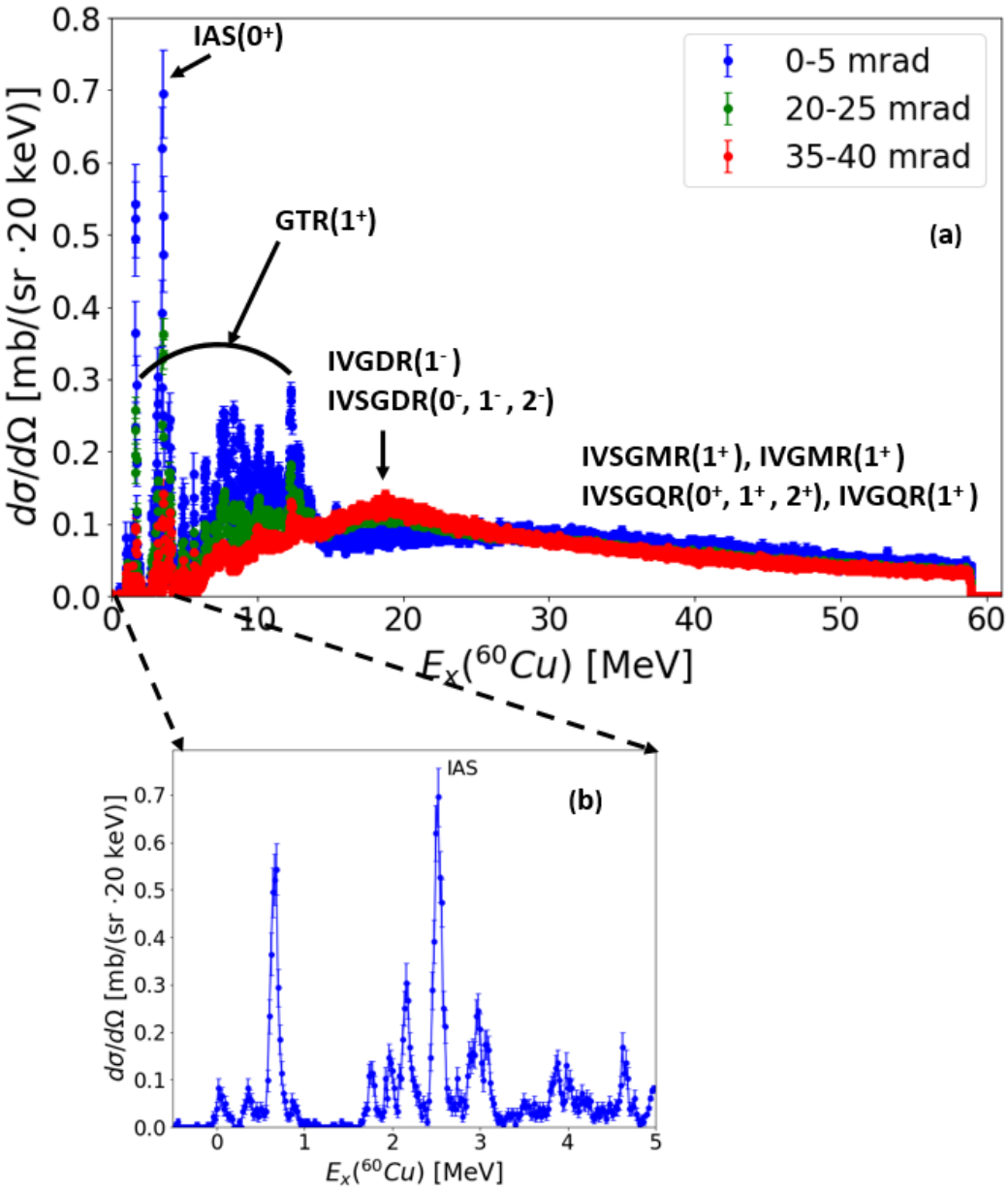

Figure 2.5 The typical $\Delta T_z = -1$ charge-exchange energy spectrum from the full range of excitation energy (60 MeV) used for the three angular settings from the ^{60}Ni(^{3}He,t) reaction. Various isovector giant resonances and their corresponding spin and parity (J^π) are indicated. Figure (a) include the Isobaric Analog State (IAS), Gamow-Teller Resonance (GTR), the isovector spin, and non-spin giant dipole, monopole, and quadrupole resonances (IVSGDR/IVGDR, IVSGMR/IVGMR, and IVSGQR/IVGQR). Their features can be identified by comparing spectra at different scattering angles. Figure (b), the visualization of the IAS state at the lower excitation energy range between 0 to 5 MeV.

For example, the GTR, IAS, and monopole excitations are associated with $\Delta L = 0$, so they peak at 0° scattering angle. For the (^{3}He,t) reaction at 140 MeV/u, their presence is enhanced in the spectrum gated on scattering angles between 0 and 5 mrad. Dipole excitations peak at small but finite angles and their features are enhanced at scattering angles between 35 and 45 mrad. The IAS is known to reside at $E_x(^{60}Cu) = 2.55$ MeV, and the main component of GTR appears at excitation energies of $\sim$ 10 MeV. The IVSGDR peaks at an excitation energy of about 18 MeV. The difference in the excitation energy between $\Delta N = 1\hbar\omega$ dipole resonances and the $\Delta N = 0\hbar\omega$ IAS is about 16 MeV, higher than estimated value of $1\hbar\omega = 41A^{-1/3} = 10.5$ MeV. The $\Delta N = 2\hbar$w IVSGMR and IVGMR are located at excitation energies of about 35 MeV and are not easy to identify due to their large widths. The IVSGQR and IVGQR resonances are located at similar excitation energies, but their angular distributions are relatively flat at forwarding scattering angles. Therefore, their contributions are difficult to observe when comparing spectra at different scattering angles.

At lower excitation energies, up to 5 MeV (Figure 2.5(b)), the most dominant peak is the IAS, and it is possible to identify individual states in ^{60}Cu. However, the level density increases as a function of the excitation energy and even at 4-5 MeV it becomes difficult to identify individual states. These low-lying states are non-collective in nature.

2.6 Overview of the Charge-Exchange Reaction Probes

Over the past decades, charge-exchange reactions have been used to investigate various phenomena in nuclear physics with applications in nuclear structure and astrophysics. Charge-exchange reactions have been developed since the last half-century [64, 65], and they are used to probe the spin-isospin response of nuclei.

As discussed above, in terms of the isospin formalism, charge-exchange reactions are characterized by an isospin-transfer by one unit, $\Delta T = 1$ (isovector), meaning that occur with $\Delta T_z = \pm 1$ as shown in Figure 2.3. $\Delta T_z = -1$ corresponds to the (p,n)-type, causing the residual nucleus to become more proton-rich nucleus, while $\Delta T_z = +1$ corresponds to the (n,p)-type, from which the residual nucleus become more neutron-rich. Both probes, involve spin $\frac{1}{2}$ particles and can mediate $\Delta S = 0$ and $\Delta S = 1$ excitations. In charge-exchange reactions, any amount of angular

momentum can be transferred, $\Delta L = 0$ (monopole), $\Delta L = 1$ (dipole), $\Delta L = 2$ (quadrupole), etc. At intermediate beam energies, the excitations with spin-transfer are strongly favored compared to non-spin transfer.

In β-decay experiments, states may be measured in an excitation energy region from 0 MeV up to the Q-value of the reaction, but higher-lying states will not be accessible via this reaction. In contrast, charge-exchange reactions are not limited by the Q-value, and highly excited states can be studied using different charge-exchange probes, such as (p, n)/(^{3}He,t), (n, p)/(t,^{3}He), $(d, ^2$He), and other reactions (see Table 2.2). A variety of probes are used with different advantages for the study of isovector excitations. The choice depends on the experimental considerations and the sensitivity to different resonances (see more experimental discussions about the IVGRs probes used in References [66, 67, 4, 1, 14]).

Table 2.2 Various charge-exchange reaction probes are classified by: β^--type or (p,n)-like reactions (left side) and β^+-type or (n,p)-like reactions (right side).

β^--type	β^+-type
(p,n)	(n,p)
(^{3}He,t)	(t,^{3}He)
(^{6}Li,^{6}He)	(d,^{2}He)
(^{12}C,^{12}Be)	(^{12}C,^{12}N)
(^{10}C,^{10}B)	(^{13}C,^{13}N)
(^{10}Be,^{10}B)	(^{7}Li,^{7}Be)
π^+ , π^0	π^- , π^0

The analysis of data obtained from the (n,p) or (p,n)-like reactions benefits from the reduced complexity of the reaction mechanism compared to using composite probes such as (t,^{3}He) or (^{3}He,t) reactions [68]. However, to achieve a better energy resolution, it is preferred that both the projectile and ejectile are charged so that their momenta can be well constrained and analyzed. For example, with the (^{3}He,t) reaction an excellent resolution of as low as 30 keV or less can be achieved [69, 70, 71, 72]. Achieving a better resolution is useful for studying the reaction mechanism for which it is preferable to isolate individual transitions, or for the study of the fine structure of giant resonances [73].

The main difference between the (n,p) and (p,n) reactions and reactions induced by composite

probes such as (t,^{3}He) and (^{3}He,t) reactions is that the former probe the target nucleus relatively deeply, while the latter predominantly probe the surface of the target nucleus. The strong absorption near the surface of the target nucleus is a general characteristic of composite probes used for charge-exchange reactions at intermediate beam energies. Therefore, it has been used to isolate the excitations associated with radial nodes near the nuclear surface such as the IVSGMR and IVGMR [74]. This specific property was used to compare the (t,^{3}He) and (n,p) reactions by measuring the double-differential cross sections at 300 MeV/u on ^{208}Pb and ^{92}Zr targets at the rare isotope beam factory of RIKEN [40].

Experiments using the (d,^{2}He) reaction as a probe are relatively complex compared to (t,^{3}He) and (n,p) reactions, but such experiments have been successful in tracking the isovector spin-transfer strength for many nuclei [75, 76, 77, 78, 79, 18]. The complexity of the (d,^{2}He) reaction is due to the simultaneous measurement of the two emitted protons from the unbound ^{2}He particle. The energy and angles of both protons need to be measured accurately in order to achieve good energy and scattering angle resolutions in the reconstructed spectra and to allow for making a precise cut on the relative energy (ϵ_{pp}) between the two emitted protons. [68]. However, there is a disadvantage to using the (d,^{2}He) reaction to study giant resonances in medium-heavy and heavy nuclei because of the background from deuteron-breakup reactions occurring in the Coulomb fields of the target nuclei. Consequently, the studies of the isovector giant resonances through the (d,^{2}He) reaction have been limited to light and medium-heavy nuclei [68].

The (^{6}Li,^{6}He) reaction probe has also been used as a selective filter for spin-transfer excitations because of the transitions from the $J^\pi = 0^+$ ground state in ^{6}Li to the $J^\pi = 1^+$ ground state in ^{6}He. Since ^{6}He has no particle-stable excited states, effects from ejectile excitation can be avoided [80]. Experiments with the (^{6}Li,^{6}He) reaction were performed at $\sim$ 100 MeV/u on ^{12}C, ^{13}C, ^{58}Ni, and ^{90}Zr target nuclei [81]. While it was not possible to measure the scattering angle, this reaction was successful in terms of isolating the spin-transfer of giant resonances [80].

The (^{7}Li,^{7}Be) and (^{7}Li,^{7}Be+γ) reactions have been used at beam energy of $E/A = 50$ MeV on ^{6}Li, ^{12}C, ^{90}Zr, ^{120}Sn, ^{208}Pb and polystyrene targets [82]. The gamma rays detected from excited

states in ^{7}Be via (^{7}Li,^{7}Be+γ) were successfully used to isolate excitations associated with and without spin-transfers. With this probe, either the $3/2^{-}$ ground state or the $1/2^{-}$ excited state at 429 keV in ^{7}Be can be populated making it possible to separate excitations associated with $\Delta S = 0$ and $\Delta S = 1$. This technique has been applied to investigate the isovector giant resonances in forwarding kinematics at beam energies of $50 - 70$ AMeV [82, 83, 84, 46].

The (^{12}C,^{12}B) and (^{12}C,^{12}N) reactions also have selective spin-transfer properties and they can be used to investigate $\Delta T_z = -1$ and $\Delta T_z = +1$ transitions, respectively. The (^{12}C,^{12}B) reaction has been used to measure GT transitions on ^{12}C, ^{26}Mg, ^{54}Fe, ^{58}Ni, and ^{90}Zr targets, and the (^{12}C,^{12}N) reaction have been used on ^{56}Fe targets at a beam energy of $E/A = 70$ MeV [85], 135 AMeV [86], and others [50, 87, 88]. However, with large negative reaction Q-values, the significant momentum transfers associated with these reactions make them less useful to study the isovector transitions, specifically the monopole excitations.

The charge-exchange probe (^{13}C,^{13}N) has been studied to locate isovector ($\Delta T = 1$) non-spin-transfer ($\Delta S = 0$) giant resonances via ^{60}Ni(^{13}C,^{13}N)^{60}Co reaction at $E/A = 100$ MeV [89]. Through a distorted wave Born approximation analysis, the isovector dipole resonance was found at $E_x = 8.7$ MeV and quadrupole resonance was found at $E_x = 20$ MeV. The proton separation energy in ^{13}N is less than the excitation energy of the first excited state, the only transition contributed was the one from the ^{13}C($\frac{1}{2}^{-}$) ground state to the ^{13}N($\frac{1}{2}^{-}$) [89, 90]. This transition is dominated by the large Fermi matrix element, which is why this reaction provides some selectivity for ΔS = 0.

The pion ($\pi^{\pm}, \pi^{0}$) charge-exchange reactions are another probe used to investigate the isovector excitations. Since pions are spinless particles, they are used as an ideal tool for studying spinless-transfer excitations [91]. The (π^{+}, π^{0}) and (π^{-}, π^{0}) reactions were used to investigate the properties (energies, widths, and cross sections) of the isovector monopole, and the other isovector giant resonances in nuclei between ^{14}C and ^{208}Pb [43]. The production of pion beams is complicated and it is difficult to achieve a high resolution in the π^{0} exit channel through the analysis of the $\pi^{0} \rightarrow \gamma\gamma$ decay [3]. However, at Los Alamos Meson Physics Facility (LAMPF) successful the pion charge-exchange reactions have been performed with aim of extracting information on the IVGMR

[43, 44, 42].

The availability of rare-isotope beams has resulted in the use of new unstable charge-exchange reaction probes in forward kinematics. Rare-isotope beams provide new possibilities to selectively excite specific giant resonances, for example, the (^{10}C,^{10}B(0^+,IAS)) reaction [92, 93] and the (^{10}Be,^{10}B(0^+,IAS)) reaction [29] have been used to selectively excite the non-spin-transfer excitations. In addition, by using rare isotope beams it is possible to create exothermic reactions. The released energy can offset the energy needed for the excitation of the target nucleus. Therefore, this reduces the linear momentum transferred between the projectile and the target nucleus and results in creating more favorable conditions to study monopole excitations. For example, the (^{12}N,^{12}C) charge-exchange reaction at 175 MeV/*u* was successfully developed and applied to ^{90}Zr as a novel probe for studying the excitation of the IVSGMR [50]. This probe comes with an additional advantage of spin-transfer transitions that are selectively excited.

As charge-exchange reactions probe the spin-isospin response of nuclei, they are very attractive for studying the excitations from nuclei with asymmetric neutron-to-proton ratios. By impinging the rare-isotope beam on a hydrogen target, the (p,n) reaction in inverse kinematics can be used to study unstable nuclei. In the first experiments, the neutron from the (p,n) reaction was not detected. This method relies on measuring the residual nuclei from the projectile only and avoided the detection of the recoil neutron from the proton target in the process [94, 95, 96, 97, 98, 99, 100, 101].

More recently, inverse-kinematics (p,n) experiments using the missing-mass method in which the neutrons are detected have been developed at NSCL [102] and at RIBF group [92]. The NSCL group has used the setup called Low Energy Neutron Detection Array (LENDA) designed to facilitate the study of (p,n) charge-exchange reactions in inverse kinematics at intermediate energies using unstable beams. The LENDA detector was successfully developed and used to study the ^{56}Ni(p,n) and ^{55}Co(p,n) reactions at 110 MeV/*u* in inverse kinematics in order to extract GT strengths for transitions to ^{56}Cu and ^{55}Ni, respectively [103], which are of astrophysical importance. Other experiments where this technique has been utilized are ^{132}Sn(p,n) and ^{12}Be(p,n) reactions at RIBF [104] and ^{16}C(p,n) at NSCL [105].

The development of a new technique to perform charge-exchange experiments in inverse kinematics using the (n,p) reaction has been more complicated. This is because a neutron target is not available. Therefore, one of the other probes in $\Delta T_z = +1$ direction must be used [68]. The first successful attempt to study (n,p) reactions in iverse kinematics used the ^{34}P(^{7}Li,^{7}Be + γ(429 keV)) charge-exchange reaction in inverse kinematics at 100A MeV to measure GT transition strengths in the β^+ direction from ^{34}P, populating states in ^{34}Si [106]. Meharchand et al. (2010) used (^{7}Li,^{7}Be) reaction in inverse kinematics to study the spectroscopy of ^{12}Be [107]. This technique relies on tagging the charge-exchange reactions with γ-rays emitted from the decay of the $1/2^-$ excited state at 429 keV from ^{7}Be and use the measurement of the projectile-like residual in a spectrometer to learn about reaction kinematics and be able to extract scattering angles and the excitation energies. As a consequence, its use is limited to relatively light nuclei and to excitation energies below the particle-decay threshold.

The most recent (n,p)-type charge-exchange reaction developed by Giraud et al. (2021) [108] uses the (d,^{2}He) reaction in inverse kinematics to study exotic nuclei. This was done by using an active-target time-projection chamber (AT-TPC). The inner volume of the AT-TPC was filled with deuterium gas, which serves as the target and the detector medium for the tracking of the two protons emitted from the unbound ^{2}He nucleus. The charge-exchange residual nuclei were detected in the *S*800 spectrometer, and served as a trigger for the time-projection chamber data acquisition system [109, 110].

CHAPTER 3

CHARGE-EXCHANGE REACTION TECHNIQUES

Charge-exchange (CE) reactions involve the exchange of a proton and neutron between a target nucleus and an incoming beam nucleus. In these reactions, the isospin changes by $\Delta T = 1$ (isovector), with the potential for $\Delta S = 1$ (spin transfer) or $\Delta S = 0$ (non spin transfer) and the ability to transfer various units of angular momentum: $\Delta L = 0$ (monopole), $\Delta L = 1$ (dipole), $\Delta L = 2$ (quadrupole), $\Delta L = 3$ (octupole), and so forth. This chapter gives a brief overview of CE reactions and associated techniques.

The theoretical cross sections calculated in this thesis were performed using the distorted wave Born approximation (DWBA) method discussed in section 3.3 and 3.4 with the FOLD code [111]. The DWBA calculations were used to perform a multiple decomposition analysis for extracting the isovector response associated with different units of angular momentum transfer. To convert extracted cross sections into Gamow-Teller strength, the Eikonal approximation is applied as discussed in section 3.5.

3.1 Introduction into Charge-Exchange Reaction Techniques

To extract information about charge-exchange excitations and giant resonances from measured excitation-energy spectra, such as the one shown in Figure 2.5, several steps are required. The experimental differential cross sections are determined from the data with:

$$\left(\frac{d\sigma}{d\Omega}\right)^{exp} = \frac{Y}{N_b N_t \epsilon_1 \epsilon_2 d\Omega} \quad mb/sr, \tag{3.1}$$

where Y represents the total number of counts in a specific angular bin, N_b is the total number of nuclei that struck the target foil, N_t is the number of nuclei in the target, $d\Omega$ is the opening angle, ϵ_1 is the correction for the lifetime of the data acquisition system (DAQ) and ϵ_2 is the correction for the target purity.

To extract the contribution from transitions associated with the transfer of different units of angular momentum transfers (ΔL) a multiple decomposition analysis (MDA) [112, 113] is performed. The measured differential cross section for each peak or energy bin is fitted with a linear

combination of theoretical angular distributions associated with these different angular momentum transfers:

$$\left(\frac{d\sigma}{d\Omega}\right)_{exp} = a_0 \left(\frac{d\sigma}{d\Omega}\right)^{DWBA}_{\Delta L=0} + a_1 \left(\frac{d\sigma}{d\Omega}\right)^{DWBA}_{\Delta L=1} + a_2 \left(\frac{d\sigma}{d\Omega}\right)^{DWBA}_{\Delta L=2} + ..., \tag{3.2}$$

where $\left(\frac{d\sigma}{d\Omega}\right)^{DWBA}_{\Delta L=i}$ are the theoretical differential cross sections for $\Delta L = i$ and a_i are their corresponding fit parameters.

In this work, the theoretical differential cross sections are calculated in Distorted Wave Born Approximation (DWBA), which will be discussed in more details in the following sections, focusing on the case of the ^{60}Ni(^{3}He,t) reaction at 140 MeV/u.

3.2 Calculation of Differential Cross Sections

Theoretical calculations for the differential reaction cross section in the (^{3}He,t) experiment were performed using the FOLD code package [111, 114]. This code uses the Distorted Wave Born Approximation (DWBA), discussed in section 3.3, where both incoming and outgoing waves are distorted by the mean field of the target nucleus. Details regarding the inputs and outputs for the DWBA calculations are provided in section 3.4.

The FOLD code was used to calculate the differential cross sections for charge-exchange (CE) reactions involving composite particles composed of three component codes, including the WSAW, FOLD, and DWHI. The WSAW code was used for computing radial wave functions for relevant shell-model orbitals, as discussed in section 3.4. The second component, FOLD, was used to calculate the form factor based on a double folding of the one-body transition densities, providing structural information for the target and projectile system based on the nucleon-nucleon interaction. The third component, DWHI, was employed to calculate the differential cross section while considering the distortion of incoming and outgoing particles due to the mean field of the target nucleus, incorporating optical potentials. Additionally, more details about the DWHI code were discussed in section 3.4.3

For the ^{60}Ni(^{3}He,t) reaction, one-body transition densities (OBTDs) were obtained within the normal-modes (NM) formalism using the NORMOD code [115], as detailed in section 3.4.2. The

folding procedure was executed using the Love-Franey effective nucleon-nucleon (NN) interaction at 140 MeV/*u* [41, 37].

Figure 3.1 shows a schematic description of the inputs and outputs for the DWBA calculations in FOLD code to calculate differential cross sections for CE reactions with composite particles that consist of three parts: WSAW, FOLD, and DWHI.

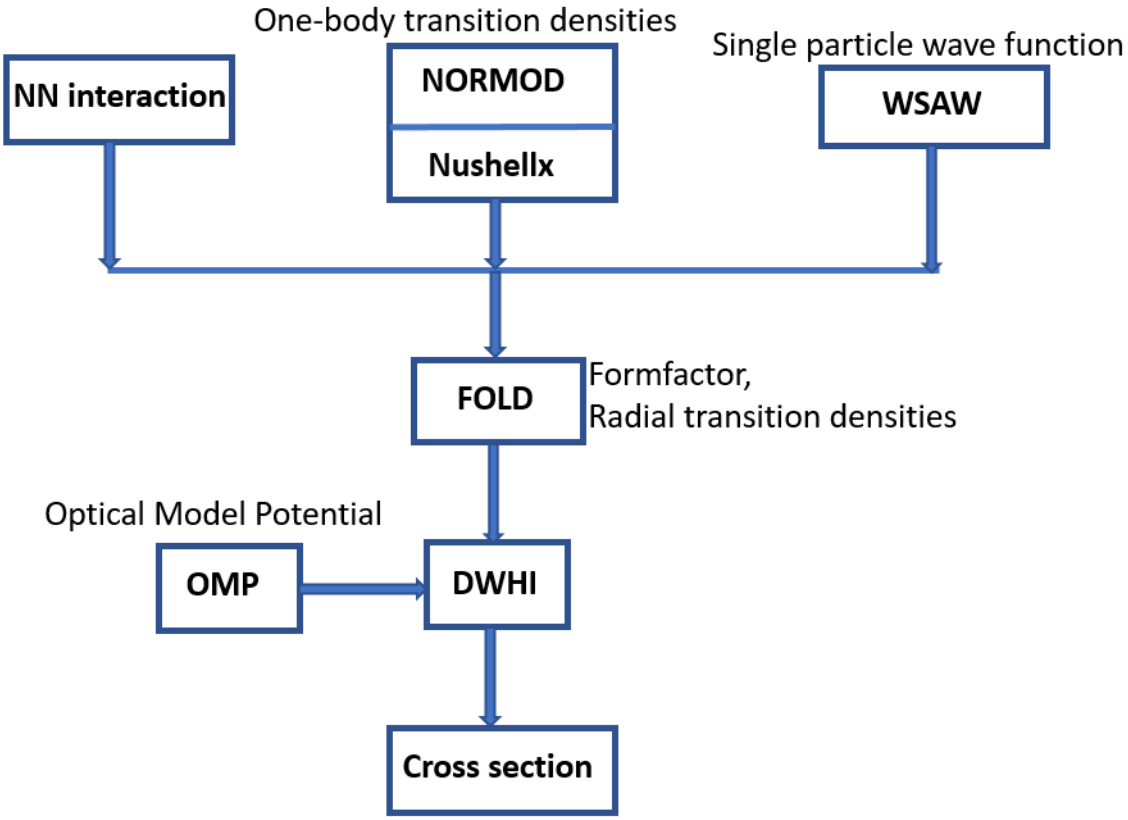

Figure 3.1 Hierarchy image describing the steps in the distorted wave Born approximation (DWBA) used to compute theoretical differential cross sections through FOLD code.

3.3 Brief Description of the DWBA

Above beam energies of about $\sim$ 100 MeV/u, the charge-exchange reaction predominantly proceeds in a single step. Therefore, to good approximation, two-step (or more-step) processes do not have to be taken into account. Here, we assume that the nucleons of the projectile and target system are non-identical. Participating nucleons of the target and the projectile systems are treated equally and the initial and final states have definite isospins. For the reaction:

$$\text{projectile(p)} + \text{target(t)} = \text{ejectile(e)} + \text{residual(R)}, \tag{3.3}$$

the Hamiltonian in the prior form can be written as:

$$H = H_p + H_t + T_{pt} + V_{pt}, \tag{3.4}$$

where H_p and H_t are the internal Hamiltonians for the projectile and target, T_{pt} is the kinetic energy of the relative motion of projectile and target, and V_{pt} is the interaction potential. The scattering potential V_{pt} is divided into two parts: one with known solution, which contains the elastic scattering potential ($U_{elastic}$) including the Coulomb potential, and one that contains any residual potential, which mediate the charge-exchange ($W_{charge-exchange}$):

$$V_{pt} = U_{elastic} + W_{charge-exchange}. \tag{3.5}$$

The transition between the initial and final states is described by a T-matrix [3, 116]:

$$T_{fi} = \langle \Phi | U_{elastic} | \chi^+ \rangle + \langle \chi^- | W_{charge-exchange} | \Psi^+ \rangle, \tag{3.6}$$

where χ^+ and χ^- represent incoming and outgoing waves distorted by the mean field of the target ($U_{elastic}$). Ψ^+ is the solution of the Schrödinger equation in prior form, with an incoming plane wave and outgoing spherical wave. Φ is the incoming plane wave. The first term in equation 3.6, which is of isoscalar type, drops out because it does not connect the initial and final states of a charge-exchange reaction. Potential U is still used to determine the distortion of the incoming and outgoing waves. The remaining term describes the charge-exchange reaction.

T_{fi} is used to calculate the theoretical differential cross sections of the nuclear reaction.

$$\frac{d\sigma}{d\Omega} = \left(\frac{\mu}{2\pi\hbar^2}\right)^2 \frac{k_f}{k_i} |T_{fi}|^2. \tag{3.7}$$

where k_i and k_f are momenta of incoming and outgoing channels, respectively, μ is the reduced energy. For the charge-exchange reactions, T_{fi} is usually calculated by using:

$$T_{fi} = \langle \chi_f^+(\vec{k_f}, \vec{R'}) | F(\vec{R'}) | \chi_i^-(\vec{k_i}, \vec{R'}). \tag{3.8}$$

Equation 3.8 consists of the incoming and outgoing distorted waves χ_f^+ and χ_i^-, respectively, and a form factor, $F(\vec{R'})$, that describes the interaction between the projectile and the nucleons in the target.

The form factor is a double folding of the nucleon-nucleon (NN) interaction over the projectile and target-system transition densities. The transition densities for projectile and target systems contain the overlap between the initial and final states of these separate systems and directly relate to the transition strengths, such as the Gamow-Teller transition strengths. The transition densities and strengths are calculated in a nuclear structure model.

The DWBA calculations for the charge-exchange reactions used in this work are done by using the package known as FOLD [111], which consists of three modules: WSAW, FOLD, and DWHI. The module FOLD calculates the form factor $F(\vec{R'})$. Besides the nuclear-structure information obtained from a structure model, it requires a single-particle radial wave function of the orbitals of the nucleus involved in the calculation. These single-particle wave functions are calculated in WSAW. In addition, FOLD requires a NN-potential. In this work, we use the NN-interaction of Love and Franey [41, 37]. The form factor calculated in FOLD serves as input for DWHI, which is used for the distorted-wave calculation resulting in the transition matrix T_{fi} and the cross sections.

3.4 Inputs & Outputs for the DWBA Calculations

3.4.1 Single-Particle Wave Functions (WSAW)

As mentioned in the above section 3.3, one of the important ingredients needed to calculate form factor $F(\vec{R'})$ include single-particle wave functions calculated through the first module from

the FOLD package known as WSAW [111]. WSAW is used to calculate the radial part of the single-particle wave functions for the one-particle and one-hole states connected by the relevant transition operator. A Woods-Saxon potential is assumed, and for protons, the Coulomb potential is also included. In addition, a spin-orbit potential is included for both protons and neutrons. The necessary nuclear physics inputs to the WSAW calculations are the nuclear charge of the target nucleus, core mass, and the binding energies (BEs) of every single proton and neutron in orbitals that participate in the excitation. These BEs were obtained through the shell-model code NUSHELLX@MSU [115, 117] with the DENS function, employing the SK20 [118] interaction in ^{60}Ni and ^{60}Cu.

In WSAW, the depth of the Woods-Saxon potentials are varied to match binding energies for each of the single-particle orbitals separately. The Woods-Saxon potential has the general form:

$$f(R; r_n, a_n) = \frac{V_0}{1 + \exp\left(R - r_n A^{1/3}\right)/a_n}, \tag{3.9}$$

where V_0 is the maximum depth of the volume potential, r_n is the radius of the potential, A is the mass number of the target nucleus, and a_n is diffuseness of the potential [119]. In this work, the starting value of the Woods-Saxon potential is set to 60 MeV. The radius parameter r_n is fixed to 1.25 fm, and the diffuseness is fixed to 0.6 fm. The Coulomb potential has a radius parameter of 1.25 fm. The spin-orbit potential has a radial form that goes with $\frac{1}{r}$ times the derivative of the Woods-Saxon potential. The spin-orbit potential strength is set to 7 MeV. Note that, the program assumes a spin-operator of the form $\vec{L} \cdot \vec{\sigma}$ and that a factor of $\left(\frac{\hbar}{m_\pi c}\right)^2 \approx 2$ is already included.

Table 3.1 describes input parameters used in the WSAW program for target (^{60}Ni) and residual (^{60}Cu) system . The full input files are included in the Appendix A, Table A.1. The outputs are the radial wave functions for each of the orbitals involved in the calculation. The plots of these relevant single-particle wave functions are shown in Figure 3.2. Note that all wave functions are positive near r = 0 (by design) and are normalized such that $\int_0^\infty \psi(r) r^2 \, dr = 1$. The densities for ^{3}He-projectile and ^{3}H-ejectile system are calculated from Variational Monte-Carlo results [120].

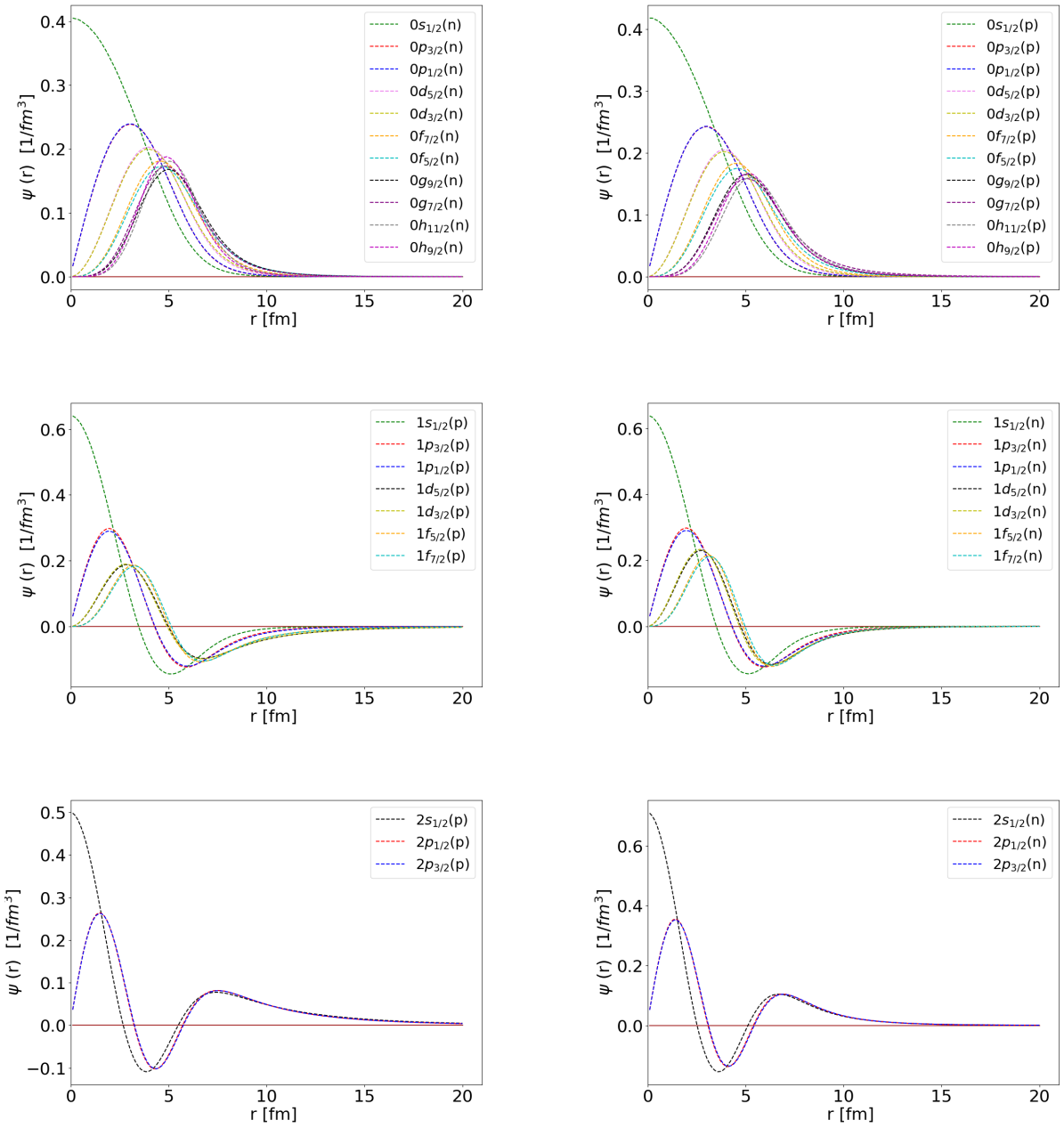

Figure 3.2 The Woods-Saxon radial single-particle wave functions calculated from the WSAW program for n=0 (top), n=1 (middle) and n=2 (bottom). The left panels show single-particle wave functions for protons and on right panels, for neutrons.

Table 3.1 Description of the input parameters in the WSAW file for calculating single-particle wave functions as shown in the Appendix A, Table A.1- A.3.

Particle	Input parameters	Meaning of the input values
line number 1	0.1 fm 20 fm 1 150	Step size for radius Maximum value of radius Step size (first point) Total number of points needed to plot radius
line number 2	Ni60Cu60	File name containing radial wave functions
line number 3	59 60 .65 fm 1.25 fm 1.25 fm 7.0 MeV	Core mass of target nucleus Starting value of the volume potential depth Diffuseness of the potential Radius parameter of the potential Coulomb radius parameter Spin-orbit potential strength
For each orbital a line with	x MeV 1. l n 1. j s	Binding energy of paricle (proton or neutron) Mass number of particle Orbital angular momentum of proton Number of interior nodes for this particular particle Charge of particle (either 0 or 1) Total angular momentum of the particle orbit Spin of the particle

3.4.2 Calculation of the Formfactor (FOLD)

The FOLD program [111] is used to calculate the form factor $F(\vec{R}')$:

$$F(\vec{R}') = \langle \Phi_e \Phi_r | V_{eff} | \Phi_t \Phi_p \rangle \tag{3.10}$$

where Φ_e, Φ_r, Φ_t, and Φ_p are the wave functions of the ejectile, residual, target, and projectile, respectively, and V_{eff} is the effective nucleon-nucleon (NN) interaction between nucleons in the target and projectile nuclei. The ingredients for the calculation of the formfactor are the single particle wave functions from WSAW, the effective NN interaction, and one-body transition densities (OBTDs) calculated in the NORMOD code [121], which is discussed later in this section. The formfactors are calculated from these ingredients by a double-folding of the effective NN interaction over the transition densities of the projectile-ejectile and target-residual systems. The double-folding over the transition densities of the participant nuclei in the reaction is necessary to account for the composite nature of the nuclei involved.

The phenomenological nucleon-nucleon interaction used to model charge-exchange reactions were described by Love and Franey in 1981 through a phaseshift analysis of NN scattering data [37]. Later on, with an updated data set, this interaction was improved by Franey and Love in 1985 [41]. The Love and Franey interaction is particularly useful in the charge-exchange studies since V_{eff} is parameterized in terms of the central (V_C), spin-orbit (V_{LS}), and tensor (V_T) terms contributing to the interactions that are of interest for charge-exchange reactions. It takes the following form:

$$V_{ij} = V_C(r_{ij}) + V_{LS}(r_{ij})\vec{L}\cdot\vec{S} + V_T(r_{ij})S_{ij}, \tag{3.11}$$

where S_{ij} is the tensor operator, defined as

$$S_{ij} = 3\frac{(\vec{\sigma}_i\cdot\vec{r}_{ij})(\vec{\sigma}_j\cdot\vec{r}_{ij})}{r_{ij}^2} - \vec{\sigma}_i\cdot\vec{\sigma}_j \tag{3.12}$$

The radial dependence of each term is expanded as a sum of Yukawa potentials,

$$V(r) = \sum_i V_i Y(r/R_i), \tag{3.13}$$

where $Y(x) = \frac{e^{-x}}{x}$. The parameters V_i and the ranges R_i are fit to nucleon-nucleon scattering data. The result of the work by Love and Franey provides effective NN T-matrix interaction strengths applicable at various incident beam energies. For the case of the ^{60}Ni(^{3}He,t) reaction at the E_x = 420 MeV, the Love and Franey interaction at 140 MeV/u was used.

Information about the transitions for which differential cross sections are calculated come in the form of one-body transition densities (OBTDs), which are amplitudes for one-particle one-hole (1p-1h) excitations that are connected by the specific operators of Eq. 2.1 for each of the transitions. The OBTDs for all giant resonances being investigated in the ^{60}Ni(^{3}He,t) reaction were calculated in a normal-modes formalism and the calculations were performed with the NORMOD code [121]. Unlike the shell-model calculations with Nushellx (see section 3.4), in the normal-modes formalism, the OBTDs are calculated by producing the most coherent superposition of the 1p-1h excitations, thereby maximizing the transition strength.

For the normal-modes calculations, it was assumed that the 28 protons fill all single-particle shells up to $0f_{7/2}$. The 32 neutrons are assumed to also fill the $0f_{7/2}$ shell and the $1p_{3/2}$ shell,

as shown in Figure 3.3(a). Figure 3.3(b) and (c) show examples for the exciting of two isovector transitions in the ^{60}Ni(^{3}He,t) reaction.

Table 3.2 describes the input parameters of the NORMOD input file. The full NORMOD input file and the output tables of the OBTDs for each giant resonance being investigated in this work are included in the appendix B, Table B.1-B.2 and Tables B.3-B.15 respectively. The plots of the radial transition densities, which represent the overlaps between the initial and final states in the target nucleus, for all giant resonances being investigated in this work as listed in Table 2.1 are shown in Figure 3.4. These are calculated in FOLD code, and serve as input for the formfactor calculation.

Finally, the formfactors for each giant resonance are calculated. Given the total angular momentum transfer in the projectile (^{3}He,t) system, ΔJ_p, and the total angular momentum transfer in the target (^{60}Ni,^{60}Cu) system, ΔJ_T, the relative angular momentum transfer is calculated with:

$$\Delta J_R = \Delta J_p \oplus \Delta J_T, \tag{3.14}$$

where $\Delta J_p = \Delta L_p + \Delta S_p$ equals either 0 ($S_p = 0$) or 1 ($S_p = 1$), since $\Delta L_p = 0$. ΔJ_T is defined by the type of giant resonance excited. Since $\Delta L_p = 0$, the orbital angular momentum transfer in the target system ΔL_T, defines the charge in parity:

$$(-1)^{\Delta L_T} = (\pi_i \cdot \pi_f)_{\Delta T}, \tag{3.15}$$

where π_i is the parity of the ^{60}Ni ground state and π_f is the parity of the final state in ^{60}Cu. Since the ^{60}Ni ground state has a spin-parity of 0^+, $\pi_i = 1$. π_f is negative (positive) if ΔL_T = odd (even). Note that for certain excitations, two sets of formfactors contribute. For example for $0^+ \rightarrow 1^+$ excitations, $\Delta J_p = 1$ and $\Delta J_T = 1$, allowing for both $\Delta J_R = \Delta L_T = 0$ and $\Delta J_R = \Delta L_T = 2$. Because of the tensor interaction in the nucleon-nucleon interaction, the two components interfere with each other. However, for strong excitations such as the giant resonances, the impact of such interferences is small [20]. For the MDA, only formfactors with pure $\Delta J_R = \Delta L_T$ are used, as its purpose is to decompose contributions with different ΔL_T. Each type of transition as listed in Table 2.1 requires its own FOLD input file. Table 3.3 describes the input parameters of the FOLD input file. Example of FOLD input files for several transitions are included in the Appendix C, Tables C.1 - C.7. The

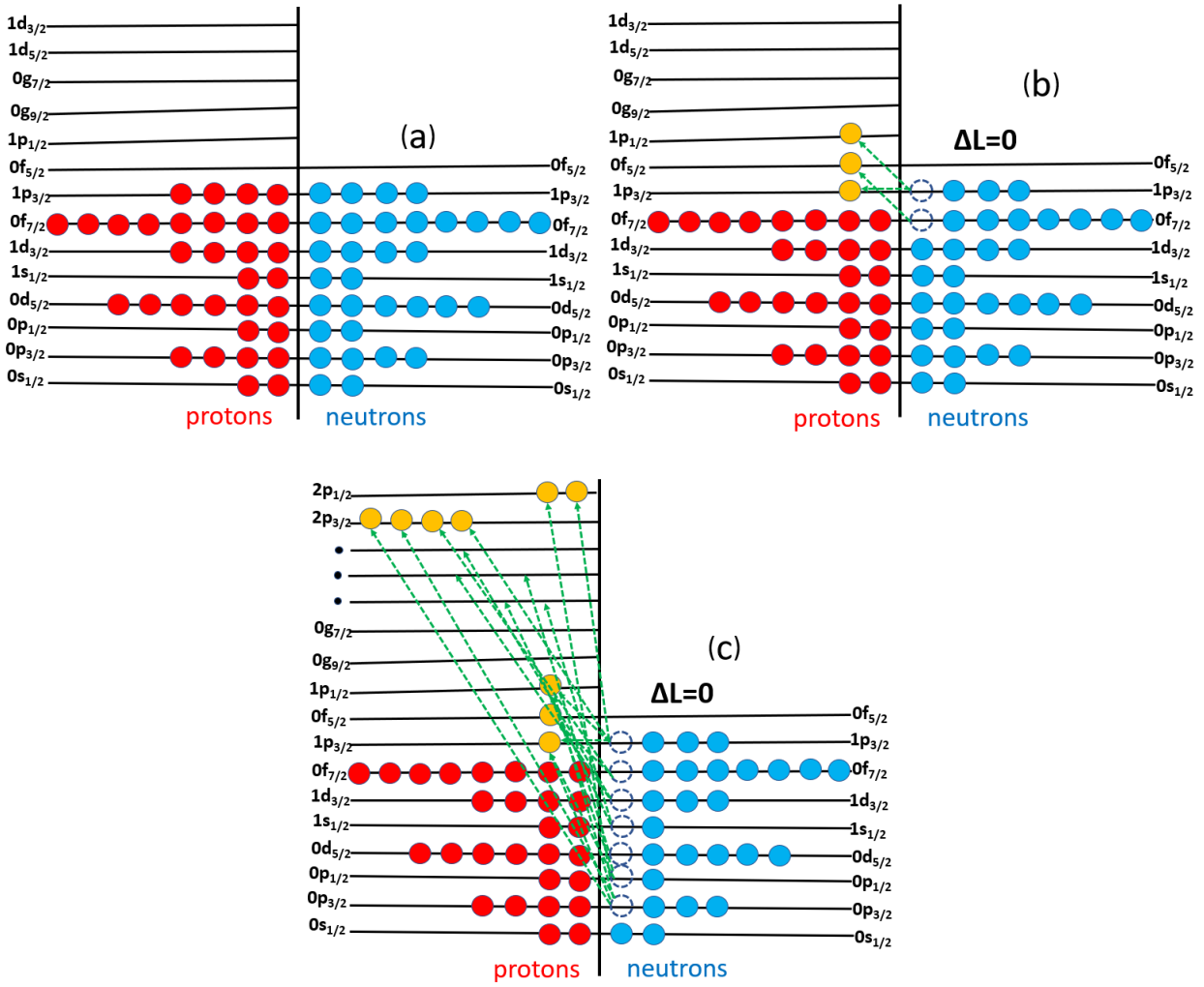

Figure 3.3 Figure (a) shows the configuration of ^{60}Ni ground state assumed in the NORMOD calculations. Protons are in red color, they fill single particle shells up to $0f_{7/2}$, while neutrons are in blue color and fills up to the $1p_{3/2}$ shell. Figures(b) and (c) are examples of the exciting GT and IVSGMR transitions respectively. The GT transition can only populate states in ^{60}Cu with pf-shell contributions (^{60}Ni[g.s] $\rightarrow$ ^{60}Cu[$0\hbar w$]) while IVGMR transition can populate states in ^{60}Cu with pf, sdg and pfh-shell contributions (^{60}Ni[g.s] $\rightarrow$ ^{60}Cu[$2\hbar w$])).

outputs of each FOLD input file are the formfactors as discussed above, which are shown in Figures 3.5 and 3.6. Since the NN interaction has real and imaginary terms, the formfactors also have real and imaginary components. Note that excitations involving the transfer of spin ($\Delta S = 1$) have strong real formfactors, while those without the transfer of spin ($\Delta S = 0$) have strong imaginary formfactors.

Table 3.2 Description of the input parameters in the NORMOD input file for calculating OBTDs useful for FOLD input files for each giant resonance being investigated as shown in the Appendix C, Tables C.1 - C.7.

Line number	Input parameters	Meaning of the input values
line number 1	1	Wave functions are defined to be positive near origin
line number 2	14	Number of proton shells
line number 3 to 16: Protons		Describing parameters of every single proton orbit
Column number 1	n-value	Number of nodes in particular wave Function
Column number 2	L-value	Angular momentum of proton
Column number 3	2J-value	Twice total angular momentum of single particle wave function
Column number 4	1.0	Fullness of proton-shell
Column number 5	1 or 0	1 for proton, 0 for neutron
Column number 6	$\mathbf{n}\hbar\omega$	**n** is major shell number of proton
Column number 7	**x**-value	**x** is an arbitrary number for each shells
line number 17	11	Number of neutron shells
line number 18 to 28: Neutrons	Same as 3 to 16	Same description as line 3 to 16
line number 29	IAS	Parameters describing IAS
line number 30	GT	Parameters describing GT transition
line number 31-33	Dipoles	Parameters describing Dipoles transition
line number 34	IVGQR	Parameters describing IVGQR transition
line number 35-37	IVSGQR	Parameters describing IVSGQR transition
line number 38	IVGMR	Parameters describing IVGMR transition
line number 39	IVSGMR	Parameters describing IVSGMR transition
line number 40	Octupole	Parameters describing Octupole transition
Column 1	M-value	Discussed in operator of Eq. 2.1
Column 2	ΔJ	Total transferred angular momentum
Column 3	J^{π}	Product of parities
Column 4	m	Mass number of target
Column 5	T	Isospin transfer
Column 6	1	reaction type (T=1) for CE reactions
Column 7 and 8	$\Delta n\hbar\omega$	Minimum and Maximum difference between major shells number

Table 3.3 Description of the input parameters in the FOLD files for calculating transition densities and formfactors as shown in the Appendix C, Tables C.1 - C.7.

Line number	Input parameters	Meaning of the input values
line number 1	1	Selects CE reaction type
	1FOLDNI	File name to save formfactors
line number 2 to 7	600	Total number of integration steps
parameters of (^{3}He,t)	0.03	Step size (fm)
	420	Beam energy (MeV)
	3	Mass of projectile (^{3}He)
	1	set to be 1 for printout for r-space densities
	1	set to be 1 for printout for q-space densities
	1	set to be 1 for printout for formfactors
line number 3	0.5^+	Spin and parity (J^π) of ejectile (^{3}H)
	0.5^+	Spin and parity (J^π) of projectile (^{3}He)
line number 4	0.5	Isospin (T) of ejectile (^{3}H)
	+0.5	Isospin projection (T_z) of ejectile (^{3}H)
	0.5	Isospin of projectile particle (^{3}He)
	-0.5	Isospin projection of projectile particle (^{3}He)
line number 5	3 3 0.000	Selection of format of OBTDs particle
line number 6	1	Single-particle wave function (ex: $0s_{1/2}$)
	1	hole-particle wave function (ex: $0s_{1/2}$)
	ΔJ_p	1 for spin transfer and 0 for no spin transfer
	0.707	OBTD for (^{3}He,t) system
line number 7	-1 -1	fixed end line
line number 8	HE3H3	File name of projectile and ejectile
line 9 to 10 same as	$\Delta J^\pi_R = 1^+$ for GT	Relative final spin and parity of each transition
3 to 4 but for (^{60}Ni,^{60}Cu)	$J^\pi = 0^+$ for ^{60}Ni	Initial (ground) spin and parity of target
line number 10	1 (2 for IAS)	Isospin (T) of residual (^{60}Cu)
	1	Isospin projection (T_z) of residual (^{60}Cu)
	2	Isospin (T) of target (^{60}Ni)
	2	Isospin projection of target (^{60}Ni)
line 11 same as 5	3 3 0.000	Selection of format of OBTDs
line number 13 to x-line	OBTDs (1p-1h)	Values calculated from NORMOD code
Column 1	1p	Single-particle wave function
Column 2	1h	hole-particle wave function
Column 3	ΔJ_T	Depends on type of giant resonance excited
Column 4	0.0	ignored
Column 5	value	OBTD
line number 14	-1 -1	fixed end line
line number 15	Ni60Cu60	File name containing radial wave functions

Table 3.4 Description of the input parameters in the FOLD file for calculating transition densities and formfactors, a continuation of Table 3.3.

line number 16	0.939	Scaling parameter for transformation of interaction strengths from NN system to nucleon-nucleon system
	2.650	Momentum parameter used to calculate exchange contribution.
	1.000	Not used.
	Love and Franey NN interaction	Filename contains parameters at 140 MeV/u.
line number 17	1 or 2	Number of formfactor(s).
line number 18	ΔJ_R	Relative spin transfer
	J_P	Total angular momentum for each formfactor
	J_T	Total angular momentum transfer in the target system
	-1	Select components of NN interaction (the -1 is all components)
line number 19-20 or 19-22	Fixed values	Scaling factors for formfactor components. (Usually set to 1)

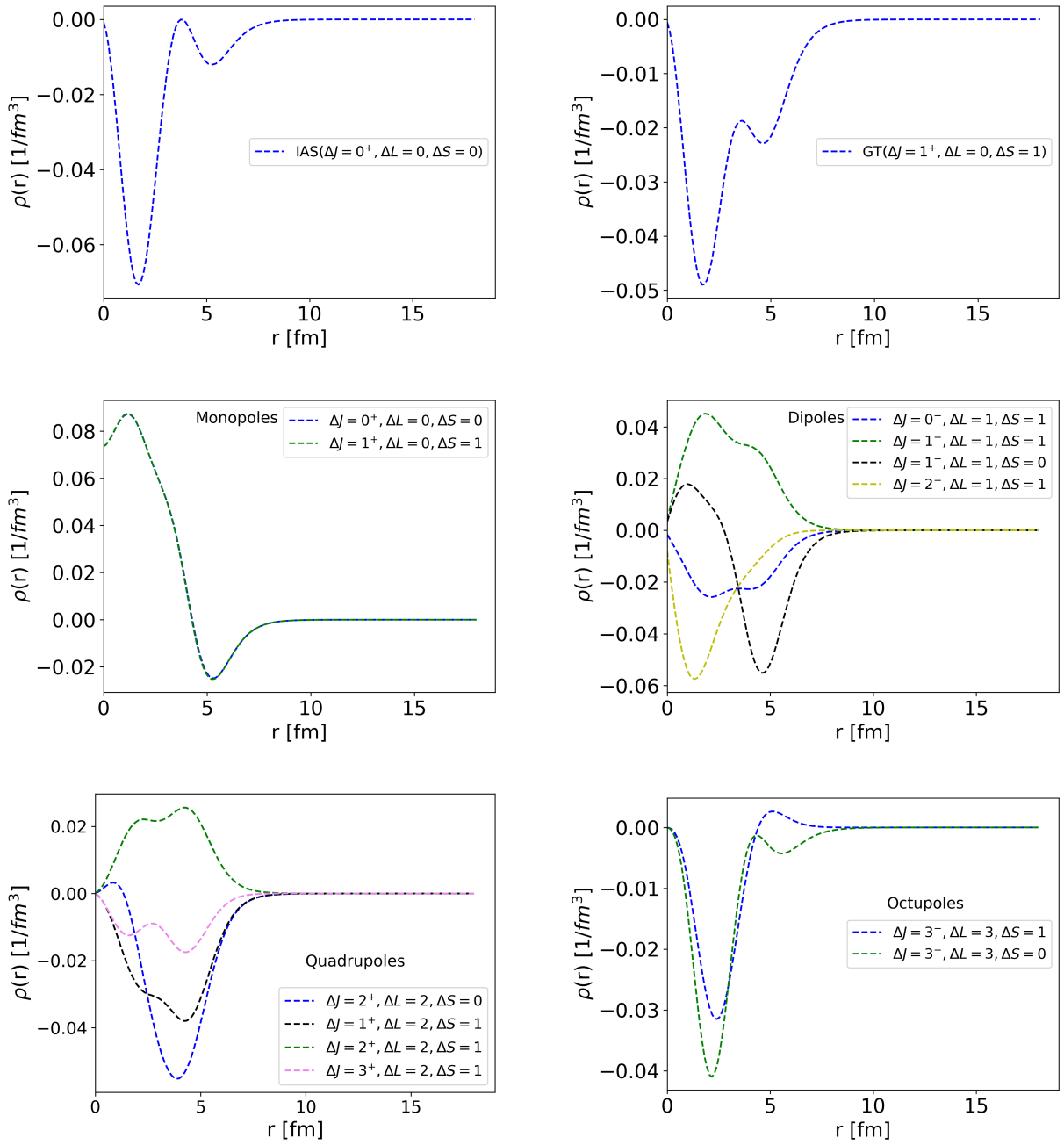

Figure 3.4 Transition densities calculated from FOLD code for a target nucleus (^{60}Ni) of the IAS, GTR, monopoles, dipoles, quadrupoles, and octupoles transitions being investigated in this work as all listed in Table 2.1.

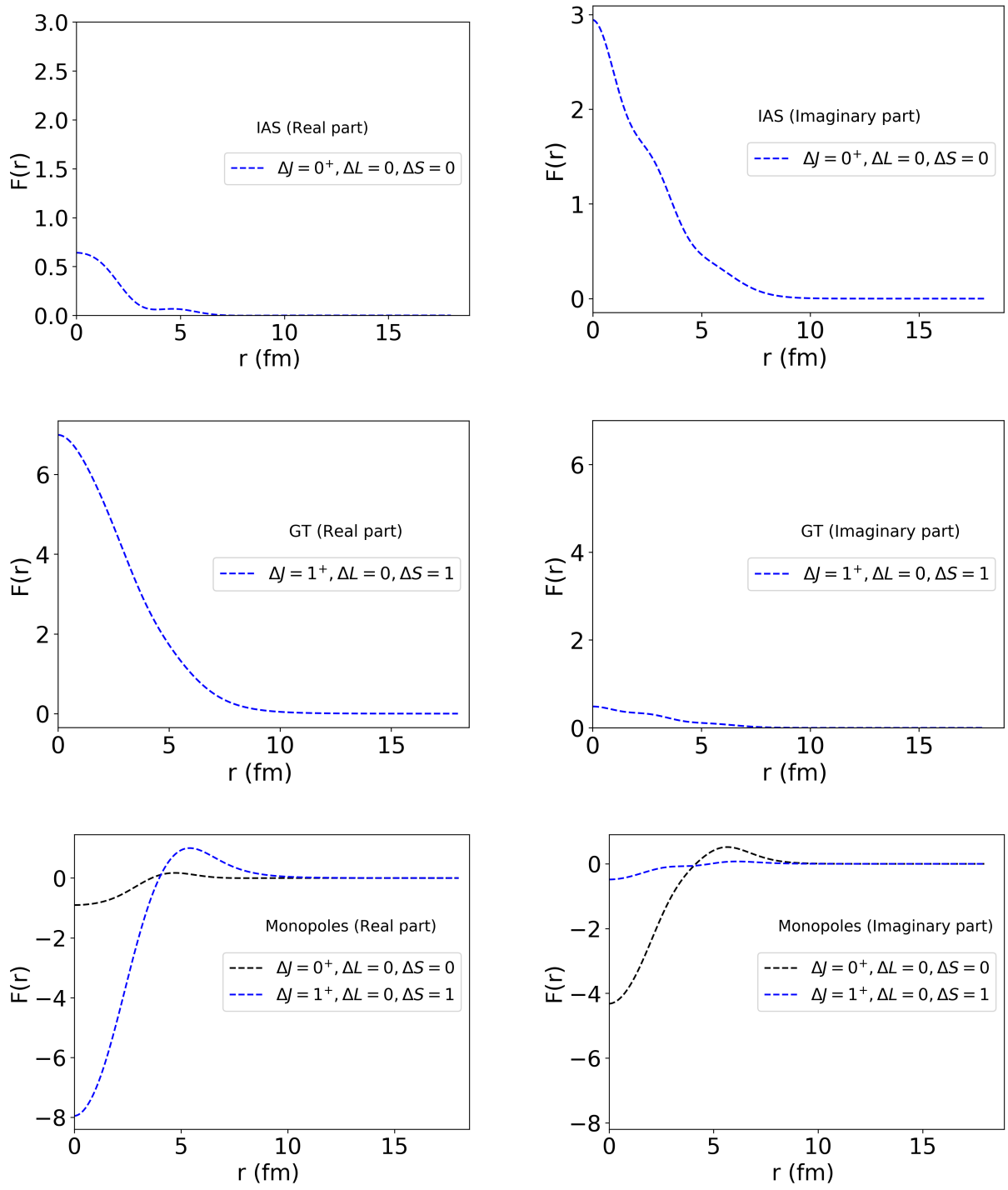

Figure 3.5 The real (left panels) and imaginary (right panels) part of the formfactors for transitions listed in the panels. They were calculated in the FOLD code. The excitations with spin transfer (ΔS = 1) have strong real formfactors, while these without spin transfer (ΔS = 0) have strong imaginary formfactors. Also note that the $2\hbar w$ resonances have a node in the formfactior.

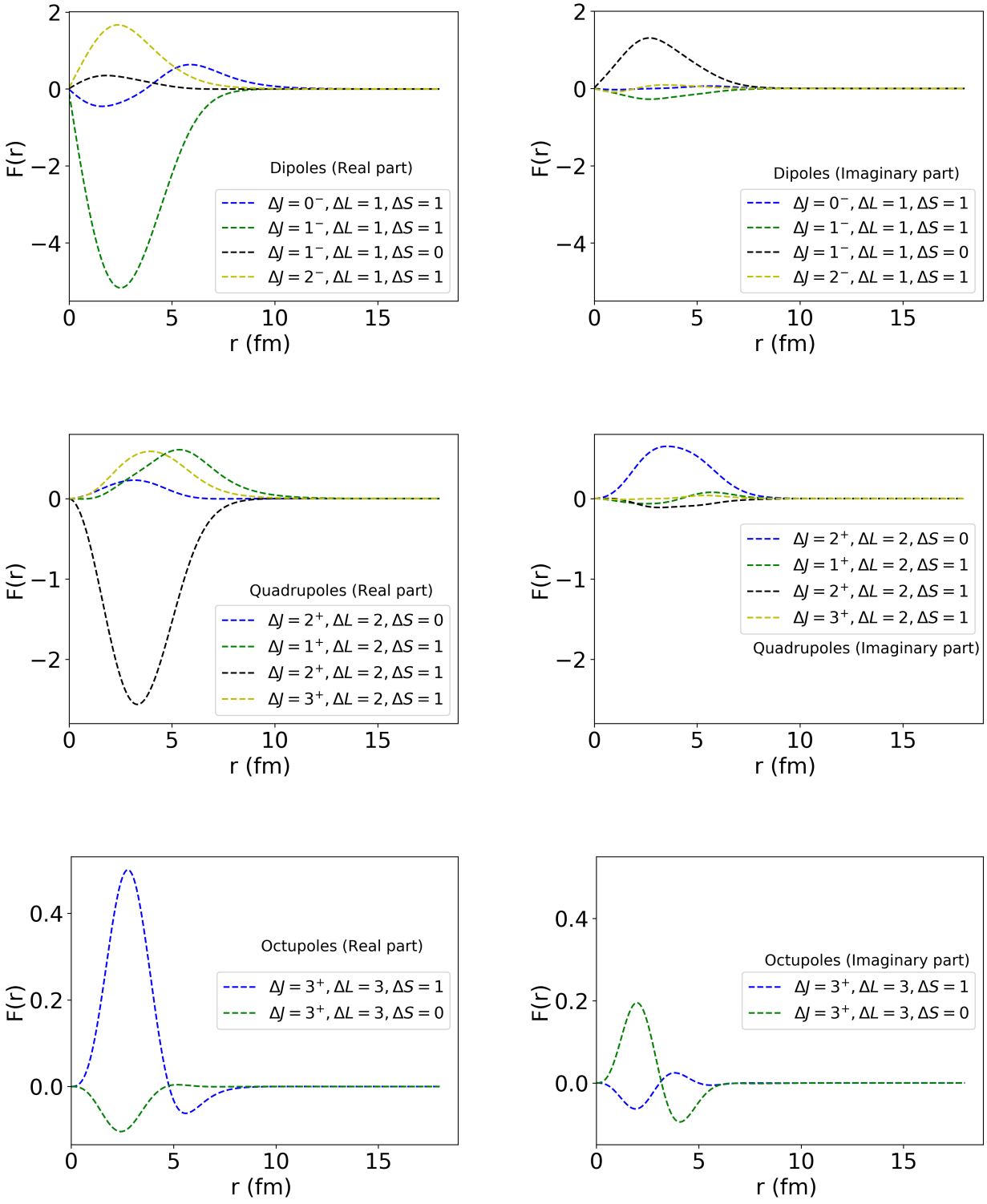

Figure 3.6 The real (left panels) and imaginary (right panels) part of the formfactors for transitions listed in the panels. They were calculated in the FOLD code. The excitations with spin transfer ($\Delta S = 1$) have strong real formfactors, while these without spin transfer ($\Delta S = 0$) have strong imaginary formfactors.

3.4.3 Calculation of Differential Cross Section (DWHI)

The final part of the FOLD package, called DWHI, calculates the transition matrix elements, T_{fi} in Eq. 3.7 and the differential cross sections. The DWHI code uses the previously calculated formfactor (see Eq. 3.10) together with the optical model potential (Eq. 3.9) as the ingredients. The optical potential distorts the incoming and outgoing waves. The real and imaginary optical potential parameters (depths of the potential, radius and diffuseness) used in this work for the ^{60}Ni-^{3}He and ^{60}Cu-^{3}H systems, were taken from measurement of ^{3}He elastic scattering on ^{58}Ni at 443 MeV [119]. The potential depths of ^{60}Cu-^{3}H system were scaled to 85% of the one of ^{60}Ni following the procedure in Ref. [122], while the other parameters remain the same. The potential parameters are shown in Table 3.5.

Table 3.5 Optical potential parameters used in DWHI calculations for ^{60}Ni(^{3}He,t)^{60}Cu reaction at 140 MeV/u. These values were taken from Ref. [119]. and defined for ^{3}H following Ref. [122].

Nuclides	V [MeV]	r_v (fm)	a_v [fm]	W [MeV]	r_w [fm]	a_w [fm]
^{60}Ni + ^{3}He	35.16	1.32	0.84	44.43	1.021	1.018
^{60}Cu + ^{3}H	29.89	1.32	0.84	37.77	1.021	1.018

As discussed in section 3.4.2, each giant resonance listed in Table 2.1 requires its own DWHI input file. Table 3.6 describes the input parameters of the DWHI input files. Examples of DWHI input files for several transitions are included in the Appendix D, Tables D.1 - D.14. The output of each DWHI calculation file is shown in Figure 3.7. The differential cross sections will be used in the data analysis and serve as inputs for the MDA (Eq. 3.2. The results from MDA calculation are discussed in Chapter 5.

Table 3.6 Description of the input parameters in the DWHI files for calculating the angular distributions for each giant resonance as shown in the Appendix D, Tables D.1 - D.14.

Line number	Input parameters	Meaning of the input values
line number 1	1210000041000000	Options for calculation and plotting cross sections for each form factor
line number 2	FOLDNI	File name containing form factor
line number 3	40 0 0.2	Total number of angle used Initial angle Angle step size
line number 4	value-1=160 value-2=1 or 2 value-3=1 value-4=1 value-5=0 value-6	Number of partial waves for elastic Number of form factors to expect must match number produced by FOLD $2 \times \Delta$J-projectile spin in initial channel (^{3}He) $2 \times \Delta$J-ejectile spin in final channel (t) $2 \times \Delta$J-target spin initial channel (^{60}Ni) $2 \times \Delta$J-residual transfer (^{60}Cu)
line number 5	value-1=0.03 value-2=600	Step size Total number of integration steps
line number 6 (For incoming channel)	value1= 420 value-2 = 3 value-3 = 2 value-4 = 60 value-5 = 28 value-6 = 1.25 value-7=1 value-8=0	Beam/lab energy Projectile (^{3}He) mass number Projectile proton number Target (^{60}Ni) mass number Target proton number Coulomb radius Twice the spin value of the incident projectile Not used in entrance channel
line number 7 (Real part of optical potential parameters of ^{60}Ni-target) (Imaginary part of optical potential parameters of ^{60}Ni-target)	value-1=1 value-2=-35.16 value-3=1.32 value-4=0.84 value-5=0 value-6=-44.43 value-7=1.021 value-8=1.018 value-9=0 value-10=0	Woods-Saxon potential (WS) Real well depths of WS potential Radius Diffuseness Indicate that beam energy used (420 MeV) is the lab energy or reaction Q-value Imaginary well depths of WS potential Radius Diffuseness Imaginary spin-orbit factor (not used) Computing factor (not used)
line number 8	value=0	Fixed end line

Table 3.7 Description of the input parameters in the DWHI file for calculating the angular distributions. Continuation of Table 3.6.

line number 9 (For outgoing channel)	value-1= −6.2 value-2 = 3 value-3= 1 value-4= 60 value-5= 29 value-6= 1.25 value-7=1 value-8=0	Q-value Ejectile (t) mass number Ejectile proton number Residual (^{60}Cu) mass number Residual proton number Coulomb radius Twice the spin value of the ejectile Not used in entrance channel
line number 10 (Real part of optical potential parameters of ^{60}Cu-residual) (Imaginary part of optical potential parameters of ^{60}Cu)	Value-1=1 value-2=-37.77 value-3=1.021 value-4=1.018 value-5=0 value-6=-44.43 value-7=1.021 value-8=1.018 value-9=0 value-10=0	Wood-Saxon potential Real depth of WS potential Radius Diffuseness Indicate that beam energy used (420 MeV) is the lab energy or reaction Q-value Imaginary depth of WS potential Radius Diffuseness Imaginary spin-orbit factor Computing factor
line number 11	value=0	Fixed end line
line number 12	ΔJ_R $2 \times J_P$ $2 \times \Delta J_T$	Relative spin transfer Same as J_P in FOLD Same as J_T in FOLD
line number 13	0 0 0 1	Fixed line ending form factor, where 0. terminate further form factor and 1. enter data for single form factor
line number 14	Plot filename	Filename of output

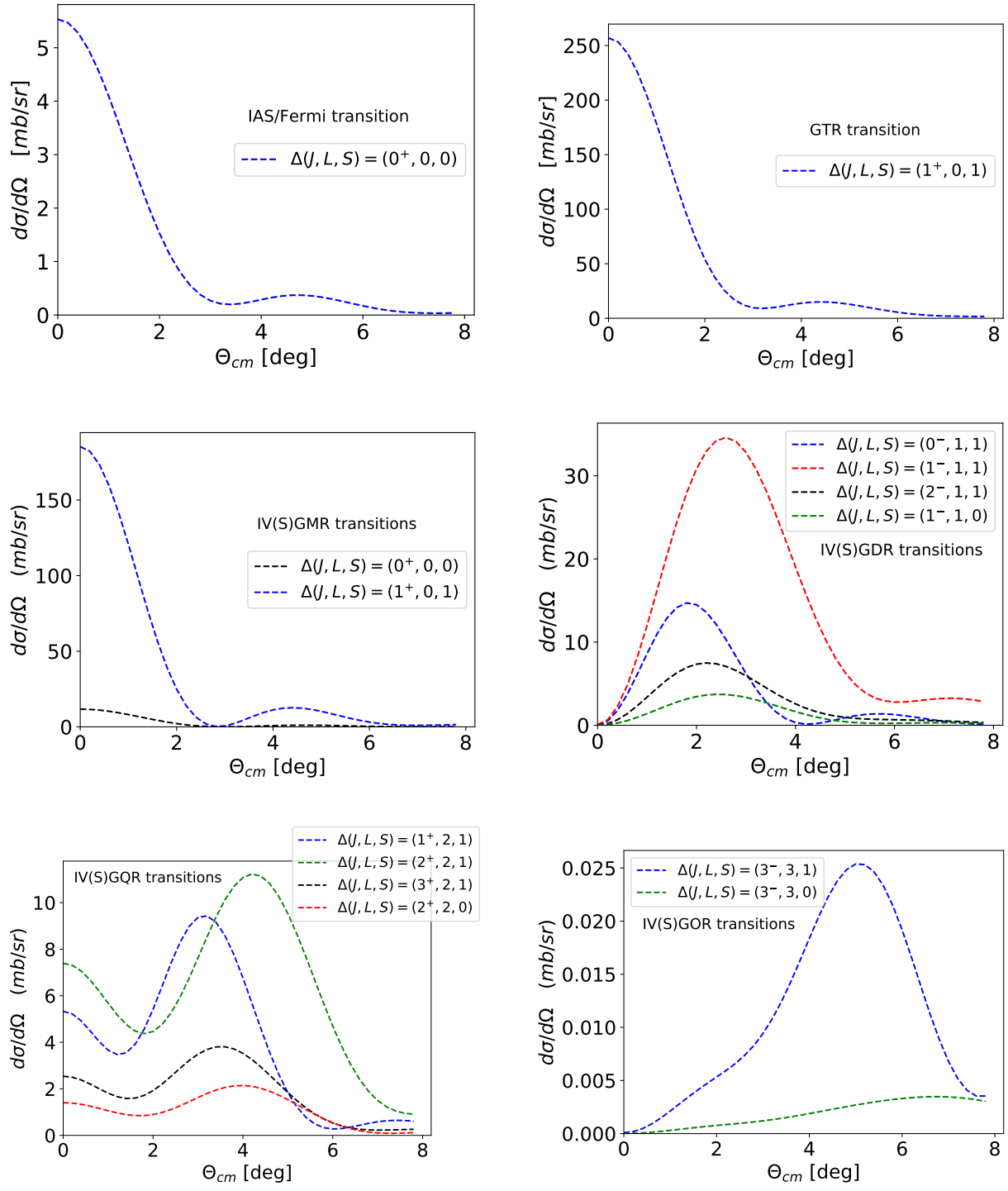

Figure 3.7 Differential cross sections calculated for the following giant resonances excited via the ^{60}Ni(^{3}He,t) reaction: the isobaric analog state (top-left), Gamow-Teller resonance (top-right), isovector(spin) monopole resonances (middle-left), isovector (spin) dipole resonances (middle-right), isovector (spin) quadrupole resonances (bottom-left) and isovetor (spin) octupole giant resonances (bottom-right).

3.5 Eikonal Approximation and the Unit Cross Section for GT and IAS

The extraction of Gamow-Teller strength, $B(\mathrm{GT})$, can be performed directly via a β/EC decay half-life measurement. However, β-decay can only populate states in the daughter nucleus that are energetically accessible given the Q-value of the transition. As shown in Figure 3.8, CE reactions are not limited by a Q-value, and transitions to high-lying states can be studied. CE reactions are mediated by the strong force, and the weak force mediates β-decay. However, the operators involved in each process are both of the same $\boldsymbol{\sigma\tau}$ type and the initial and final states that are connected by this operator are the same. It turns out that, at intermediate beam energies, the differential cross sections, $\left(\frac{\mathrm{d}\sigma}{\mathrm{d}\Omega}\right)_{\Delta\mathbf{L}=0}$, at small momentum transfer ($\mathbf{q} \approx 0$) measured via charge-exchange reactions is proportional to the Gamow-Teller strength of the transition [123]. This proportionality was experimentally shown by Taddeucci *et al* [123, 19, 20, 124], and is given by:

$$\left(\frac{d\sigma}{d\Omega}(\mathbf{q}=0)\right)_{\Delta L=0} = \hat{\sigma} B(\mathrm{GT}), \tag{3.16}$$

where the $\hat{\sigma}$ is the proportionality constant, called the unit cross section. For this proportionality to hold, the $\Delta\mathrm{L} = 0$ component of the differential cross section must be used, which can be obtained through the multipole decomposition analysis described in section 3.1 and 5.2. In the Eikonal approximation, the unit cross section can be decomposed:

$$\hat{\sigma}_{\mathrm{GT}} = KN|J_{\sigma\tau}|^2, \tag{3.17}$$

where $\hat{\sigma}_{\mathrm{GT}}$ is the Gamow-Teller unit cross sections, K is a kinematical factor, carrying information about masses and energies of particles, and is expressed in terms of incoming and outgoing wave momenta ($\mathrm{k_i}$ and $\mathrm{k_f}$) and their corresponding initial and final reduced energies ($\mathrm{E_i}$ and $\mathrm{E_f}$):

$$\mathrm{K} = \frac{\mathrm{E_i E_f}}{(\pi\hbar^2\mathrm{c}^2)^2}\frac{\mathrm{k_f}}{\mathrm{k_i}}, \tag{3.18}$$

N is a distortion factor defined by the ratio of the DWBA to the PWBA (plane-wave Born approximation) cross sections [123, 19]:

$$\mathrm{N} = \left(\frac{\sigma^{\mathrm{DWBA}}}{\sigma^{\mathrm{PWBA}}}\right), \tag{3.19}$$

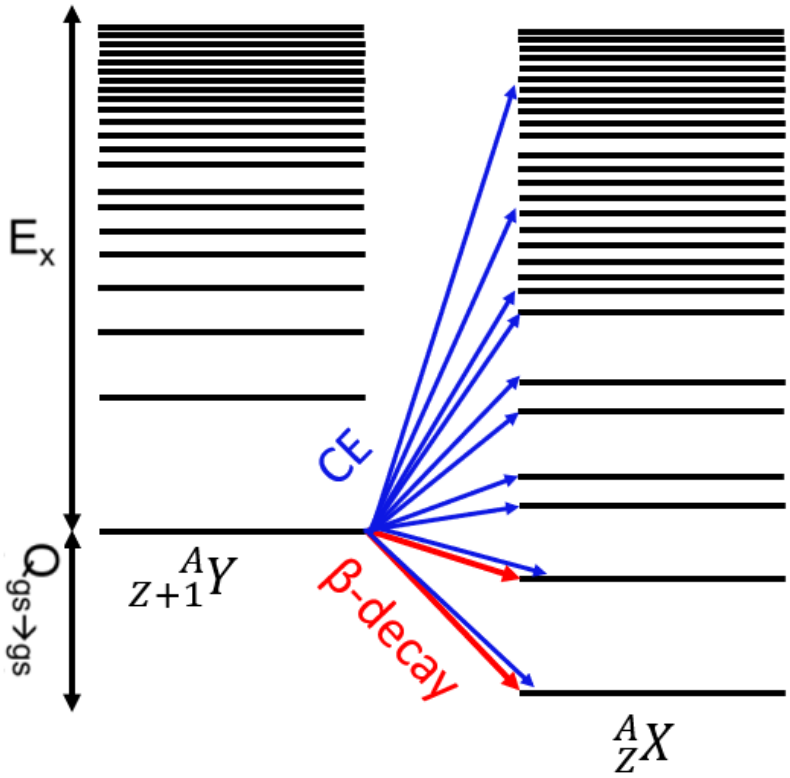

Figure 3.8 Schematic representation of both β-decay (red colors) and CE reactions (blue colors) from parent nucleus Y to the daughter nucleus X. β-decay can only populate states in the daughter nucleus that are energetically accessible with the Q-value of the decaying nucleus. However, CE reactions are not limited by Q-value, and highly excited states (nuclei that do not β-decay) can be studied via CE reactions.

and $J_{\sigma\tau}$ (or J_{τ}) is the volume integral of the corresponding effective NN interaction (see Eq. 3.11) between the projectile and target nucleons. In practice, σ_{GT} is conveniently calibrated by using transitions for which the transition strengths are known from β/EC decay and one does not have to rely on a calculation. This makes the extraction of GT strength model independent, which is very important for testing theoretical models. Of course, not for all nuclei are measured GT strength from β/EC decay available. However, the unit cross sections for Gamow-Teller transitions in such cases can be calculated by using expressions that only depend only on the mass number (A) of the nucleus which have been established experimentally. For (^{3}He,t) reactions at $E \approx 420$ MeV, this relationship is $\hat{\sigma}_{GT} = 109/A^{0.65}$ as shown in Figure 3.9. The proportionality described above for GT transitions also hold for the Fermi transition to the IAS and the mass dependent $\hat{\sigma}_F$ is also included in Figure 3.9.

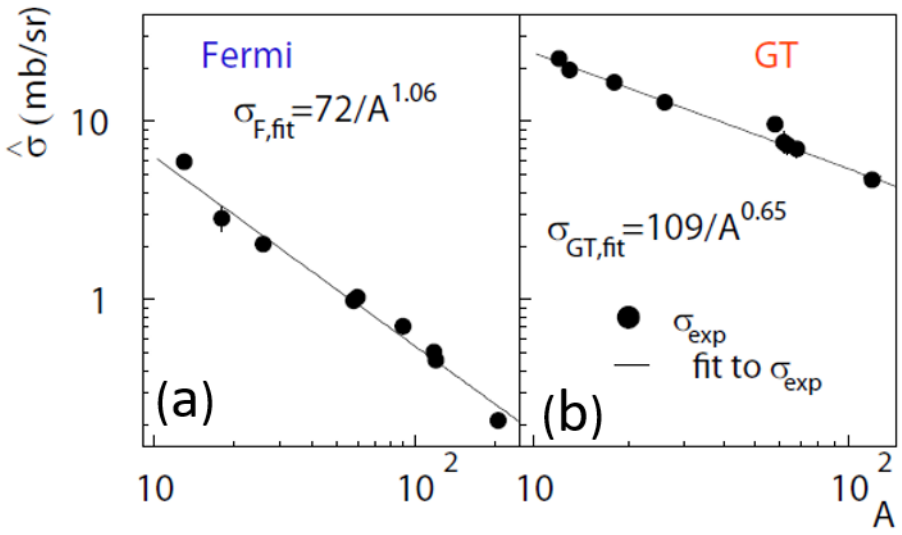

Figure 3.9 Figures (a) and (b) are measured of Fermi and Gamow-Teller unit cross sections respectively, as a function of mass number (A) for (^{3}He,t) reaction at 420 MeV. Both figures are taken and modified from Ref. [19].

The proportionality between strength and differential cross sections holds for beam energies of $E \gtrsim 100$ MeV/u. This energy is sufficiently high to strongly reduce the contribution of multistep processes to the CE reaction. The proportionality has the least uncertainty for strong transitions. For weak transition, interference between the $V_{\sigma\tau}$ and $V_{T\tau}$ components of the NN interaction become significant [19]. The uncertainty as a function of B(GT) was estimated to be $\sigma_{rel.syst.error} \approx 0.03 - 0.035ln[B(\mathrm{GT})]$. For example, states at $E_x = 2.07[B(\mathrm{GT}) = 0.091]$ and $E_x = 2.74[B(\mathrm{GT}) = 0.113]$, standard deviations of 11.4% and 10.6% were expected, respectively [20].

CHAPTER 4

DATA ANALYSIS: ^{60}Ni(^{3}He, t) REACTION AT RCNP

This dissertation focuses on probing isovector giant resonances in ^{60}Ni up to high excitation energies (60 MeV) using the (^{3}He,t) reaction at 140 MeV/u. The experiment was performed at the Grand Raiden Spectrometer (GRS) at Osaka University's Research Center for Nuclear Physics (RCNP). The method involved directing a ^{3}He beam at 420 MeV produced by the RCNP Ring Cyclotron with an intensity of $\sim$ 4 pnA on a ^{60}Ni foil target of 2 mg/cm^2. Section 4.1 describes the experimental setup, procedures, and devices. An overview of the GRS and its focal plane detectors are discussed in section 4.2 and 4.3, respectively. The method used to extract the excitation energy spectrum from ^{60}Ni(^{3}He,t) reaction was the missing-mass method, discussed in section 4.4. The magnetic fields of GRS and the angular acceptance are discussed in section 4.6 and 4.5, respectively. The measured differential cross sections from ^{60}Ni(^{3}He,t) data are discussed in section 4.7.

4.1 Experimental Setup, Procedures & Devices

The ^{60}Ni(^{3}He,t) experiment was performed at the Research Center for Nuclear Physics (RCNP) in Osaka University, Japan by using a primary ^{3}He beam of 140 MeV/u and the high-resolution QQDD-type Grand Raiden Spectrometer described in section 4.2. The spectrometer was set at -0.5° relative to the beam axis. The intermediate-energy ^{3}He^{2+} beam at the RCNP facility has been used extensively in various experiments for studying the Gamow-Teller strength distribution and other giant resonances via (^{3}He,t) reactions at intermediate beam energies [19, 119, 125, 126, 127]. The Azimuthally Varying Field (AVF) and Ring cyclotrons shown on Figure 4.1 were coupled to accelerate a beam of ^{3}He nuclei to 420 MeV and transported to the target through the WS beam line [128] connecting the separated-sector Ring Cyclotron and the GRS. Beam intensities of up to 4 pnA were impinged on a ^{60}Ni-target foil of 2 mg/cm^2 installed in the scattering chamber. The ^{60}Ni target was 98% pure.

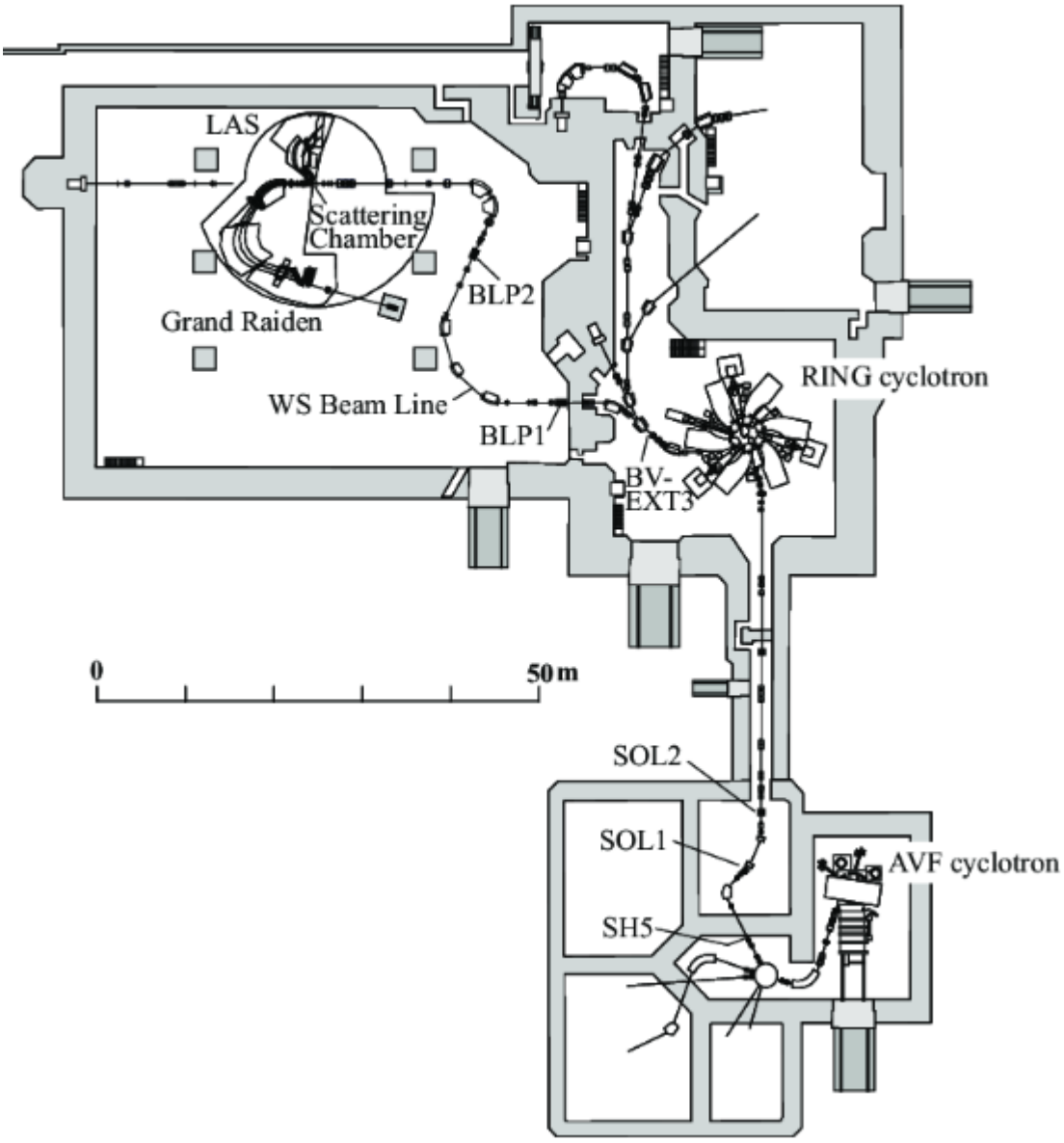

Figure 4.1 Schematic layout of the RCNP Ring Cyclotron facility.

4.2 Grand Raiden Spectrometer

The Grand Raiden Spectrometer (GRS) shown in Figure 4.2, is used to identify and analyze the momentum of tritons produced in (^{3}He,t) reactions [129]. The GRS was designed for high-resolution measurements. The GRS contains three dipoles magnets (D_1, D_2 and DSR), two quadrupoles (Q_1 and Q_2), one sextupole (SX), and one multipole (MP) magnet as shown in Figure 4.2. The multipole magnet can produce fields that are dipole, quadrupole, octupole, sextupole,

and decapole. It is used to correct for aberrations in the ion optics. The Dipole Magnet for Spin Rotation (DSR), is meant for polarized beam experiments and not used in this experiment. The GRS can achieve a momentum resolution of $\Delta p/p = 2.7 \times 10^{-5}$ and operate at magnetic rigidity of up to 5.4 Tm allowing the measurement of tritons at 140 MeV/u ($B\rho$ = 5.31 Tm) [130, 128]. Specification parameters of the GRS are shown in Table 4.1.

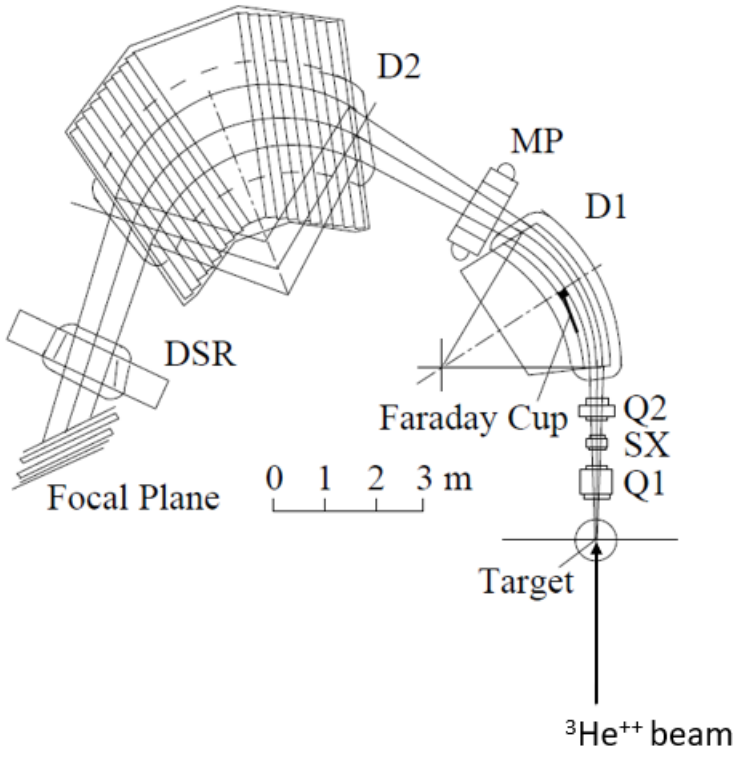

Figure 4.2 Schematic representation of the Grand Raiden Spectrometer set at 0°. The position and angle are measured in the focal plane detectors. The momentum vector of the ejectile is deduced, from which the excitation energy in the residual nucleus and scattering angles are determined. Figure modified from Ref. [131].

4.3 Focal-Plane Detectors for Grand Raiden Spectrometer

The Focal-plane (FP) detectors for the GRS contain two sets of Multi-Wire Drift Chambers (MWDCs, see Figure 4.3 and Table 4.2) placed in the focal plane of the spectrometer. They are used to collect information about the positions and angles of the particles. Each MWDC is filled with a gas mixture typically composed of argon (71.4%), and isobutane (28.6%). They have two anode-wire planes known as X and U anode-wire planes. The X layer has wires perpendicular to

Table 4.1 Specification parameters of Grand Raiden Spectrometer.

Parameters	Value
Intrinsic momentum resolution (ΔP/P)	2.7×10^{-5}
Intrinsic energy resolution (ΔE/E)	4.5×10^{-5}
Position resolution	300 μm (both horizontal and vertical)
Maximum Bρ	5.4 Tm
Maximum B (D_1, D_2)	1.8T
Maximum magnetic gradient (Q_1)	0.13 T/cm
Maximum magnetic gradient (Q_2)	0.033 T/cm
Momentum range	5%
Focal plane tilt	45%
Mean orbit radius	3 m
Total deflection angle	160°
Angular range	−5° to 90°
Horizontal magnification (x|x)	−0.417
Vertical magnification (y|y)	5.98
Maximum momentum dispersion	15.45 m
Horizontal acceptance angle	±20 mr
Vertical acceptance angle	±40 mr (in over-focus mode)
Solid angle	5.6 msr (3.2 in over-focus mode)
Weight	600 tons
Flight path for the central ray	20 m

the medium plane of the spectrometer, and the U layer has wires at an angle of 48.19° [129] with respect to the X plane. The potential wires are charged and serve to generate a uniform electrical field between the cathode and anode planes [131]. Charged particles ionize the gas atoms in the trajectory and the ionized electrons drift perpendicularly to the anode plane and are detected by the grounded sense wires. Drift times from the four sets of anode wires were measured and particle trajectories were determined with a position resolution of around 100 μm in each plane.

Event rates were such that the corrections for the lifetime of the data acquisition system (DAQ) were $\approx$ 95%.

The energy loss and time-of-flight information for each hit were measured by using a set of 10-mm thick plastic scintillators (PS1 and PS2), which are mounted behind the drift chambers. The first scintillator triggers the data acquisition system, serves as the start of the time-of-flight measurement, and benefits particle identification. The stop signal is provided by the cyclotron radio frequency (RF) signal. A 1-mm thick aluminum plate placed between the scintillators improves the particle identification (PID) by increasing the energy loss in the second scintillator. At the highest

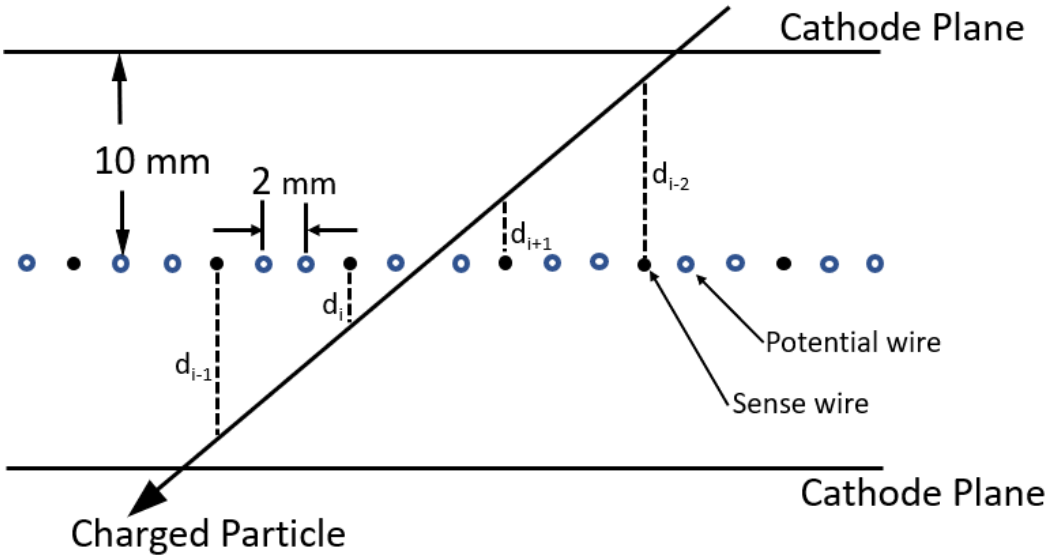

Figure 4.3 Schematic structure of an X-plane of the MWDCs for Grand Raiden Spectrometer. Anode wires and Cathode planes are represented with a typically charged particle track.

rigidity setting, beside the tritons, singly-charged $^3He^+$ ions enter the focal plane, as they have the same mass-to-charge ratio as the tritons. The $^3He^+$ ions are produced when the $^3He^{2+}$ beam particles pick up an electron in the reaction target. The particle-identification plot for this situation is shown in Figure 4.4. The gates used for selecting the $^3H^+$ and $^3He^+$ events are also indicated. The vertical bands associated with each species are due to pile-up. The $^3He^+$ particles produced via the atomic charge-exchange in target material [132] can be used for the calibration of scattering angles. Since the $^3He^+$ particles have the same rigidity as the tritons but have negligible scattering angles, they are useful for determining the central beam axis, corresponding to 0° scattering angle. The $^3He^+$ measurement is also helpful to obtain reliable energy calibration.

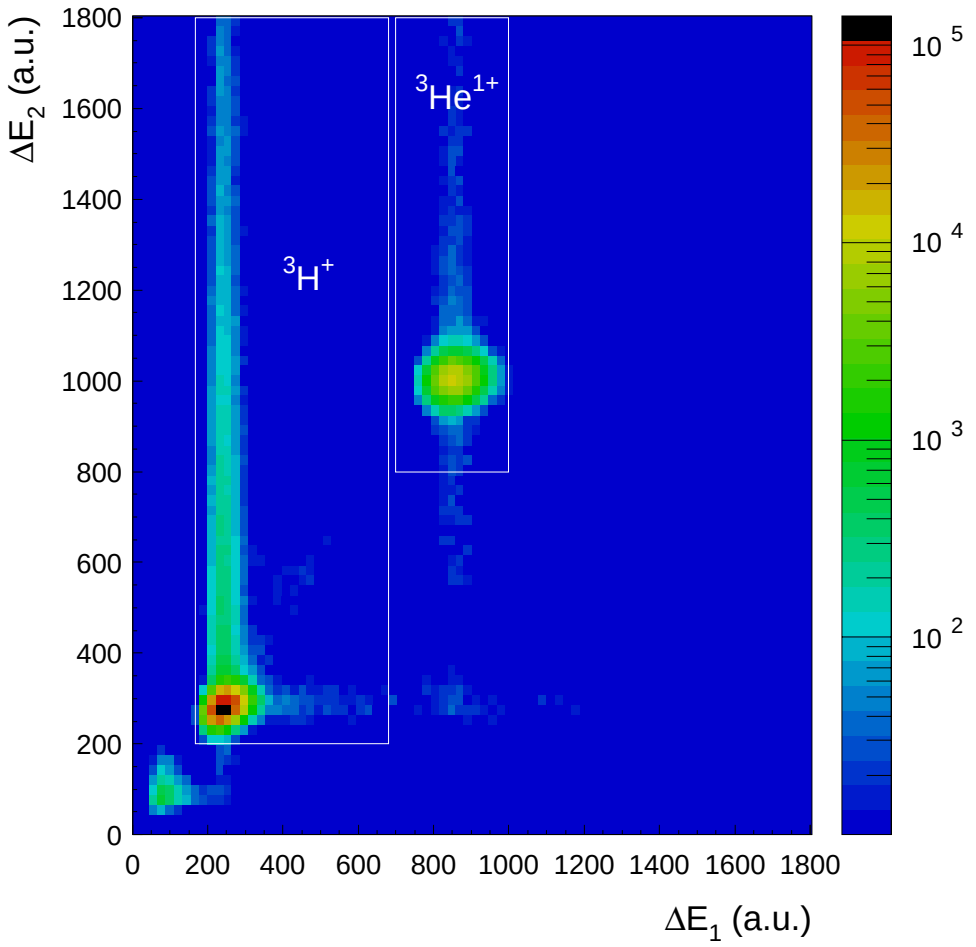

Figure 4.4 Particle identification from the plastic scintillator signals at Grand Raiden focal plane. Gates used to select tritons ($^3H^+$) and ^{3}He ($^3He^+$) charge-state particles are indicated. Particles near channel 0 in both axes are due to cosmic rays and noise in the scintillators.

The $^3He^{2+}$ beam transport to the GRS target location was achromatic. More details about the ion-optical modes for experiments at the GRS can be found in Ref. [126].

4.4 Missing-Mass Calculation

From the measured positions and angles in the MWDC detectors at the focal plane, the momentum vector of the triton is deduced, from which the excitation energies in the residual nucleus and scattering angle are determined from the missing-mass calculation [133]. The ray-trace matrix that is used to reconstruct the momenta and scattering angles from the positions and angles measured in the focal plane is determined empirically by using a sieve slit measurements [134]. The sieve slit is a block of a distinctive hole pattern (see Figure 4.5). It is installed 60 mm downstream from

Table 4.2 Specification parameters of the MWDC for Grand Raiden Spectrometer.

Parameters	Value
Anode:	
Wire configuration	X(0° = vertical), U(48.2°)
Sense wire	ϕ 20 μm gold-plated tungsten wire
Potential wires	ϕ 50 μm gold-plated beryllium-copper wire
Number of sense wires	192 (X) and 208 (U)
Anode wire spacing	2 mm
Sense wire spacing	6 mm (X) and 4 mm (U)
Cathode:	
Material	10 μm-thick carbon-aramid film
Supplied voltage	−5.6 keV
Cathode-anode gap	10 mm
Active area	1200^H mm × 120^W mm
Gas mixture:	Argon (71.4%) + Isobutane (28.6%) + Isopropyl alcohol (vapor pressure at 2°C)
Distance between two MWDCs	250 μm

the target and runs with this sieve slit are taken for every setting of the spectrometer for calibration purposes. To reconstruct horizontal and vertical scattering angles based on the hole pattern in the sieve slit, 6^{th} order polynomials relying on X_{FP}, Y_{FP}, $\Theta_{FP}^{horizontal}$ and $\Theta_{FP}^{vertical}$ are used. Then, the sieve slit is removed from the beam-line and the polynomials are used to reconstruct the target angles for the rest of the data. For the momentum calibrations, excitation energy spectra of nuclei with states for which the excitation energies are well known are used. For this experiment the ^{26}Mg(^{3}He,t) reaction was the primary calibration reaction.

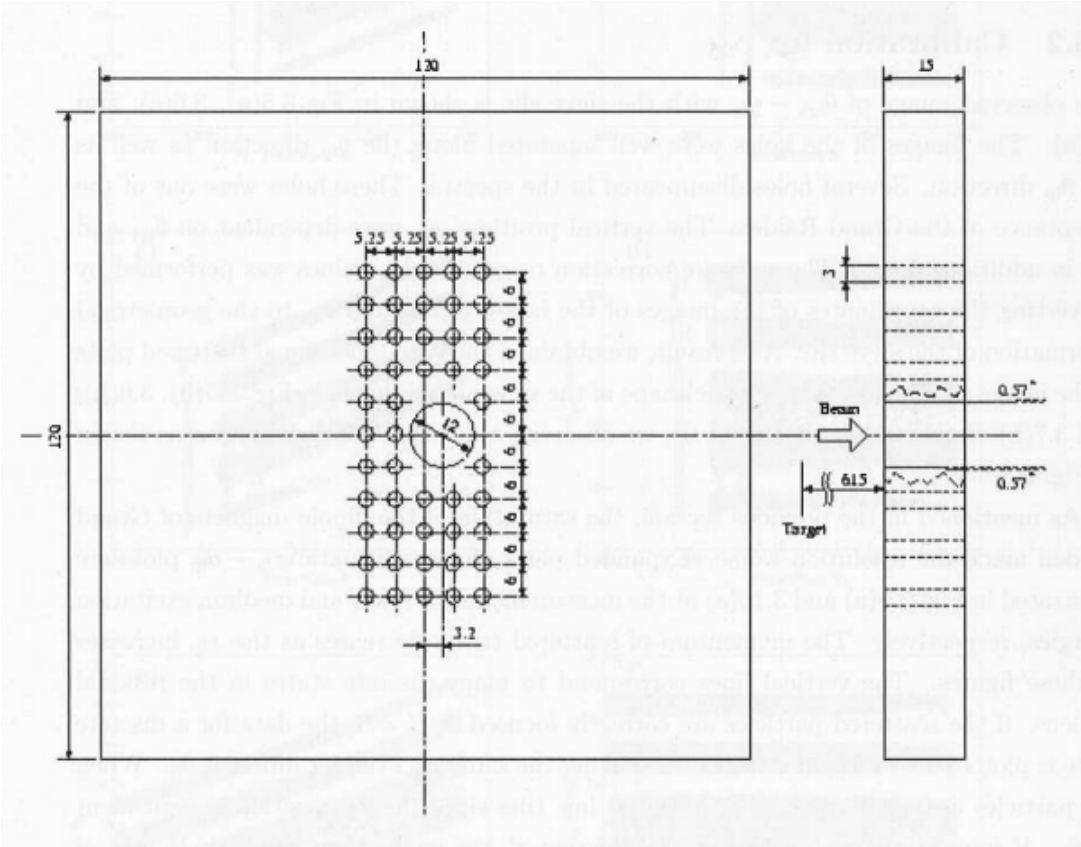

Figure 4.5 An example of the structure of sieve slit of the GRS for calibration of scattering angles. Figure taken from [135].

The missing-mass is calculated using the missing energy and momentum after reconstruction:

$$m_{miss} = \sqrt{E_{miss}^2 - P_{miss}^2} \tag{4.1}$$

The excitation energy is determined based on the mass of the residual nucleus;

$$E_x(^{60}\mathrm{Cu}) = m_{miss} - m(^{60}\mathrm{Cu}), \tag{4.2}$$

where m(^{60}Cu) is the ground-state mass of ^{60}Cu. The missing energy (E_{miss}) is defined as the excess energy in the ^{60}Ni(^{3}He,t) reaction:

$$\begin{aligned} E_{miss} &= E_i - E_f \\ &= E_k(^3\mathrm{He}) + m(^3\mathrm{He}) + m(^{60}\mathrm{Ni}) - E_k(^3\mathrm{H}) - m(^3\mathrm{H}) \end{aligned} \tag{4.3}$$

where E_k is the kinetic energy. $E_k(^3\mathrm{H})$ is determined from the reconstructed momentum of the triton.

$$E_k(^3\mathrm{H}) = \sqrt{p^2(^3\mathrm{H}) - m^2(^3\mathrm{H})} - m(^3\mathrm{H}) \tag{4.4}$$

The missing momentum is calculated from:

$$p_{miss} = \sqrt{p^2_{miss,x} + p^2_{miss,y} + p^2_{miss,z}} \tag{4.5}$$

where,

$$p_{miss,i} = p_i(^3\mathrm{He}) - p_i(^3\mathrm{H}) \tag{4.6}$$

In this calculation $p_x(^3\mathrm{He})$ and $p_y(^3\mathrm{He})$ are assumed to be 0. The x,y, and z components of the ^{3}H momentum are calculated from the measured momenta and scattering angle of the ^{3}H on the GRS:

$$\begin{cases} p_x(^3\mathrm{H}) = p_z(^3\mathrm{H}) \cdot tan(\Theta_x) \\ p_y(^3\mathrm{H}) = p_z(^3\mathrm{H}) \cdot tan(\Theta_y) \\ p_z(^3\mathrm{H}) = P_x(^3\mathrm{H}) \cdot cos(\Theta) \end{cases} \tag{4.7}$$

where,

$$\Theta = atan\left(\sqrt{tan^2(\Theta_x) + tan^2(\Theta_y)}\right) \tag{4.8}$$

and Θ_x and Θ_y are the reconstructed horizontal and vertical components of the scattering angle.

4.5 Magnetic Fields of Grand Raiden Spectrometer

As discussed in section 2.1, the strength distribution of the isovector-spin and non-spin-transfer giant monopole and dipole resonances are expected to extend up to high excitation energies. These features require experimental measurements with an energy range that covers the whole width of the resonances, approximately up to 60 MeV.

The momentum acceptance of the GRS is $\approx 5\%$. Therefore, the energy acceptance for a setting of the magnetic field is $\simeq 10\%$ (this is shown in Appendix E, since $\frac{dp}{p} \approx \frac{dk}{2k}$). This implies that the energy range for a 140 MeV/u (420 MeV) triton covered in a single setting is about 40 MeV. In order to cover the range of excitation energies above 40 MeV, three overlapping settings of the magnetic field were used. Examples of the measured spectra at these three settings are shown in Figure 4.6, for scattering angles between 25 and 30 mrad.

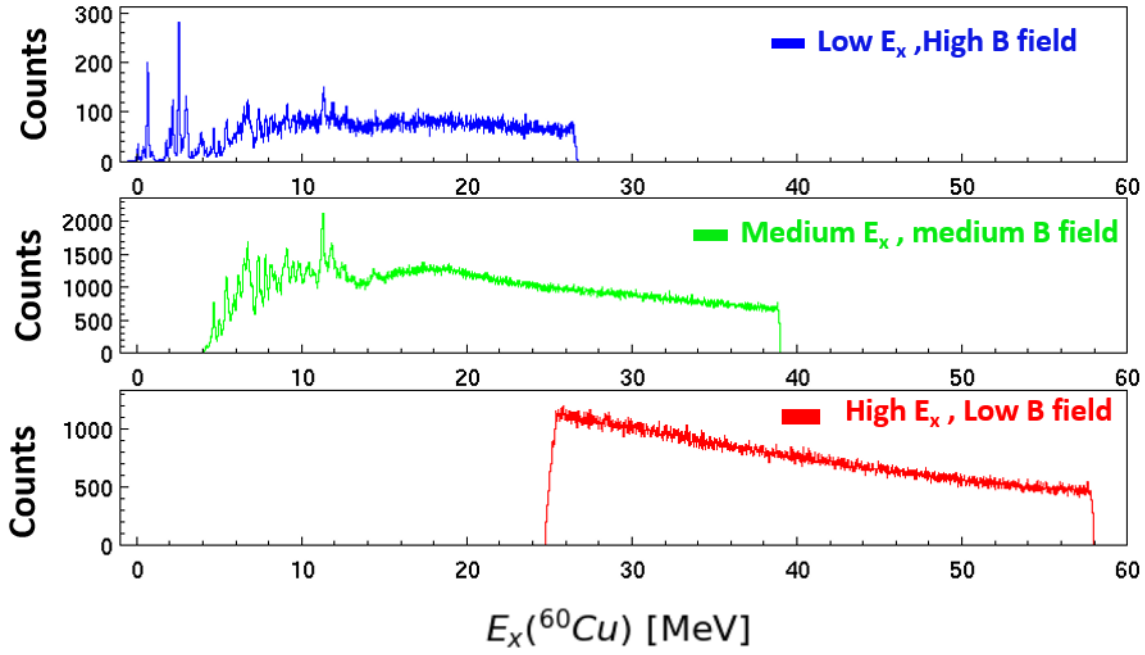

Figure 4.6 Singles spectra obtained for the ^{60}Ni(^{3}He,t) reaction for scattering angles between 25 and 30 mrad. Top: high magnetic field for the low excitation energy setting; Middle: medium magnetic field for the medium excitation energy setting; Bottom: low magnetic field for the high excitation energy setting.

4.6 Angular Acceptance and Resolution

The $^3He^+$ charge state provides a convenient way to determine the angular resolution. In Figure 4.7(a) and (b), the Θ_x and Θ_y distribution for the charge state are shown, respectively. The width (FWHM) of these distributions are 2.4 mrad (x) and 3.3 mrad (y), which constitute the angular resolutions in each direction.

The angular acceptance of the GRS has an irregular shape as shown in Figure 4.8, which displays Θ_x versus Θ_y for the low excitation energy runs. Near the edges of the acceptance, the angular acceptance is uncertain and depends on the momentum of the tritons. For $\Theta_h \leq -6$ mrad, the ray tracing of Θ_v is uncertain, especially at low triton momentum (high excitation energy), resulting in too many events at $\Theta \approx 0$. To ensure that only events with well-reconstructed angles are utilized and the acceptance is well understood, only the data with $-6 \leq \Theta_x \leq 21$ mrad and $-36 \leq \Theta_y \leq 36$ mrad were used, as indicated by the black box in Figure 4.8. Within the angular range defined by this box, 8 angular slices, each of 5 mrad wide, were used to create angular distributions as shown in Figure 4.9.

The solid angle of each of these 8 angular bins was determined in a simple Monte-Carlo integration. The result is shown in Figure 4.10. Due to the finite angular resolution, the effective solid angle of each angular bin is slightly distorted. The effect was included in the Monte-Carlo integration.

The estimated excitation energy resolution in ^{60}Cu via the ^{60}Ni(^{3}He,t) was 0.11 MeV, see Figure 4.11.

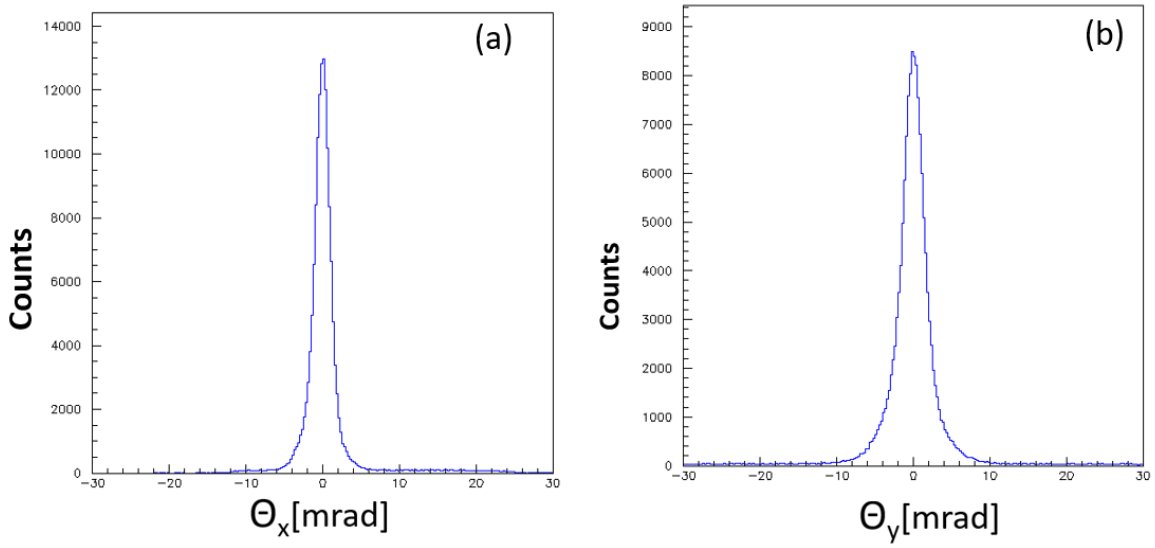

Figure 4.7 Figures(a) and (b) are the distribution of angular widths [FWHM] in horizontal (Θ_x = 2.4 mrad) and vertical (Θ_y = 3.3 mrad) projection, respectively. The angular resolution [FWHM] is $\sim$ 3 mrad.

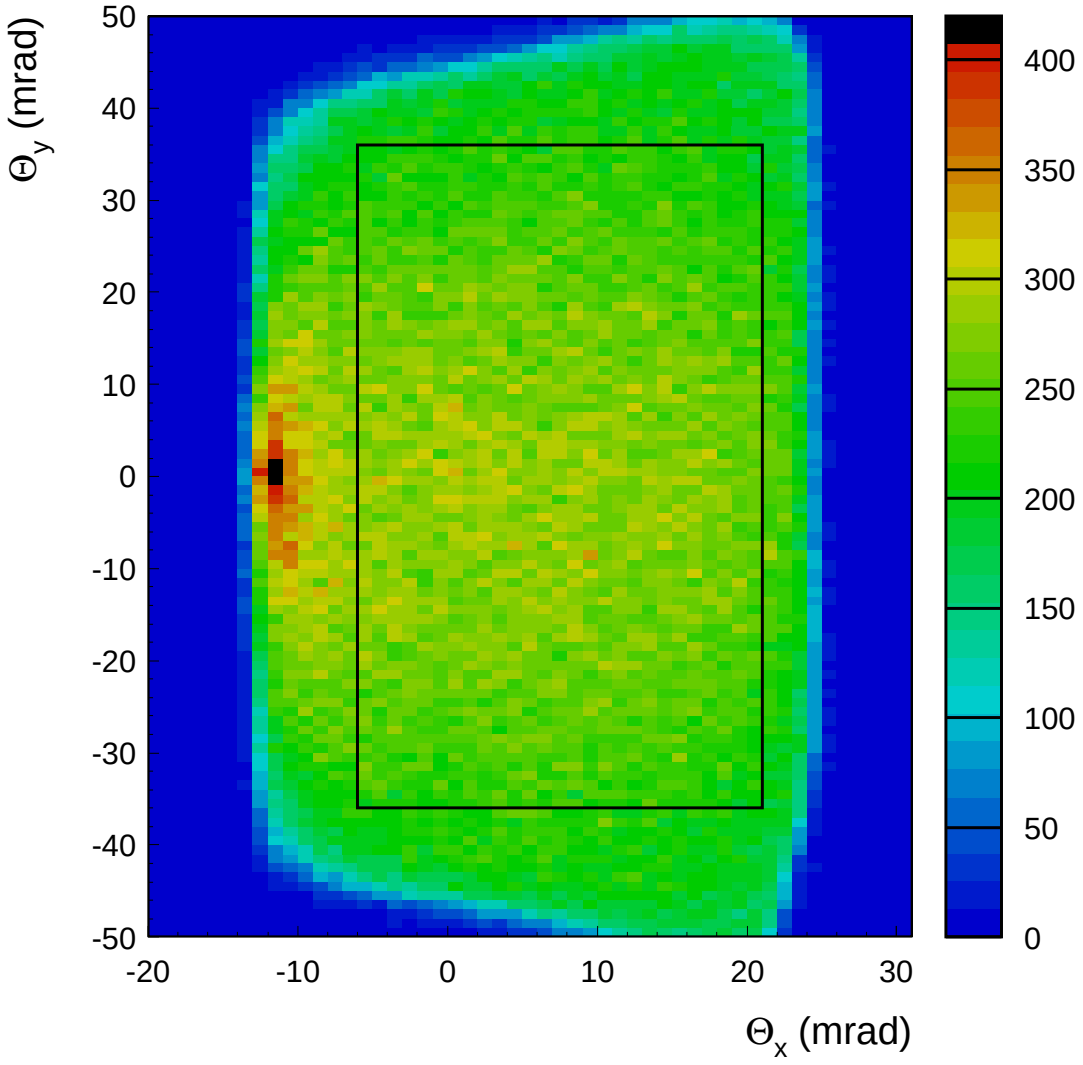

Figure 4.8 Reconstructed angles from the highest magnetic field setting. The black box indicates the angular ranges used in further analysis.

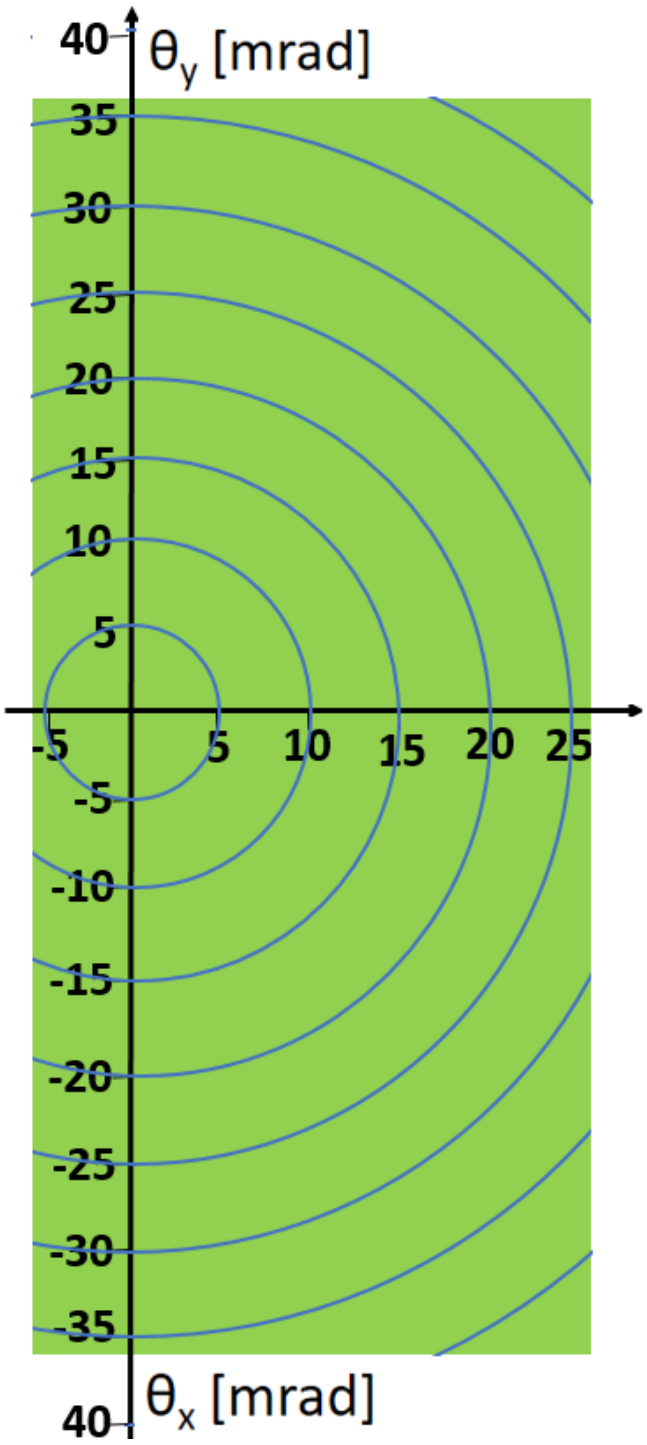

Figure 4.9 Figure illustrating vertical and horizontal angular acceptance of the GRS for the three angular settings used for ^{60}Ni(^{3}He,*t*) reaction. The 8 angular slices, each of 5 mrad wide are shown in circles.

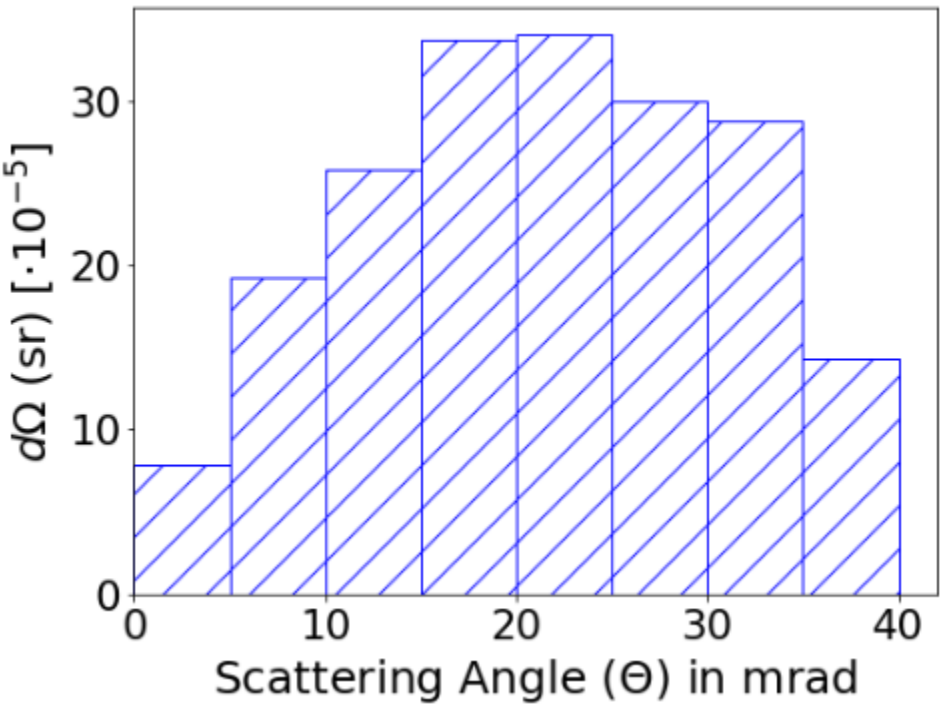

Figure 4.10 Calculated effective opening angles ($d\Omega$) for the angular bins used in the analysis of the ^{60}Ni(^{3}He,t) data.

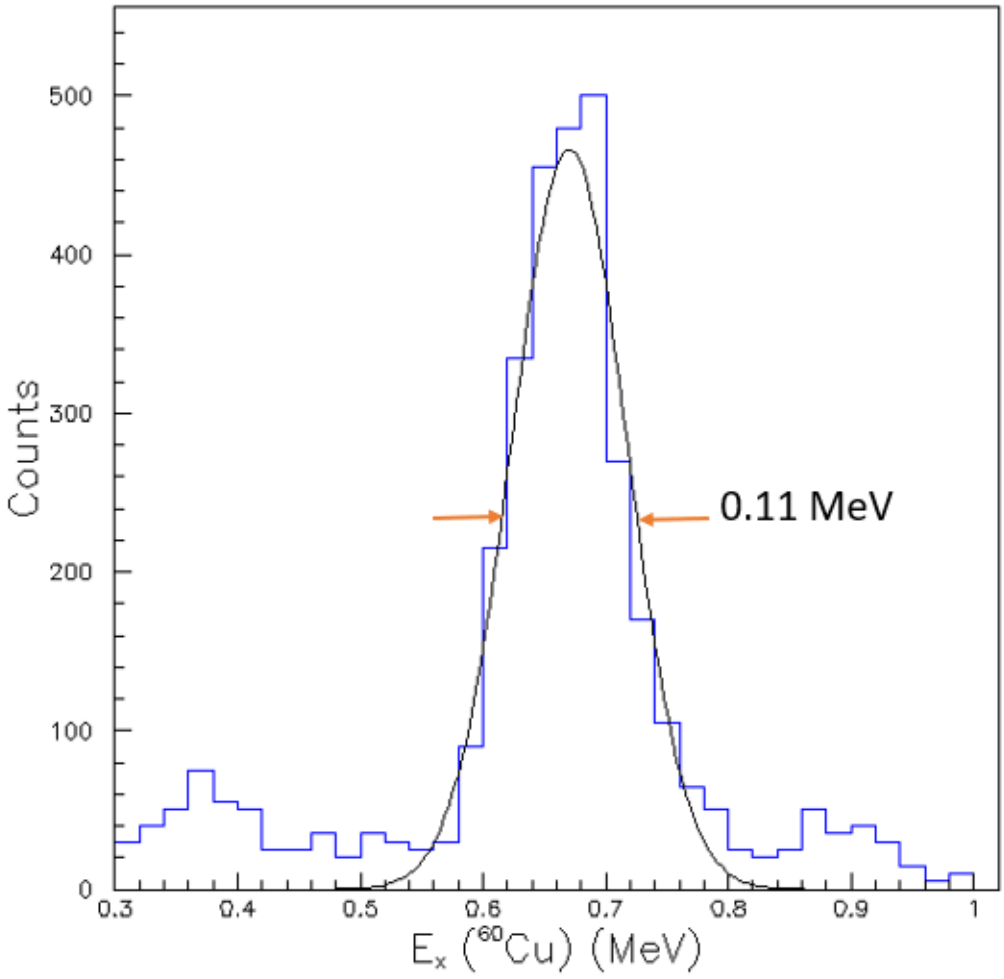

Figure 4.11 The estimated energy resolution [FWHM] from the analysis of the ^{60}Ni(^{3}He,*t*) data was 0.11 MeV.

4.7 Differential Cross Sections Calculation

As discussed in section 4.5, data from the three angular settings (low, medium, and high excitation energies) of the GRS were merged for every scattering angle bin of 5 mrad in order to have one spectrum from the full range of excitation energies up to 60 MeV. The differential cross-sections of the ^{60}Ni(^{3}He,t) reaction at 140 MeV were calculated using the following equation:

$$\frac{d\sigma}{d\Omega} = \frac{Y}{N_{beam} N_{tgt} \epsilon_1 \epsilon_2 d\Omega}, \tag{4.9}$$

where Y is the total number of counts in an angular bin, N_{beam} is the number of beam particles (^{3}He^{2+}) on target, N_{tgt} is the number of nuclei in the target ^{60}Ni foil of 2 mg/cm^2, ϵ_1 is the correction for the lifetime of the data acquisition system (95%), ϵ_2 is the correction for the target purity (98%), and $d\Omega = 2\pi \int_{\theta_i}^{\theta_f} \sin\theta d\theta$ is the solid angle for angular bin as shown in Figure 4.10, where θ_i and θ_f are the lower and upper angular bin limits.

Figure 4.12 and 4.13 shows results of the measured differential cross sections for different angular bins of 5 mrad from ^{60}Ni(^{3}He,t) data. The dominant observed peaks in the spectra are the GTR, please note that since the angular distributions of the IAS and GTR are similar and they both peak at forward angles. The IAS can be seen at an excitation energy of 2.55 MeV. The GTR peaks around 10 MeV. At higher excitation energies, the flat structure is a combination of states related to different angular momentum transfers. The statistical uncertainties are represented in the spectra.

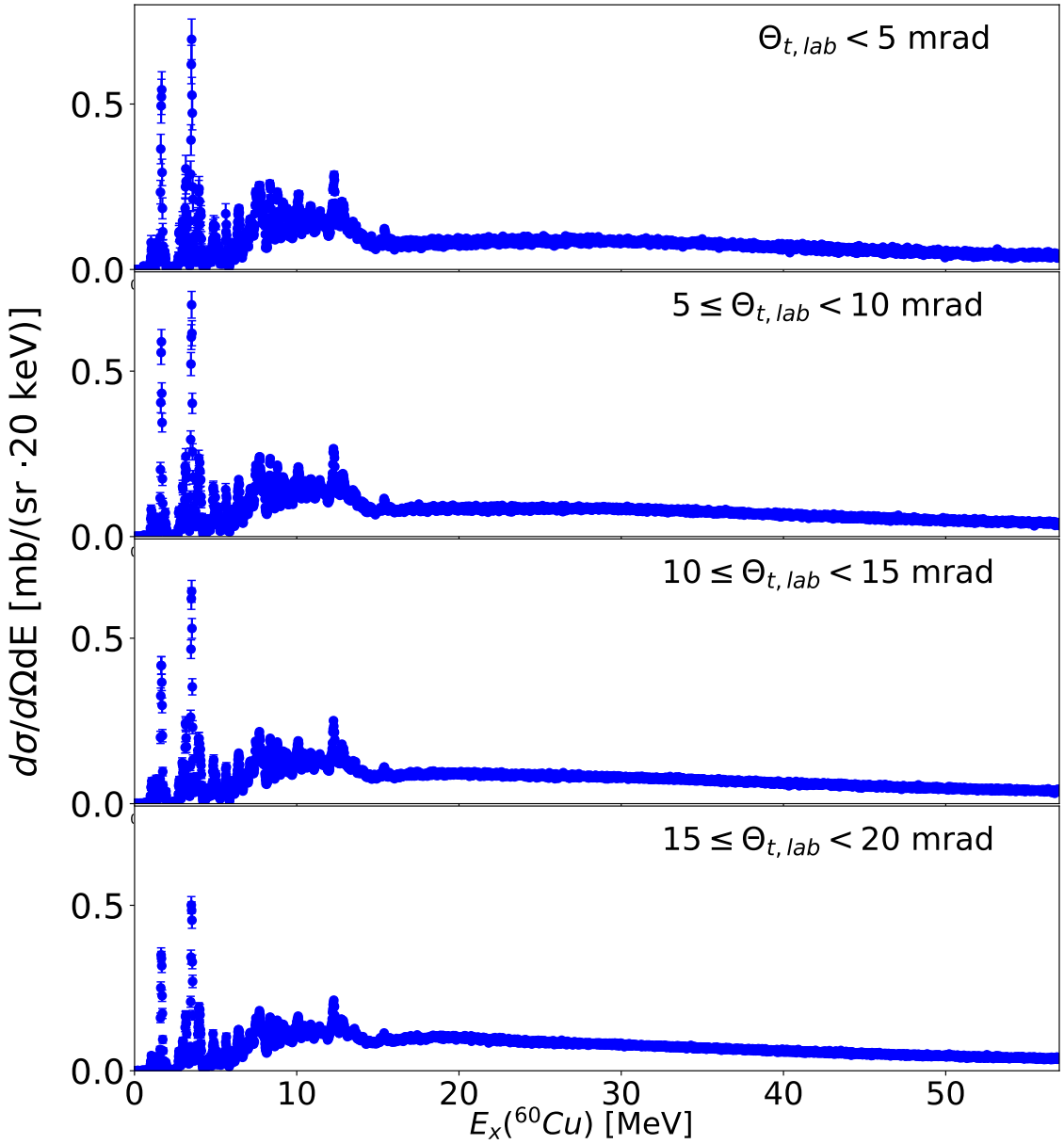

Figure 4.12 Extracted differential cross sections for each 5-mrad wide angular bin for the ^{60}Ni(^{3}He,t) reaction at 140 MeV/u. Angles are in the laboratory frame. The uncertainties presented in the data are statistical.

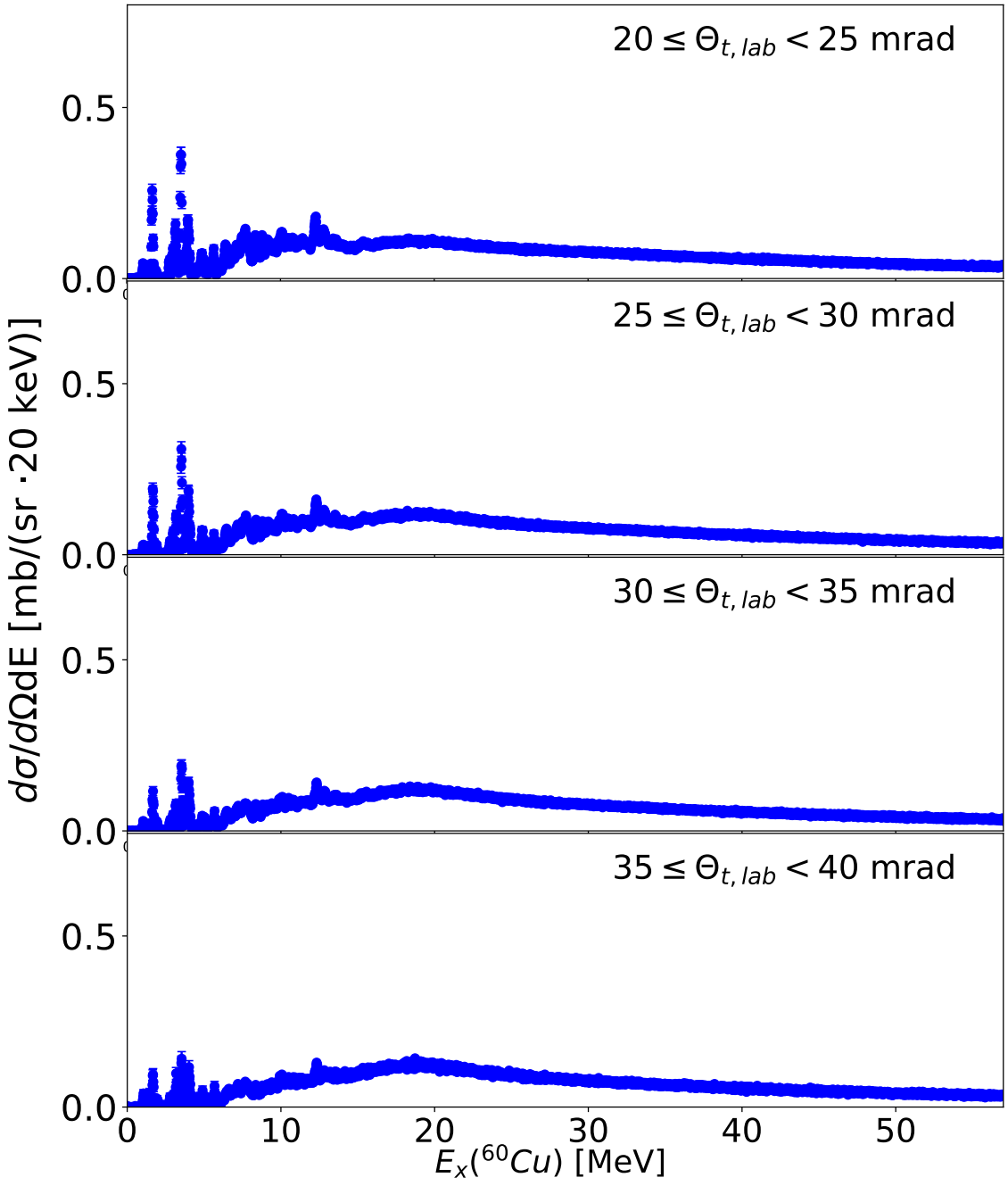

Figure 4.13 Extracted differential cross sections for each 5-mrad wide angular bin for the ^{60}Ni(^{3}He,t) reaction at 140 MeV/u. Angles are in the laboratory frame. The uncertainties presented in the data are statistical.

CHAPTER 5

RESULTS AND COMPARISON WITH THEORY

5.1 Calculated and Measured IAS

The next step in the analysis of the experimental data is to investigate the contribution from different types of transitions and to identify the location of the giant resonances. As discussed in Chapter 2, resonances associated with different units of angular momentum transfer peak at different scattering angles, and we can use a multipole decomposition analysis (MDA) to separate these contributions. In the following, we first look to the IAS, before performing a MDA of the whole excitation energy spectrum.

In ^{60}Cu, it is possible to identify individual states at low excitation energies. In Figure 5.1 (a) the excitation energy spectrum for $E_x < 5$ MeV is shown, at scattering angles of $\Theta_{t,lab} < 5$ mrad. Figure 5.1 (b) shows the differential cross section for the transition to the IAS of the ^{60}Ni: ground state, located at an excitation energy of 2.55 MeV as indicated in Figure 5.1 (a). The error bars show statistical errors. The measured differential cross section is compared with the theory, based on the distorted wave Born approximation (DWBA) see section 3.4.3. The theoretical cross section was higher than the measured cross-section and scaled down by a factor of 1.35 to match the measured cross sections. The likely reason for this overestimation by the theory is the use of an approximation to the exchange contribution in the NN interaction used in the calculation [37]. Other than this scaling factor, the theoretical calculation matches well with the experimental data, indicating the ability of the DWBA calculation to accurately describe the experimental angular distributions.

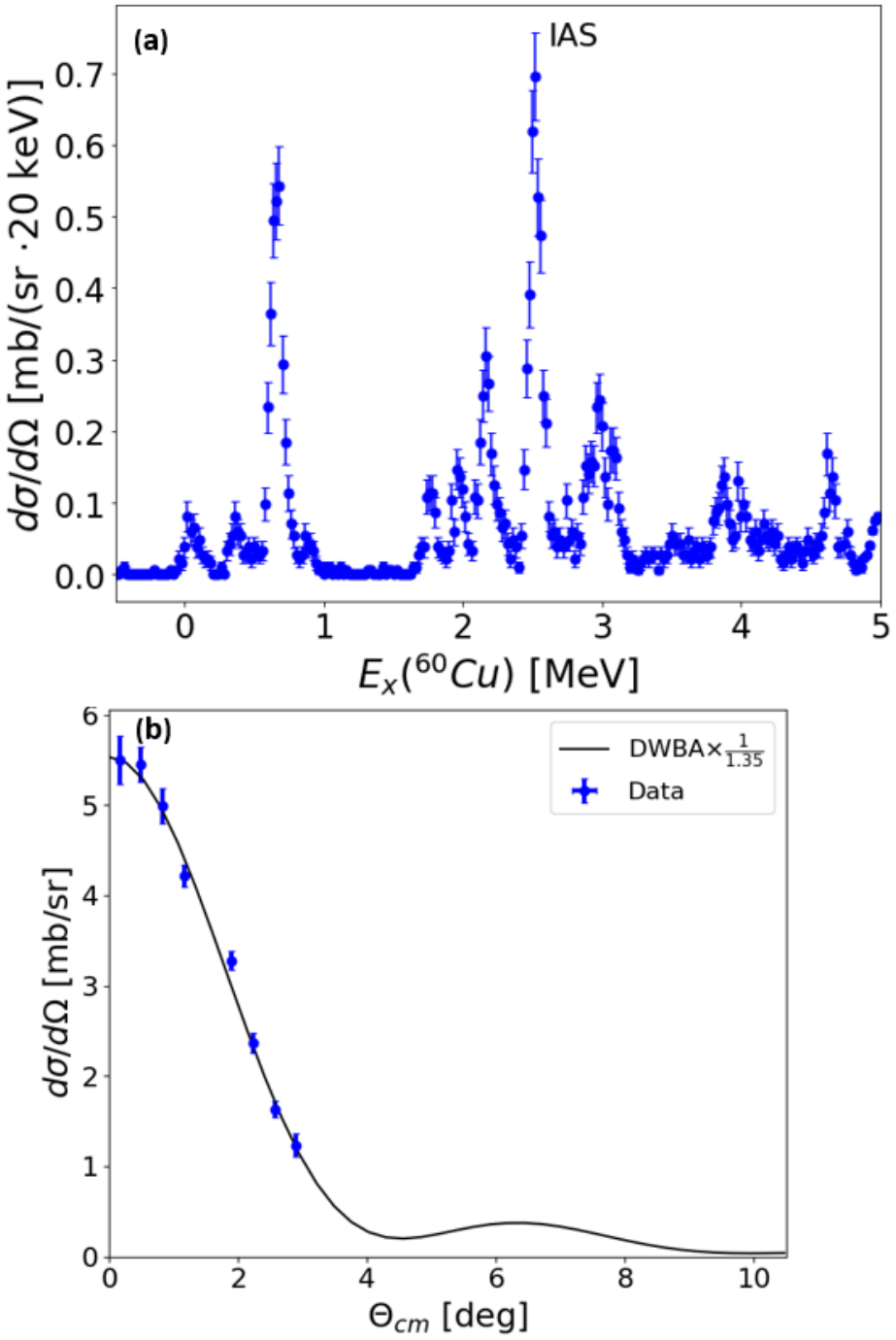

Figure 5.1 Figure (a) shows the excitation-energy spectrum between 0 and 5 MeV for the ^{60}Ni(^{3}He,t) reaction at 140 MeV/u. Figure (b) shows the comparison of the measured differential cross section for the IAS with theory, based on the DWBA calculation as shown with the black solid line. The DWBA calculation was scared down by a factor of 1.35.

5.2 Multiple Decomposition Analysis Results

As discussed in chapter 3, the MDA is a method used to extract contributions to the measured spectra that are associated with the transfer of different units of angular momentum (ΔL). The MDA was performed by fitting the measured differential cross section shown in Figures 4.12 and 4.13 for each energy bin with a linear combination of theoretical angular distributions (see Eq. 3.2), each associated with a different value of ΔL, as discussed in section 3.4.3.

Figures 5.2 and 5.3 illustrates the MDA fits for a few selected excitation energy bins. A bin size of 40 keV was used in order to ensure adequate statistics for the MDA. In DWBA, the ΔL=0, 1, and 2 shapes were computed with matching excitation energy for each bin. Note that systematic uncertainties related to the choice in which monopole, dipole, or quadrupole formfactor is used, is relatively small as the angular distributions for different choices are very similar.

The top four figures in Figure 5.2 depict a fit at excitation energies below 14 MeV, where the monopole ($\Delta L = 0$) contribution dominates over other ΔL values. However, as the scattering angles increase, the dipole ($\Delta L = 1$) contribution becomes significant. The bottom two panels in Figure 5.2 show fits around 20 MeV, where $\Delta L = 1$ and 2 contributions are relatively strong. Below 1°, the $\Delta L = 2$ component dominates, while above 1°, the dipole contributions dominate.

Figure 5.3 (top two figures) shows fits around 30 MeV, where all ΔL values contribute to the total strength. Below 1.25°, the monopole contribution dominates, while above 1.25°, the dipole contribution dominates. For the fit around 47 and 48 MeV in Figure 5.3 (middle two figures), the $\Delta L = 2$ component dominates at all scattering angles, but other $\Delta L = 0$ and 1 values also contribute to the total strength. Finally, the bottom two panels of Figure 5.3 show the fit around 54 and 57 MeV, where all ΔL values contribute to the total strength. Below 1.25°, a significant contribution of the $\Delta L = 0$ component was observed, while above 1.25°, the $\Delta L = 1$ component dominates.

Please note that the components $\Delta L = 2$ likely also include contributions from excitations with higher ΔL, but given the relatively narrow angular range covered in the experiment, these cannot be separated.

The results from the MDA for each individual bin can now be combined to obtain a picture of

the multipole response as a function of excitation energy. The combined plots are shown in Figure 5.4 and 5.5 for each of the angular bins. Figure 5.4 shows the results for angular bins below 20 mrad. Each figure contains the contributions from each ΔL component, the sum of these three components, and the experimental data.

The $\Delta L = 0$ contributions are enhanced at low scattering angles and below $E_x = 12$ MeV it is the dominant contribution to the spectrum. This strength can be attributed to Gamow-Teller transitions, aside from the IAS at 2.55 MeV. Note that the $0^+ \rightarrow 1^+$ GT transitions have a $\Delta L = 0$ and $\Delta L = 2$ component. Therefore, in regions where GT transitions are strong, a $\Delta L = 2$ contribution must be present as well. Of course, $\Delta L = 2$ contributions can also come from transitions to 2^+ and 3^+ final states as well. At higher excitation energies, contributions to the $\Delta L = 0$ response from the IVGMR and IVSGMR are expected. Indeed, $\Delta L = 0$ strength is observed above 20 MeV, but the interpretation is complicated by contributions from quasifree reactions, as discussed below.

Dipole strength (with $\Delta L = 1$) peaks at a larger scattering angle. Indeed a broad resonance that peaks at about 19 MeV is visible at the largest scattering angles. This broad structure is due to a combination of the IVSGDR ($J^\pi = 0^-, 1^-, 2^-$) and IVGDR $J^\pi = 1^-$. Because the extracted $\Delta L = 2$ distribution also contains contributions from transitions with $\Delta L > 2$, the interpretation of this distribution is ambiguous. It doesn't display a clear resonance like structure even though the IVGQR and IVSGQR should contribute to the spectrum at high excitation energies. This is due to the fact that the quasifree reactions contribute significantly to the $\Delta L = 2$ response, as discussed below. In the next sections, the responses will be examined in more detail.

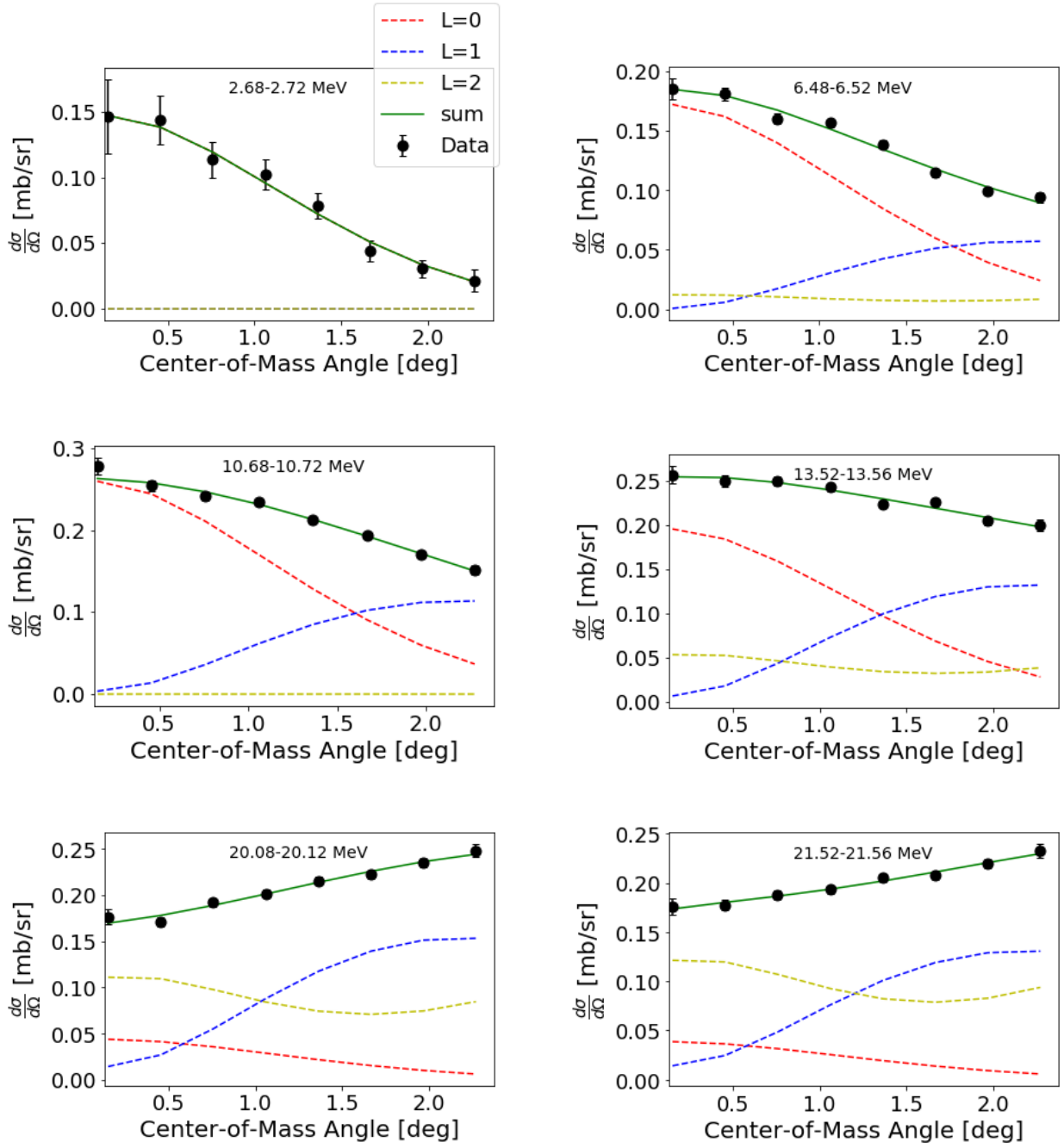

Figure 5.2 Figures show the MDA fit for a few selected measured center-of-mass angular distributions in 0.04 MeV bins between 0 and 60 MeV in ^{60}Cu. The experimental data are represented by black dots, while the dashed red, blue, and yellow lines correspond to the ΔL=0,1,2 components respectively of each fit determined from the MDA. The green solid line is the sum of the three MDA fit components. For more details, see the text.

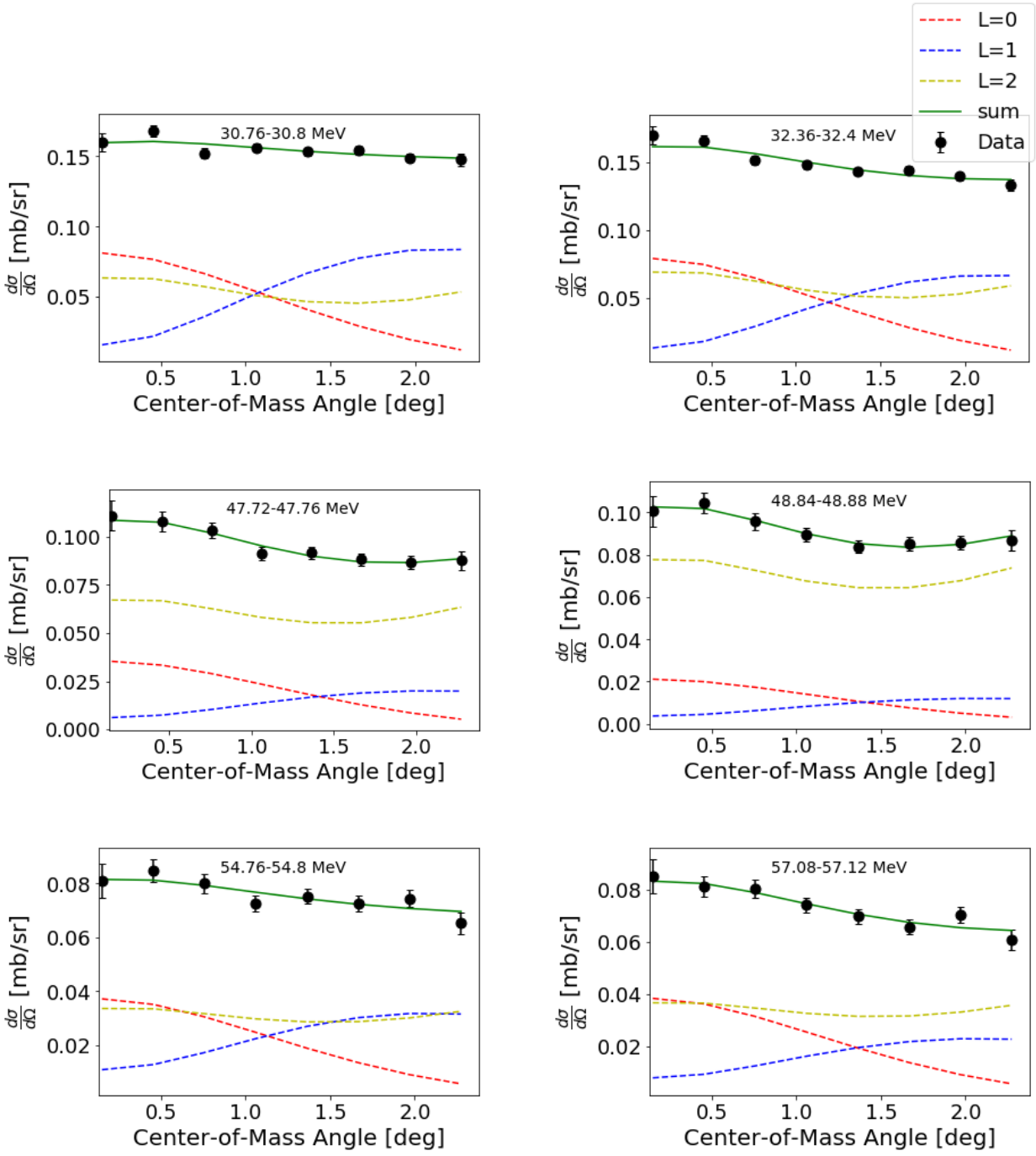

Figure 5.3 *Cont* Figures show the MDA fit for a few selected measured center-of-mass angular distributions in 0.04 MeV bins between 0 and 60 MeV in ^{60}Cu. The experimental data are represented by black dots, while the dashed red, blue, and yellow lines correspond to the ΔL=0,1,2 components respectively of each fit determined from the MDA. The green solid line is the sum of the three MDA fit components. For more details, see the text.

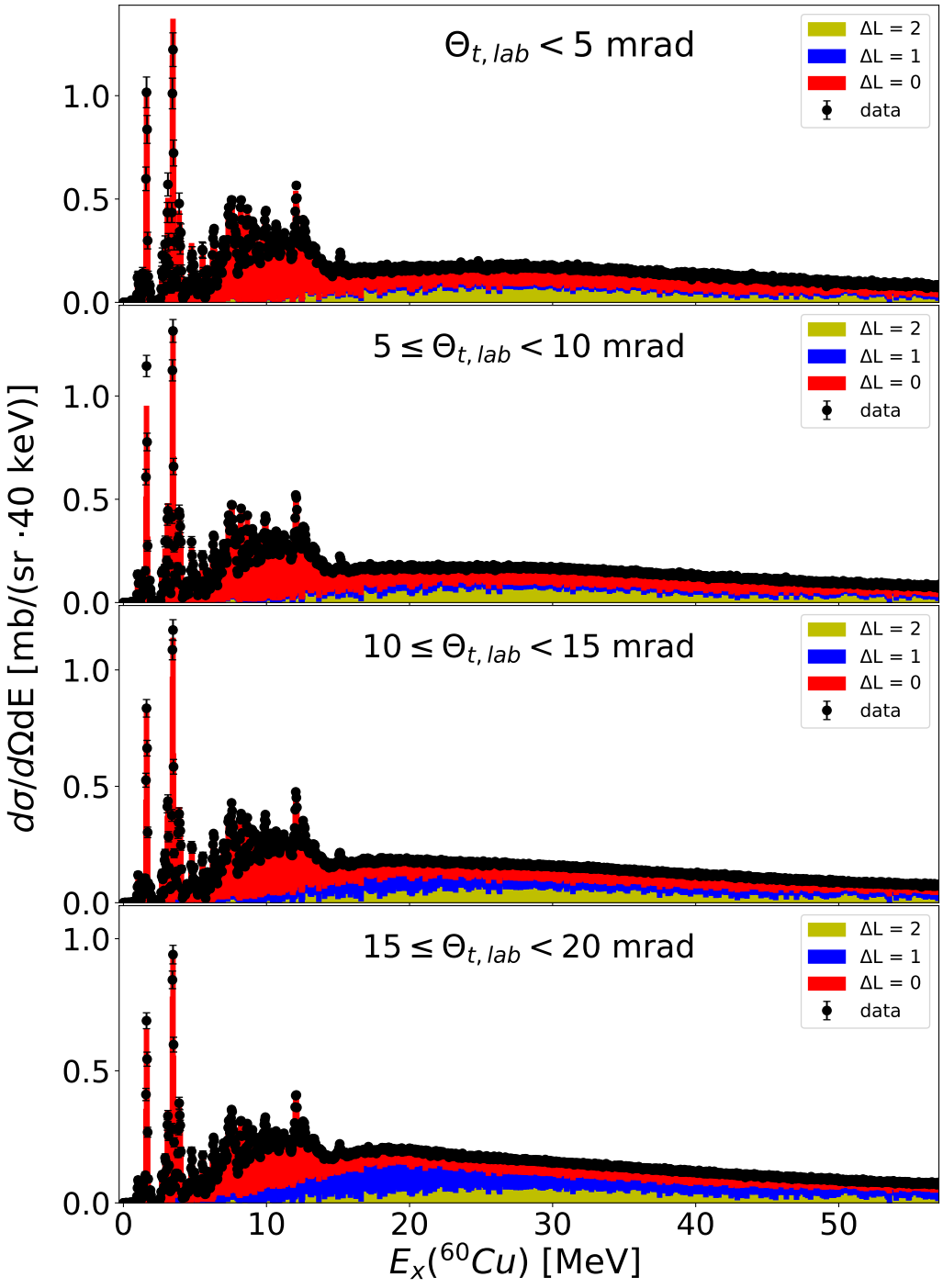

Figure 5.4 MDA results presented as the differential cross sections of ^{60}Ni(^{3}He,t) reaction at 140 MeV/u for scattering angle bin from 0 up to 20 mrad angular distribution. Each 0.04 MeV energy bin's associated angular distribution was fit in the MDA with ΔL =0, 1 and 2 theoretical angular distribution.

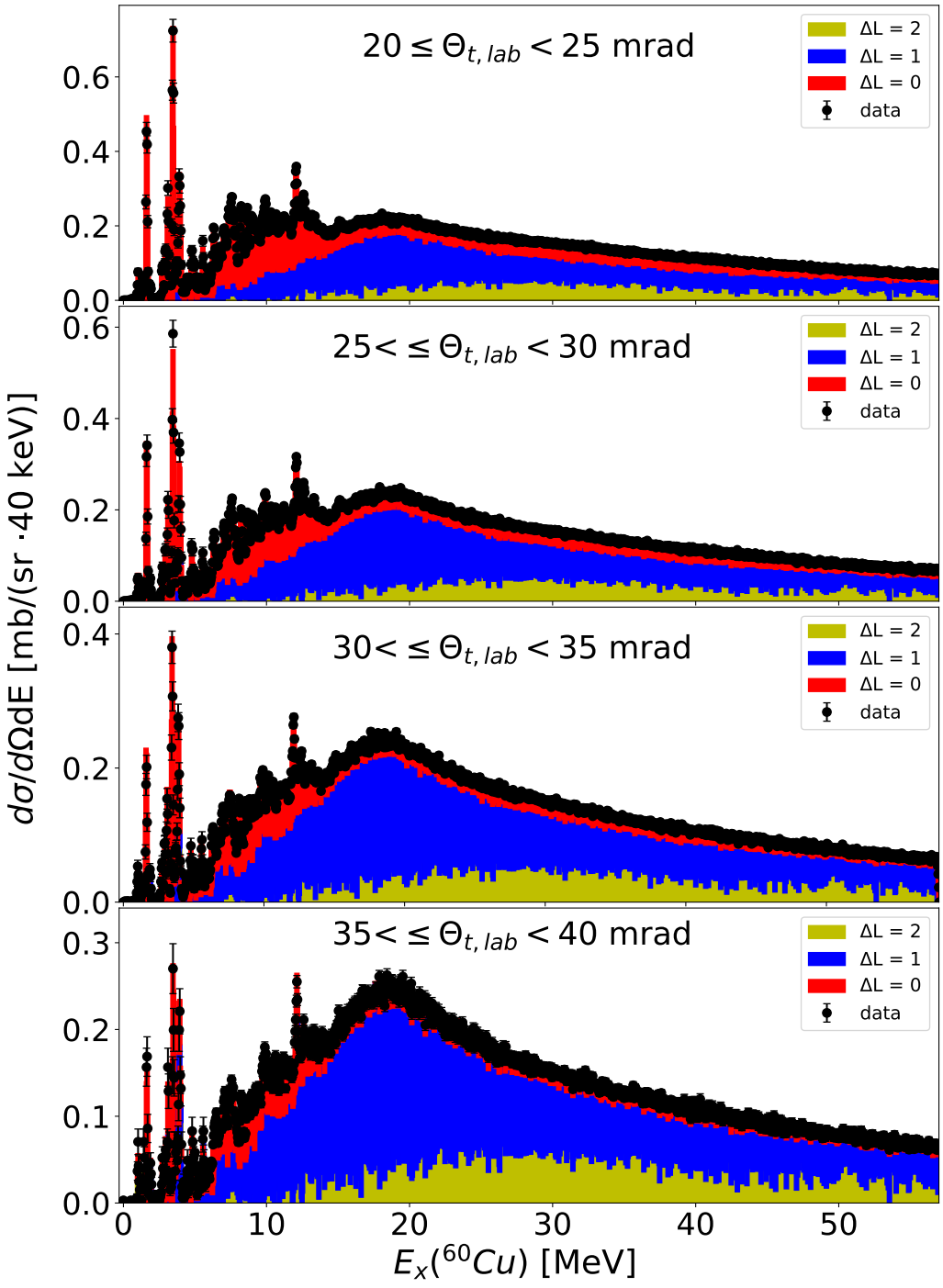

Figure 5.5 MDA results presented as the differential cross sections of ^{60}Ni(^{3}He,t) reaction at 140 MeV/u for scattering angle bin from 25 up to 40 mrad angular distribution. Each 0.04 MeV energy bin's associated angular distribution was fit in the MDA with ΔL =0, 1 and 2 theoretical angular distribution.

5.3 Gamow-Teller Strength B(GT) Extraction

5.3.1 Extrapolation to q=0

Section 3.5 introduced a relationship between charge-exchange cross sections extracted to zero momentum transfer and Gamow-Teller strength, B(GT), as shown in Eq. 3.16. The top four figures in Figure 5.2 and Figure 5.4 indicate that the cross-section at forward angles is dominated by $\Delta L = 0$ transitions, which enables the extraction of B(GT) as a function of excitation energy. Firstly, the cross section needs to be extrapolated to zero linear momentum transfer ($q \rightarrow 0$). For this purpose the cross section at 0° for the $\Delta L = 0$ component from the MDA was extracted from finite physical Q value to $Q = 0$, using the DWBA calculations:

$$\left.\frac{\mathrm{d}\sigma}{\mathrm{d}\Omega}(\mathrm{q}=0)\right|_{\Delta\mathrm{L}=0} = \left[\frac{\frac{\mathrm{d}\sigma}{\mathrm{d}\Omega}(\mathrm{Q}=0,\theta=0^\circ)}{\frac{\mathrm{d}\sigma}{\mathrm{d}\Omega}(\mathrm{Q}=\mathrm{Q},\theta=0^\circ)}\right]_{\mathrm{DWBA}} \times \left[\frac{\mathrm{d}\sigma}{\mathrm{d}\Omega}(\theta=0^\circ,\mathrm{Q})\right]^{\Delta\mathrm{L}=0}_{\mathrm{experiment}} \tag{5.1}$$

The DWBA scaling factor is displayed in Figure 5.6. Finally, after extracting the experimental cross section at $q = 0$ and by using the Gamow-Teller unit cross section ($\hat{\sigma}_{GT} = 7.614$, see Figure 3.9): the B(GT) was calculated by dividing the differential cross section at $q = 0$ by the unit cross section.

$$\mathrm{B(GT)} = \frac{\left.\frac{\mathrm{d}\sigma}{\mathrm{d}\Omega}(\mathrm{q}=0)\right|_{\Delta\mathrm{L}=0}}{\hat{\sigma}_{\mathrm{GT}}} \tag{5.2}$$

A 10% uncertainty that scales all GT strengths attributed to the uncertainty in $\hat{\sigma}_{GT}$ was taken into consideration in the further analysis [136, 19, 48]. Figure 5.7(a) presents the B(GT) distribution extracted as a function of excitation energy, while Figure 5.7(b) shows the cumulative B(GT) strength up to 20 MeV. In the subsequent section, the comparison with the shell-model calculation for the same excitation energy range is discussed.

For excitation energies up to 20 MeV, the MDA analysis yielded a total GT strength of 10.6 ± 1.45 (stat) ± 1.19 (sys). At higher excitation energy additional strength is found that is associated with $\Delta L = 0$ and likely contains some additional GT strength. However, at high excitation energies contributions from the isovector giant monopole resonances are expected to dominate the $\Delta L = 0$ response.

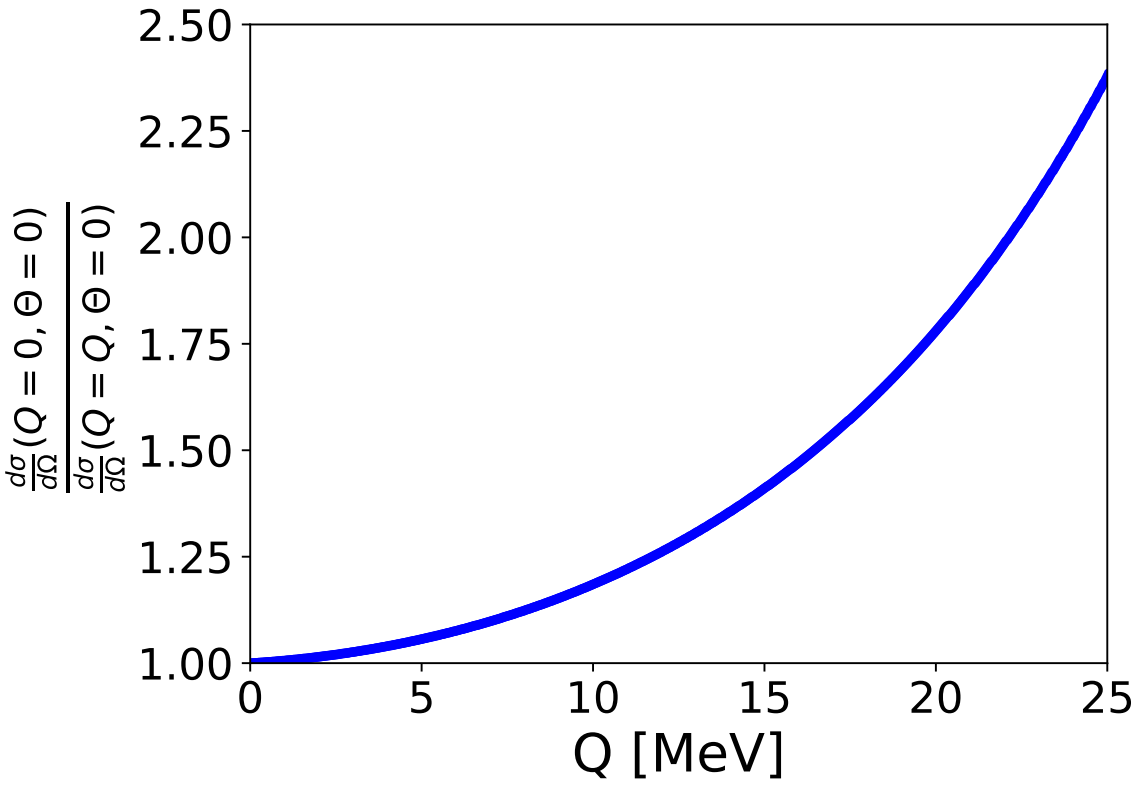

Figure 5.6 The ratio of the differential cross sections at $\theta = 0°$ and at zero Q-value ($Q = 0$) to that of $\theta = 0$ and $Q = Q_{exp}$ as calculated in DWBA.

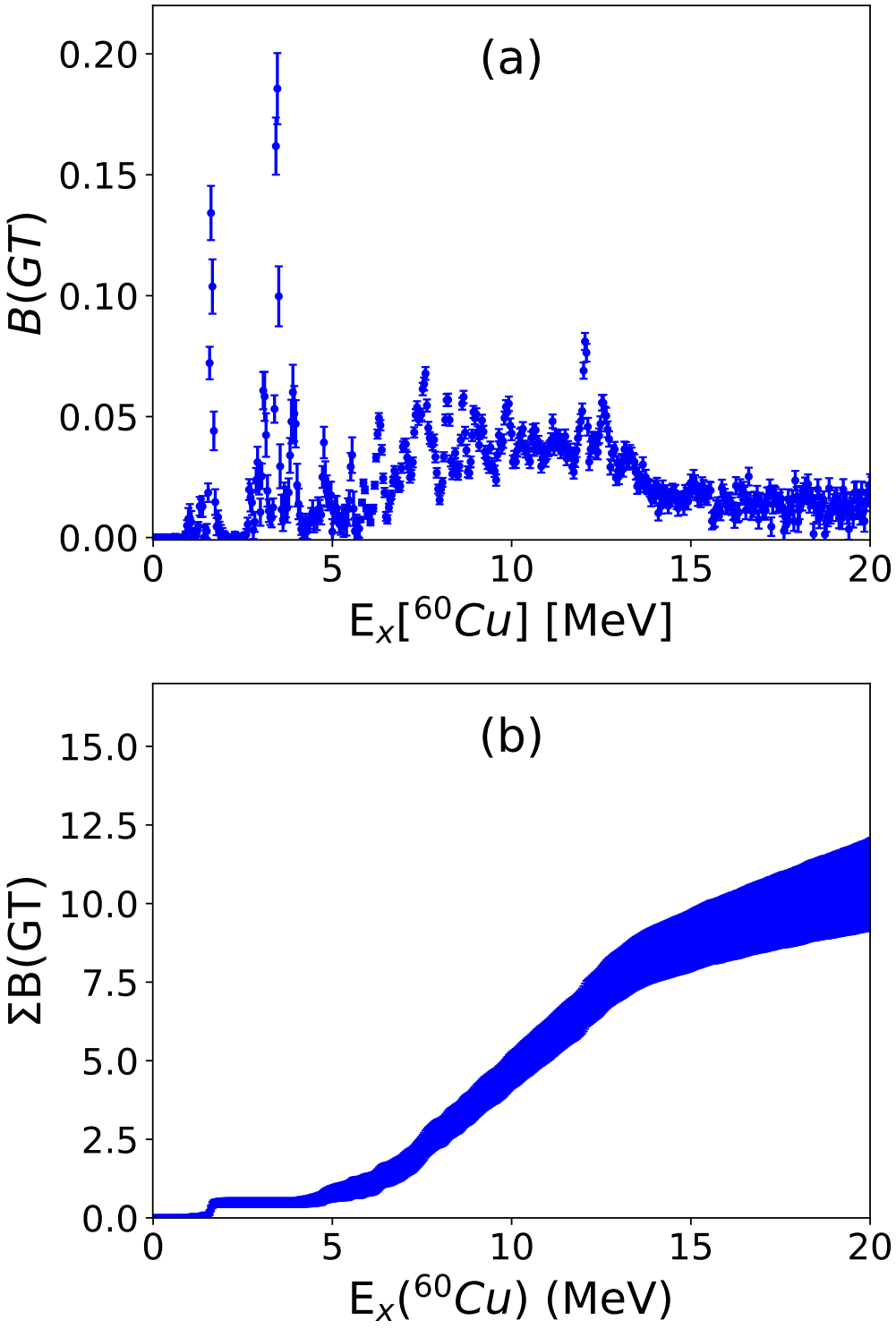

Figure 5.7 Figure (a) shows the extracted B(GT) in ^{60}Cu up to 20 MeV excitation energy, while Figure (b) displays the cumulative B(GT) strengths after removing IAS. The uncertainties shown are statistical. An additional uncertainty of 10% that scales all GT strengths is due to the uncertainty in $\hat{\sigma}$ [136, 19, 48].

5.3.2 Comparison with Theory, Shell-Model Calculations

The B(GT) distributions as a function of the excitation energy extracted from ^{60}Ni(^{3}He,t) reaction were compared to the strengths distributions calculated in shell-model calculations performed in pf-shell-model space using the GXPF1A interaction [137]. Truncations in the shell-model space were necessary to calculate the strength up to high excitation energy. The calculations were performed with the code NushellX [117]. Three calculations were performed, one in which the pf-shell-model space was not truncated, one in which at least 7 neutrons and protons were in $f_{7/2}$ orbit (strong truncation), and one in which at least 6 neutrons and protons were in the $f_{7/2}$ orbit (mild truncation). Calculations with no truncation could be performed up to an excitation energy of 6.5 MeV. Calculations with a mild truncation could be performed up to $\sim$ 15 MeV. Calculations with a strong truncation were performed up to 20 MeV. All shell-model calculations were scaled by a factor of 0.56 (see section 2.3.2) to account for a well-known quenching of the GT strength [138].

The comparisons of the experimental and theoretical GT strengths are shown in Figure 5.8 and 5.9. The theoretical strength distributions shown in Figure 5.8 match the overall structure of the experimental spectra quite well. There are several relatively strength transitions at low excitation energies and a broad distribution of strength between 5 and 15 MeV. On the other hand, it is not possible to make a one-to-one correspondence between experimental and theoretical transitions even at low excitation energies, and reducing the truncation does not provide a significantly better result, even though the theoretical spectra change significantly with different levels of truncation. Above 17 MeV more strength is found than in theory. Some of this strength might be attributed to the quenched strength at low excitation energy. However, some of this strength could also be due to the excitation of the isovector giant monopole resonances and to the quasifree-continuum as discussed in later sections.

To compare the total strength, the cumulative strengths are plotted in Figure 5.9. The level of truncation modifies the summed strength, and the total strength is lower with reduced truncation. Slightly more strength is found in the experiment compared to the theoretical calculations. The shell-model calculations plateau above 15 MeV, whereas some GT strength is observed. As

discussed above, this could be due to quenched strength at low excitation energies shifting to higher excitation energies or due to misinterpreted isovector monopole strength or contributions from the quasifree-continuum.

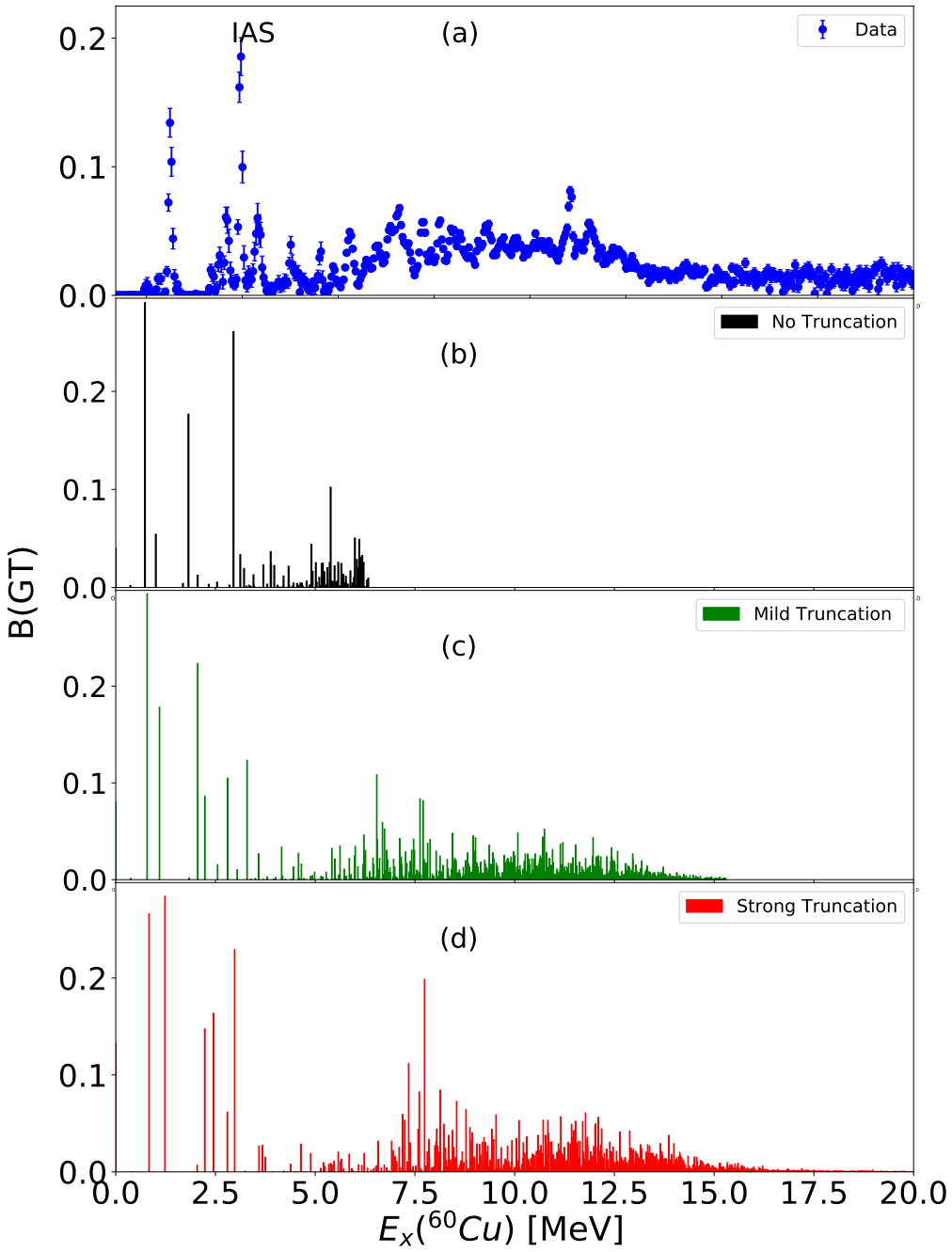

Figure 5.8 The comparison of the measured B(GT) strength and these from shell-model calculations. Figure (a) shows the measured B(GT) strengths up to 20 MeV. Figure (b) to Figure (d) shows theoretical shell-model calculations in black, green, and red for no truncation, mild truncation, and strong truncation, respectively. Note that the IAS is visible in the extracted strengths from the experiment, but does not appear in the theoretical calculations (Gamow-Teller only).

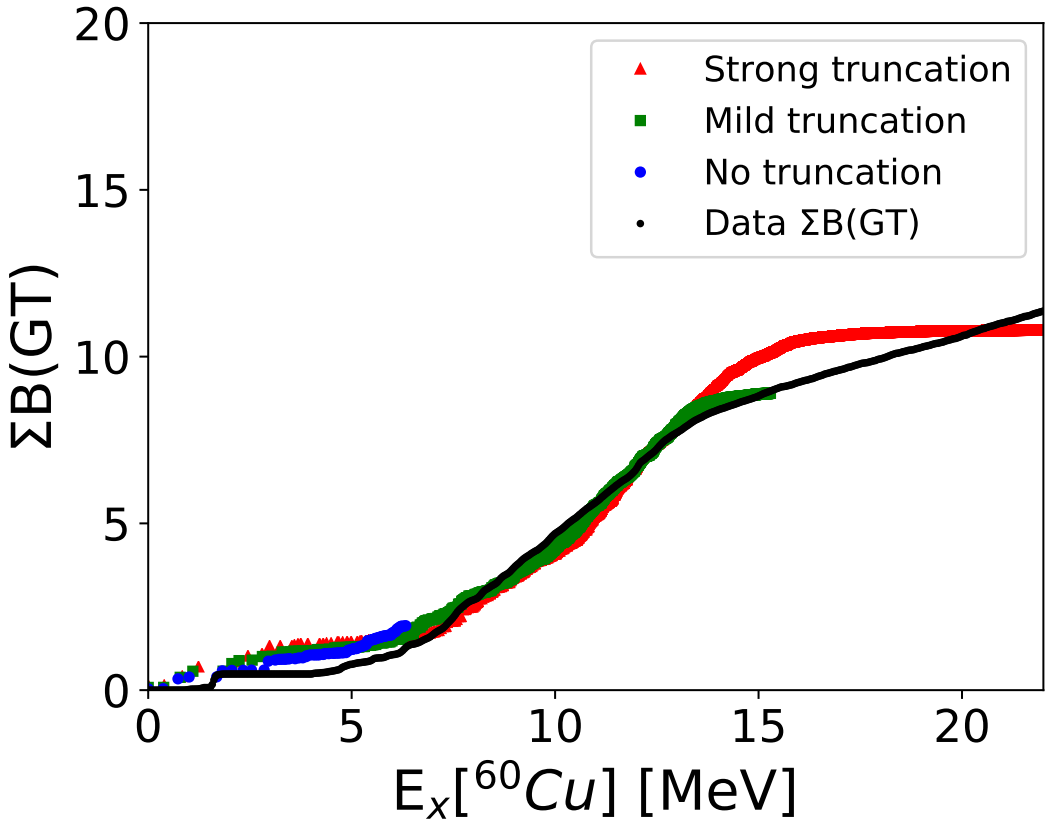

Figure 5.9 The extracted cumulative B(GT) distribution after removing IAS was compared to theoretical shell-model calculations depicted in blue, green, and red for no truncation, mild truncation, and strong truncation, respectively. All shell-model calculations were scaled by a factor of 0.55 [138] to account for a well-known quenching of the GT strength.

5.3.3 Extracted B(GT) at 14.4 MeV for $T_>$ State

Studying $T_0 + 1$ excitations is of interest as these states are the analogs of states populated in the ^{60}Ni(n,p) reaction, see Figure 2.3. These transitions can be used to estimate the electron-capture rate in core-collapse supernovae [139] for which GT strengths in the β^+ direction are important. The extraction of the first $T_0 + 1$ state, located at $E_x(^{60}\text{Cu}) = 14.4$ MeV was previously analyzed through the ^{60}Ni(p,n) reaction [139], see Figure 5.10. The extracted B(GT) for the ^{60}Ni(n,p) reaction after taking into consideration the isospin scaling factor as discussed in section 2.2 to scale the strength from the ^{60}Ni(p,n) reaction to ^{60}Ni(n,p) reaction was 0.95 ± 0.15. The scaling factor was 15 calculated by using the equation in section 2.2 [139]. A similar analysis but with the $(^3\text{He}, t)$ reaction was performed in this thesis.

The process of extracting the B(GT) for the transition to the $T_0 + 1$ state around 14.4 MeV in the ^{60}Ni(^{3}He,t) reaction at 140 MeV/u is shown in Figure 5.11. Figure 5.11(a) illustrates the differential cross section between 13.5 and 16 MeV at forward scattering angles emphasizing the prominent $T_0 + 1$ state at an excitation energy of $E_x(^{60}\text{Cu}) = 14.4$ MeV. Figure 5.11(b) displays the fitted data using a first-order polynomial background and a Gaussian function. Following background subtraction, Figure 5.11(c) visualizes the resulting peak centered around 14.4 MeV. Subsequently, a MDA was performed to extract the cross section at 0° and the B(GT) following the same process as in section 5.3.1.

In order to convert the cross-section from data to B(GT), the cross sections were extrapolated to $q = 0$ momentum transfer and divided by unit cross-section ($\hat{\sigma}_{GT} = 7.614$). In this work, the extracted B(GT) of $T_0 + 1$ state at 14.4 MeV is 0.86 ± 0.09 (stat.)±0.08 (syst.). The value is consistent with the result from the ^{60}Ni(p,n) experiment [139].

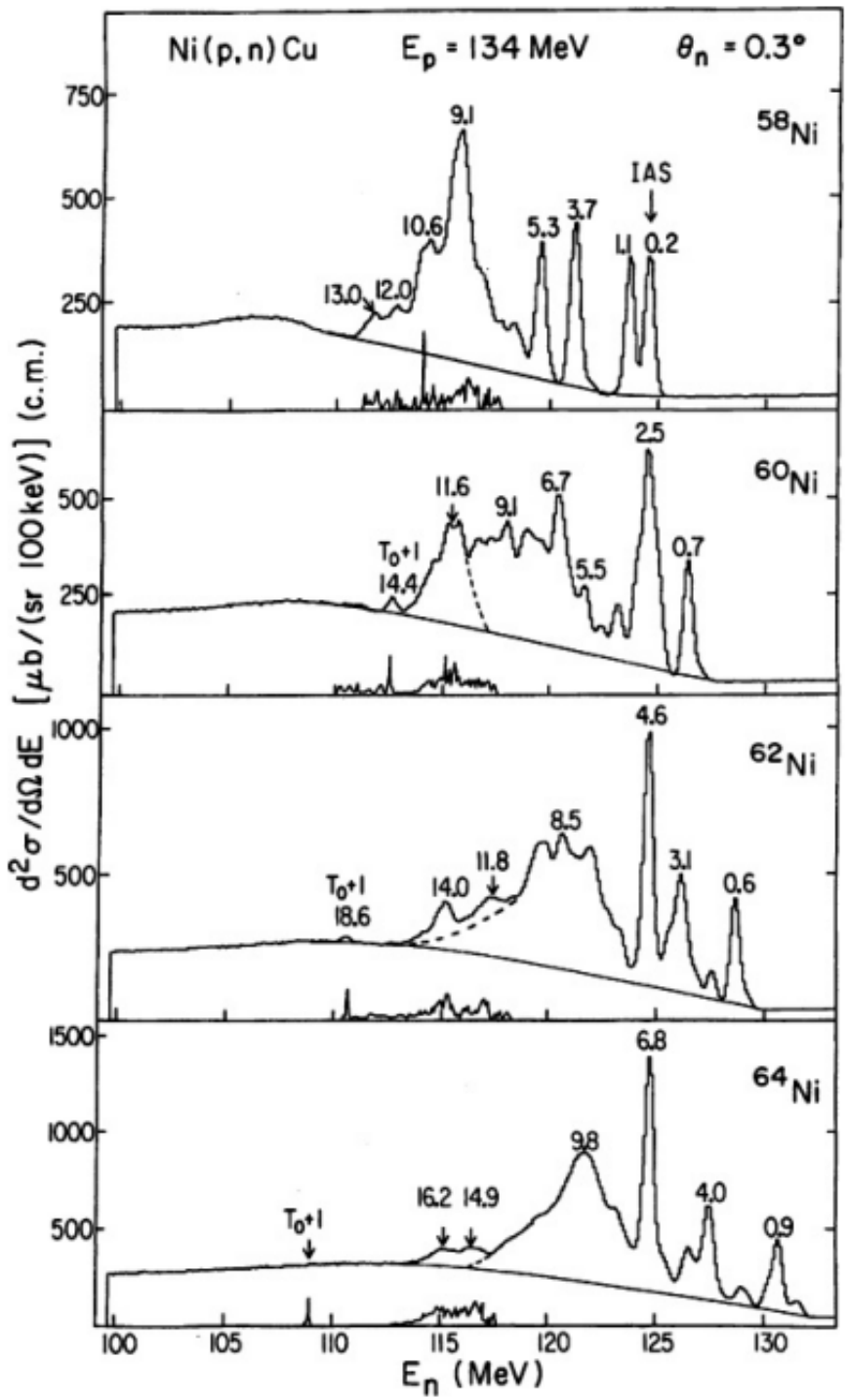

Figure 5.10 Spectra for ^{58,60,62,64}Ni(p,n) reactions at 134.4 MeV, the $T_0 + 1$ state in ^{60}Ni nucleus is shown at 14.4 MeV. Figure taken from [139].

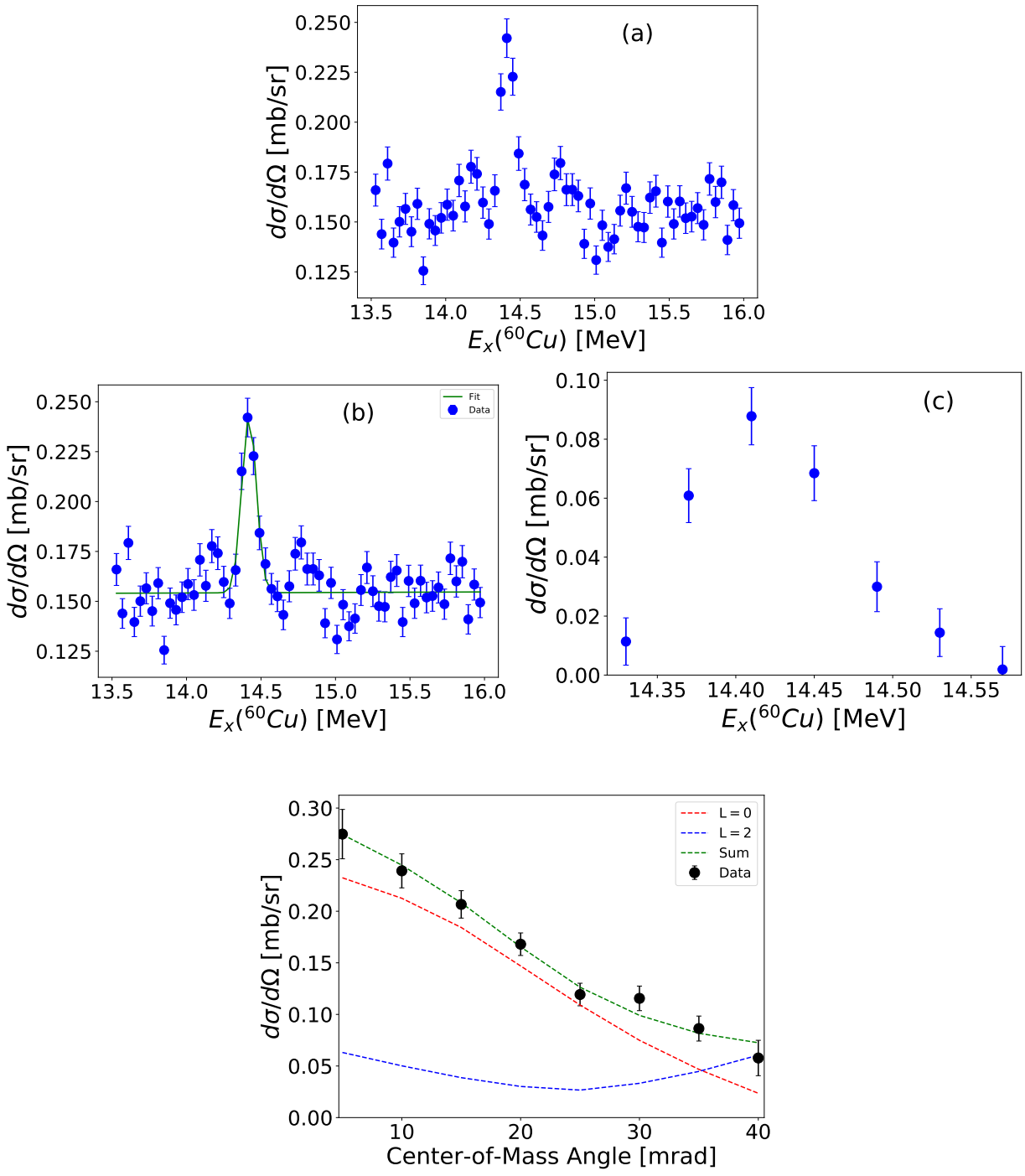

Figure 5.11 Extracting B(GT) for the transition to the $T_0 + 1$ state at 14.4 MeV in the ^{60}Ni(^{3}He,t) reaction at 140 MeV/u . Figure (a) depicts the differential cross section between 13.5 and 16 MeV. Figure (b) shows the fitted peak, while Figure (c) displays the background subtracted peak centered at E_x = 14.4 MeV. Figure (d) presents the angular distribution and the MDA.

5.3.4 Comparison with Theory, (p, p') and (e, e')

In addition to the transition to the T_0 + 1 state at 14.4 MeV, it is likely that are other GT transitions to T_0 + 1 states above 14.4 MeV. In this work, it was attempted to extract the strength of these transitions by using a simple background subtraction, as shown in Figure 5.12. Figure 5.12(a) shows the differential cross section between E_x = 13 MeV and E_x = 20 MeV for scattering angles below 5 mrad, where GT transitions are dominant. Besides the peak at 14.4 MeV, several other weaker peaks are visible. A simple linear background was subtracted, as shown in Figure 5.12(b), where the red dashed lines indicates the estimated uncertainty in this background model. The background-subtracted differential cross sections are shown in Figure 5.12(c). The extracted B(GT) strengths are shown in Figure 5.12(d). To verify that these states are T_0 + 1 states, the excitation energies of the states were compared with known corresponding T_0 + 1 states measured in the ^{60}Ni(p, p') and ^{60}Ni(e, e') reactions [140, 141], these excitation energies are indicated in red and green arrows, respectively, in Figure 5.12(d). Up to about 16.5 MeV, it appears that several T_0 + 1 states can be identified. At higher excitation energies, no (p, p') or (e, e') data are available and it cannot be proven that the peaks found are transitions to T_0 + 1 states. The results were compared with shell-model calculations with the GXPF1A interaction in the pf-shell model space (no truncation) in the (n,p) direction. They are shown as the black dots in Figure 5.12(d).

Aside from the transition to the first T_0 + 1 states, it is not possible to find a one-to-one correspondence between states found in the experiment and states calculated in the shell-model. In addition, more strength is found in the theoretical calculations than observed in the experiment.

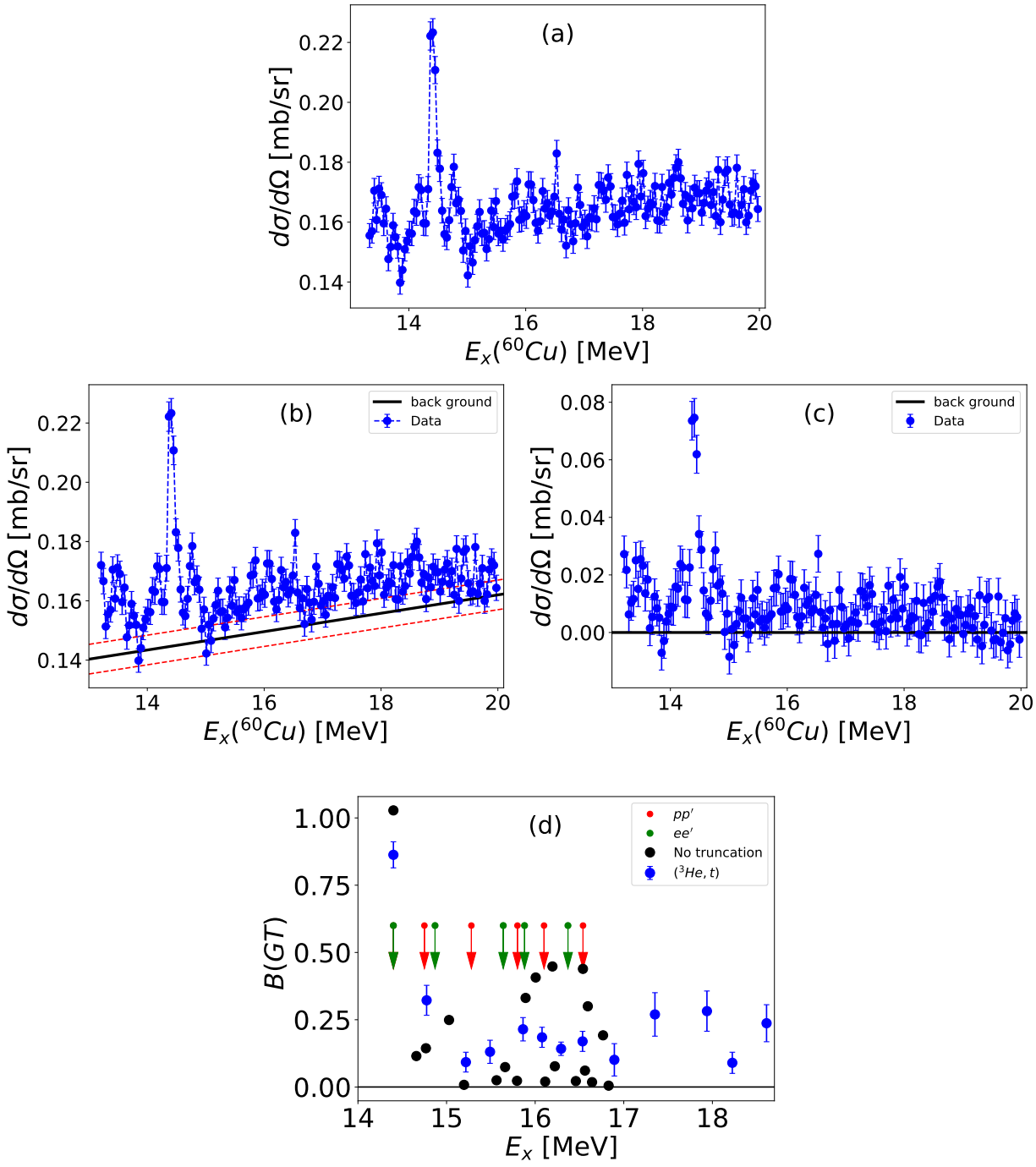

Figure 5.12 Extraction of the B(GT) for the transitions to possible T_0+1 states. Figure (a) illustrates the differential cross sections between 13 and 20 MeV. Figure (b) shows the background estimation, while Figure (c) shows the differential cross sections of the same spectrum after the background has been subtracted. Figure (d) presents the extracted B(GT) from the measured in the ^{60}Ni(^{3}He,t) data in blue dots and shell-model calculations in the (n,p) direction in black dots. The location of the states are compared with available data for the location of the T_0+1 states in (p, p') in red and (e, e') in green data [140, 141].

5.4 Background or quasifree-continuum Estimation

Extracting the Isovector Spin Giant Monopole Resonance (IVSGMR), Isovector Spin Giant Dipole Resonance (IVSGDR), and other isovector giant resonances with higher multipolarities at higher excitation energies is complicated by the presence of the quasifree-continuum in charge-exchange reactions. As the excitation energy increases, the quasifree-continuum becomes more pronounced, making it difficult to observe and analyze the resonant structures of interest. The quasifree-continuum arises from non-resonant processes. At energies of an excess of 100 MeV/u the dominant component of the continuum are quasifree reactions in which the projectile interacts with a single nucleon and the other nucleons in the target are spectators.

In quasifree reactions in the (^{3}He,t) reaction, the ^{3}He projectile interacts with a single neutron in the target, where the rest of the nucleus acts as a spectator, and the neutron behaves as a free particle, except for its binding energy. This CE process involves the transformation of this neutron into a proton, leading to its "knockout" from the nucleus. The process must occur above the proton separation energy to facilitate this knockout. As the transferred energy increases, removing neutrons from deeper shells with higher binding energies becomes possible. More details about the quasifree-continuum origin can be found in Refs. [142, 143, 144, 145, 146, 147, 42, 145, 148].

The contribution of quasifree reactions is uncertain. If quasifree reactions do not peak at forward scattering angles, the MDA conveniently includes contributions from the continuum into components associated $\Delta L \geq 2$, making the extraction of $\Delta L = 0$ and $\Delta L = 1$ strength straightforward. However, if the continuum contribution peaks at forward scattering angles, it will impact the strength extraction of $\Delta L = 0$ and $\Delta L = 1$ resonances and it is better to remove the continuum contribution before the MDA. In this work, we will compare the two approaches. The quasifree-continuum has been estimated using a phenomenological approach. Initially, Erell et al. [42] introduced this description for π charge-exchange reactions, and later, it was also applied to (^{3}He,t) reactions [145, 146, 147, 148]. For the case of (^{3}He,t) reaction, it has the following form:

$$\frac{d^2\sigma}{d\Omega dE} = N\frac{1 - exp[(E - E_0)/T]}{1 + [(E - E_{QF})/W]^2}, \tag{5.3}$$

where E_{QF} is the centroid energy of a Lorentzian distribution that undergoes a shift relative to

the energy of the free process, $E_{t(free)}$, due to various contributing factors. These factors include the proton binding energy S_p, the excitation energy E_x of the neutron-hole state, and the Coulomb barrier B_{Coul} experienced by the proton:

$$E_{QF} = E_{t(free)} - (S_p + E_x + B_{Coul}), \tag{5.4}$$

The energy E_x becomes zero only when the neutron is removed from the orbit closest to the Fermi level. The width W is attributed to the Fermi motion inside the nucleus, while the exponential term arises from Pauli blocking effects. The cut-off energy E_0 is defined by:

$$E_0 = E_{t(gs)} - S_p, \tag{5.5}$$

and E is derived from E_x by:

$$E = E_{proj} + Q_{gs} - E_x \tag{5.6}$$

The parameter T is a temperature parameter. The normalization (N) is typically selected to match the full cross section at high excitation energies, which likely leads to an overestimation of the quasifree-continuum due to the contribution from non-quasifree reactions at high excitation energies.

In this work, equation 5.3 was used to estimate the quasifree-continuum in spectra from ^{60}Ni(^{3}He,t) reaction as shown in Figure 5.13 and Figure 5.14. The parameters in Eq. 5.3 used in calculating the quasifree curves are described in Table 5.1. The value of the normalization factor N as a function of the scattering angle is shown in Figure 5.15. It was determined by scaling the calculated quasifree curve to the experimental differential cross sections for excitation energies above 55 MeV. N peaks at forward scattering angles, although the angular dependence is weak.

In order to extract monopole and dipole strengths from ^{60}Ni(^{3}He,t) data, the estimated quasifree-continuum was removed from data as shown in Figures 5.16 to 5.19. A comparison was made between the MDA results for 1 MeV bins up through 60 MeV in excitation energy before and after removing the quasifree-continuum in the ^{60}Ni(^{3}He,t) data for a scattering angle bin ranging from 0 to 40 mrad as shown in Figure 5.16 to 5.17. The top figure displays the MDA results

before removing the quasifree-continuum, whereas the bottom figure displays the MDA after the quasifree-continuum removal within the same angular range. It is observed that, after the subtraction of the quasifree-continuum, tails that extend to high excitation energies for $\Delta L = 0$ and $\Delta L = 1$ components are strongly reduced.

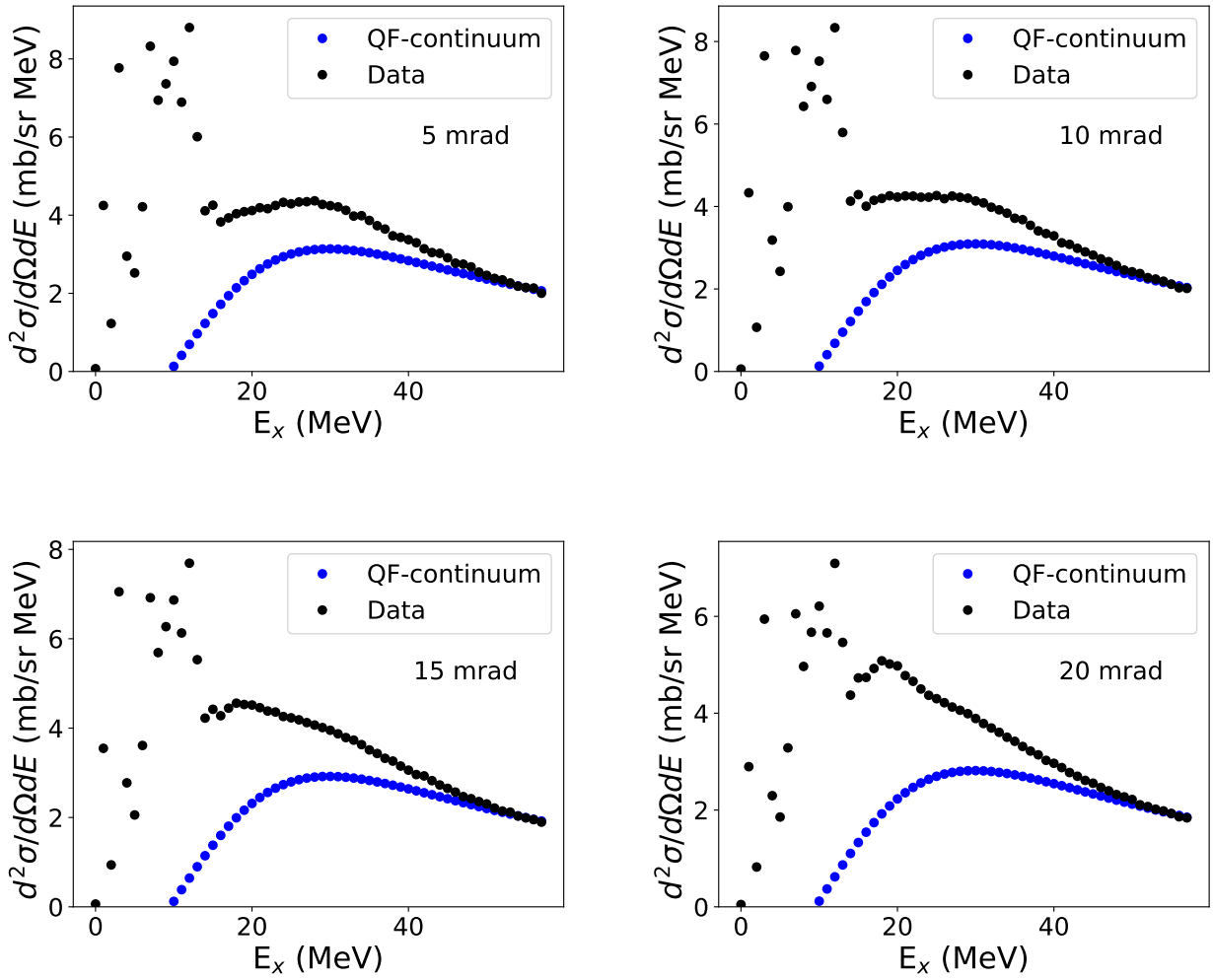

Figure 5.13 Estimating quasifree-continuum for each 5 mrad wide angular bin via the ^{60}Ni(^{3}He,t) reaction at 140 MeV/u for scattering angle bin from 5 to 20 mrad angular distribution. The black dots in the figure represents the experimental data, while the blue dots illustrate the quasi-free curve used for comparison.

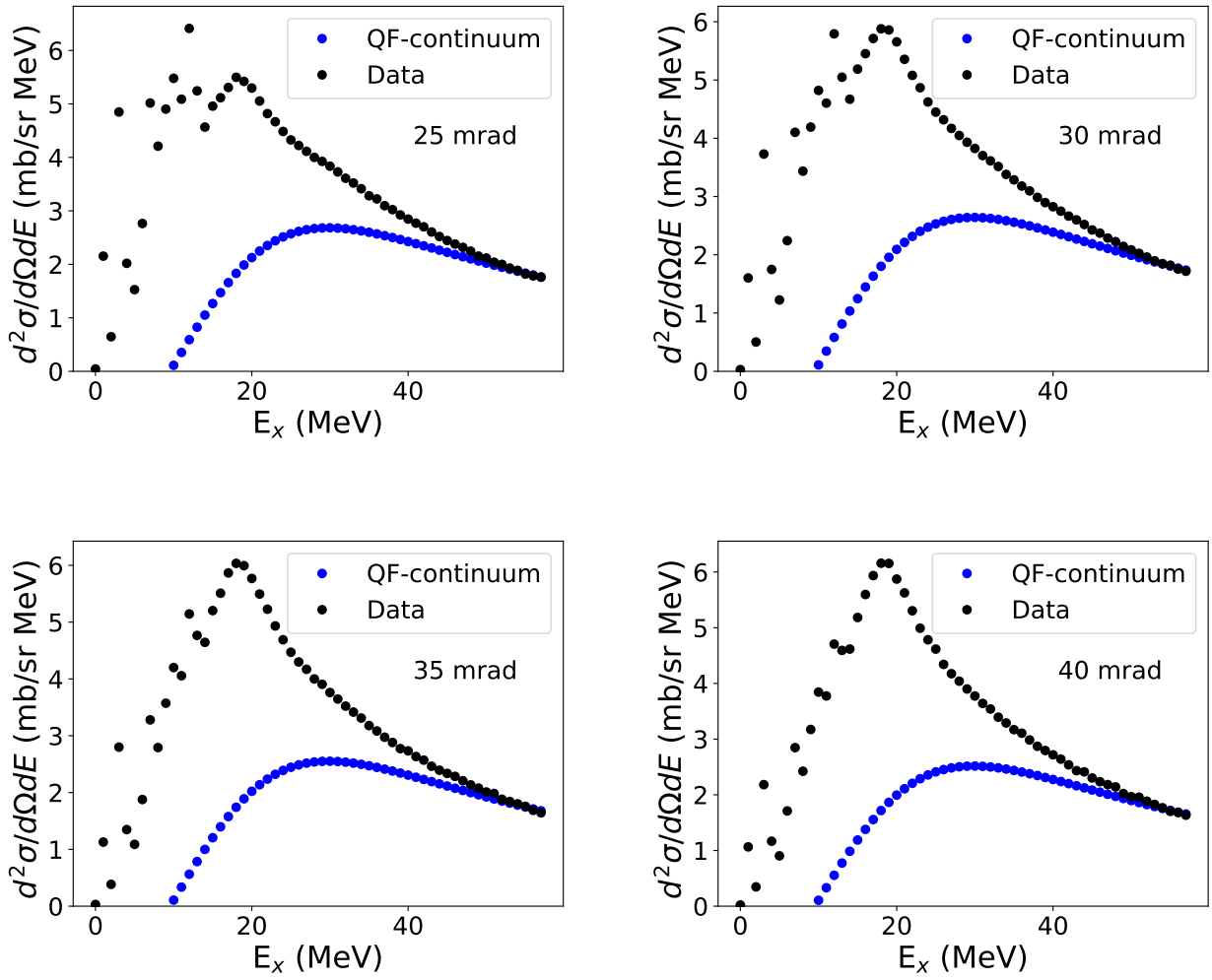

Figure 5.14 Estimating quasifree-continuum for each 5 mrad wide angular bin via the ^{60}Ni(^{3}He,t) reaction at 140 MeV/u for scattering angle bin from 25 to 40 mrad angular distribution. The black dots in the figure represents the experimental data, while the blue dots illustrate the quasi-free curve used for comparison.

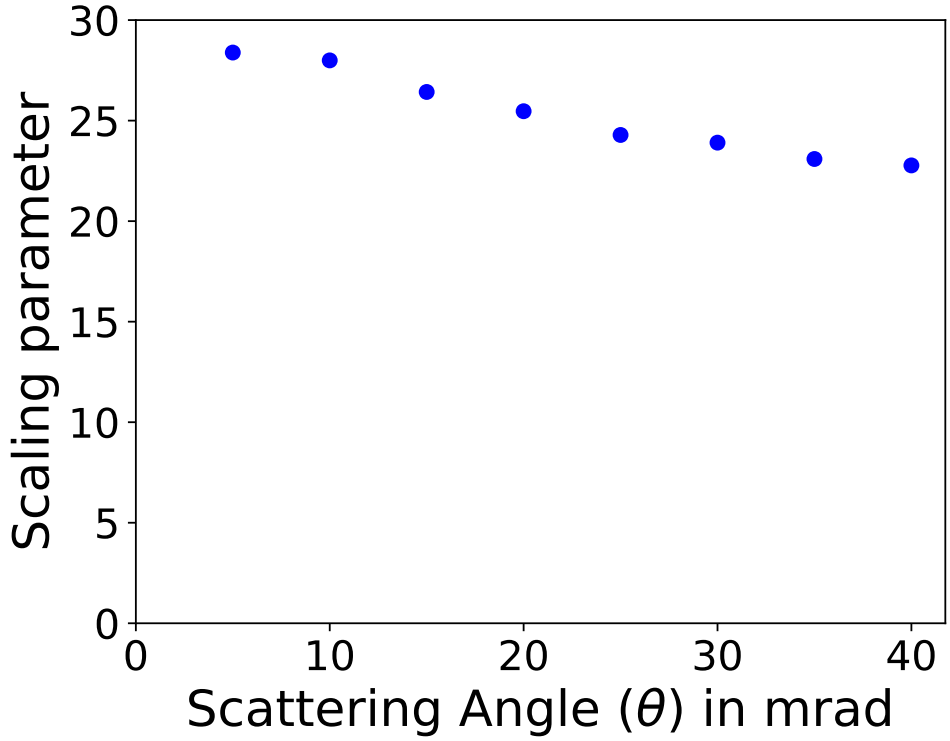

Figure 5.15 Normalizing parameters (N) from fit was used to match the full cross-section at high excitation energies for each 5 mrad wide angular bin in (^{3}He,t) data.

Table 5.1 Parameters used in calculating the quasi-free curve/quasifree-continuum via the ^{60}Ni(^{3}He,t) reaction at 140 MeV/u.

N	Normalization, fit	fit
$Q_{(gs)}$	Q value for ^{60}Ni(^{3}He,t)	-6.147
nQ	Q value for n(^{3}He,t)p	0.762 MeV
E_{proj}	Beam energy (^{3}He)	420 MeV
$E_{t(free)}$	Energy of the free triton, $\left[E_{t(free)} = E_{proj} + nQ\right]$	420.762 MeV
$E_{t(gs)}$	Ground state energy of the triton, $\left[E_{t(gs)} = E_{proj} - Q\right]$	413.852
S_p	Proton separation energy for ^{60}Ni	9.922 MeV
B_{Coul}	Coulomb barrier for the proton	7.3 MeV
E_x	Excitation energy of the neutron hole state	2 MeV
E_{QF}	Quasi-free energy, $E_{QF} = E_{t(free)} - (S_p + E_x + B_{Coul})$	401.932 MeV
E_0	$E_{t(gs)} - S_p$	404.3196 MeV
W	Width of resonance, fit	fit
T	Temperature parameter	100

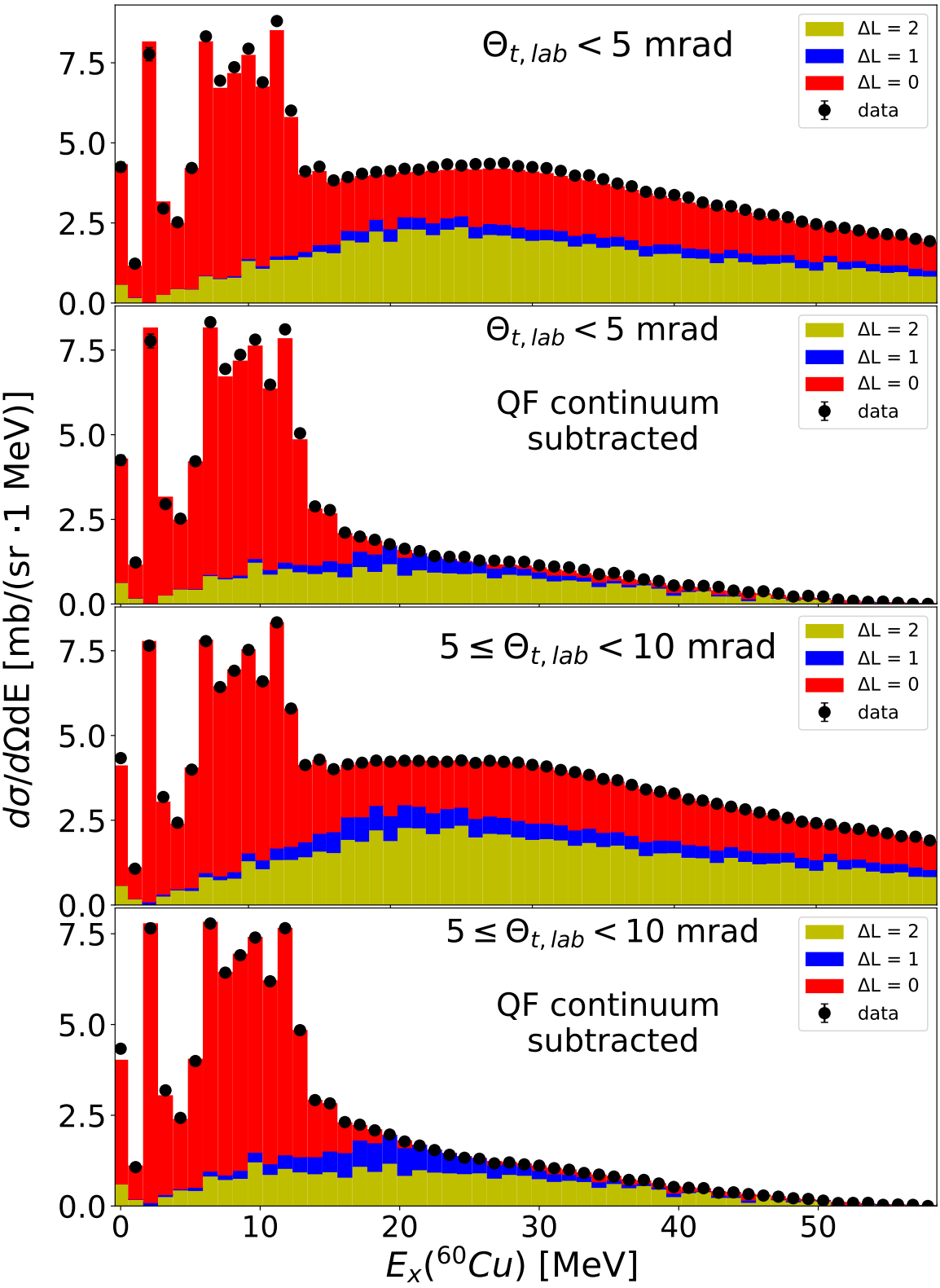

Figure 5.16 The MDA results at 1 MeV bin from ^{60}Ni(^{3}He,t) data for a scattering angle bin ranging from 0 to 10 mrad. The top figure illustrates the MDA results before removing the quasifree-continuum, while the bottom figure shows the same results after the quasifree-continuum removal within the same angular range.

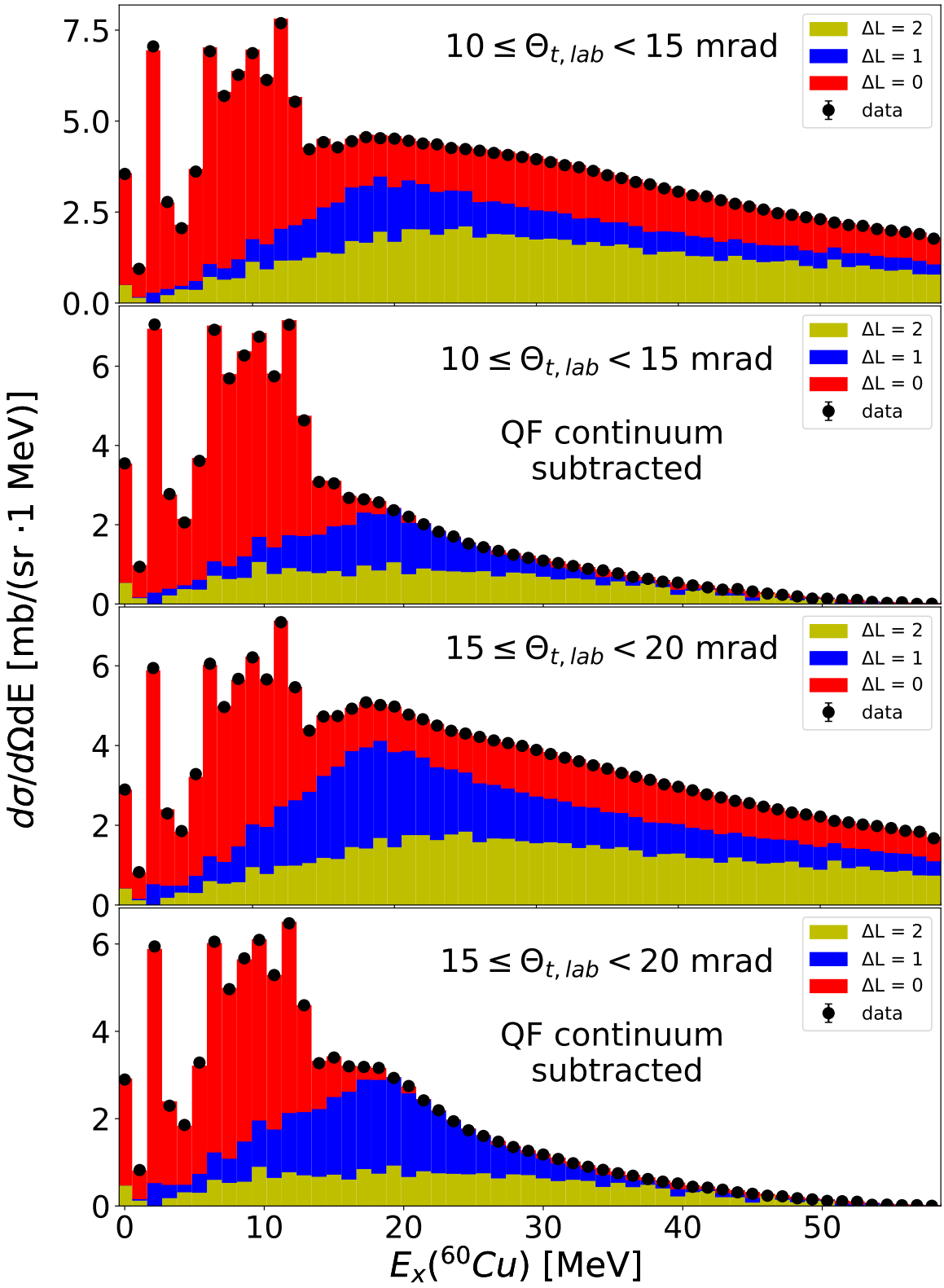

Figure 5.17 The MDA results at 1 MeV bin from ^{60}Ni(^{3}He,t) data for a scattering angle bin ranging from 10 to 20 mrad. The top figure illustrates the MDA results before removing the quasifree-continuum, while the bottom figure shows the same results after the quasifree-continuum removal within the same angular range.

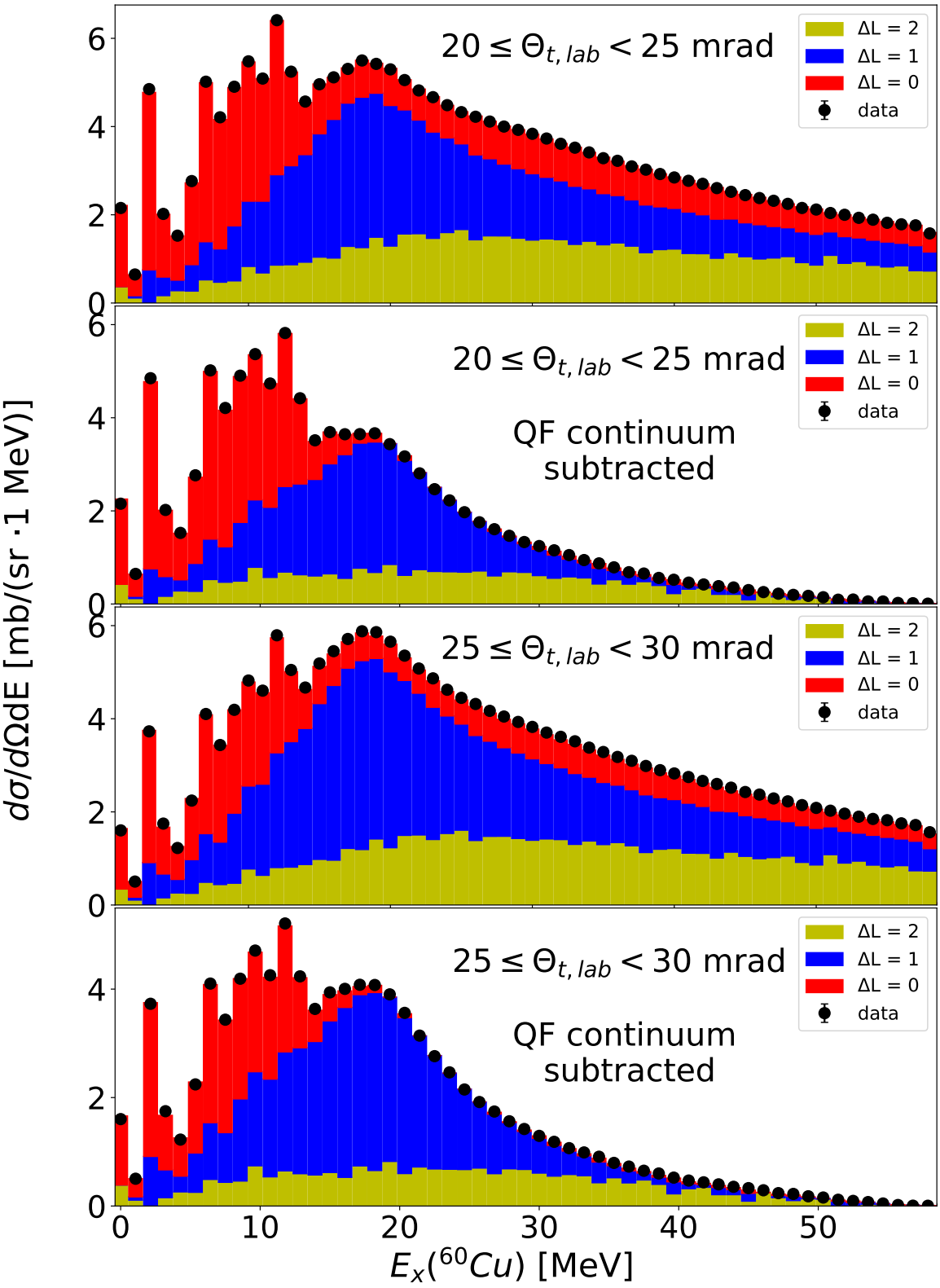

Figure 5.18 The MDA results at 1 MeV bin from ^{60}Ni(^{3}He,t) data for a scattering angle bin ranging from 20 to 20 mrad. The top figure illustrates the MDA results before removing the quasifree-continuum, while the bottom figure shows the same results after the quasifree-continuum removal within the same angular range.

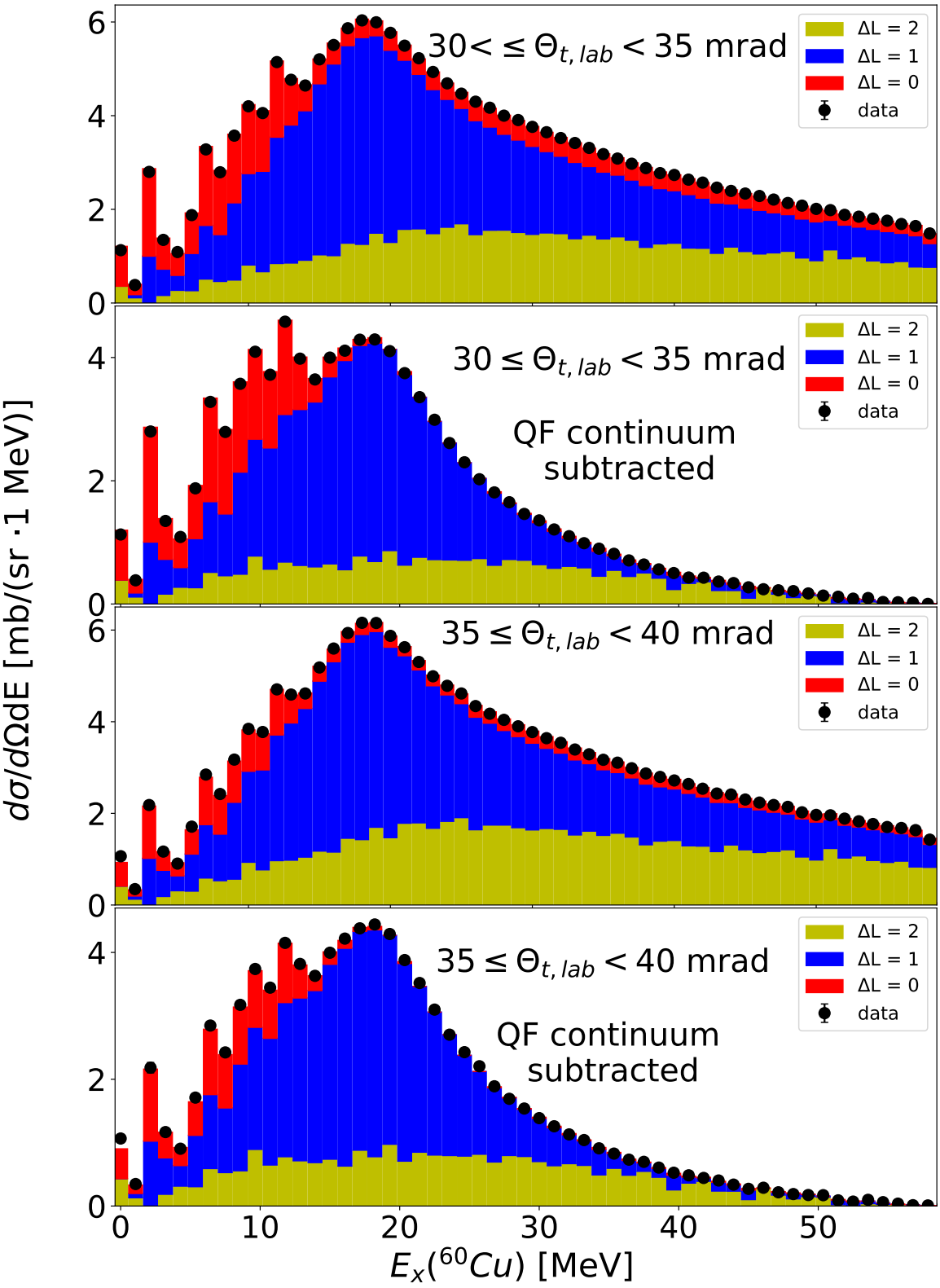

Figure 5.19 The MDA results at 1 MeV bin from ^{60}Ni(^{3}He,t) data for a scattering angle bin ranging from 30 to 40 mrad. The top figure illustrates the MDA results before removing the quasifree-continuum, while the bottom figure shows the same results after the quasifree-continuum removal within the same angular range.

5.5 Extraction of the Isovector Spin Giant Monopole Strength

Due to the common transition of $\Delta L = 0$ for the GT, IVGMR, and IVSGMR excitations, their strength contributions cannot be distinguished solely through the MDA. Although some GT strength can be situated at excitation energies above 20 MeV, it is of a non-resonant nature and is expected to be weakly excited compared to the IVGMR and IVSGMR. In this work, separating the strength contribution of the IVSGMR/IVGMR from that of GT transition was done by a simple assumption that the cross sections associated with $\Delta L = 0$ at low ($\leq$ 20 MeV) and high ($>$ 20 MeV) excitation energies correspond to the excitations of GT states and the IVSGMR/IVGMR, respectively. The extraction of the B(GT) strength was discussed in section 5.3.

To make an assessment of how much of the expected resonance strength for the IVSGMR/IVGMR is found in the analysis, the extracted cross sections associated with $\Delta L = 0$ in the MDA at 0° were compared with the calculated cross sections in DWBA with transition densities calculated in normal modes (see section 3.4.2). Figure 5.20 shows the extracted ratio of $\sigma(0°)\big|^{exp}_{dL=0}$ to $\sigma(0°)\big|^{DWBA}_{IVSGMR/IVGMR}$ for the MDA analysis performed before and after the removal of the quasifree-continuum contributions. Figure 5.20 also includes the summed fractions as a function of excitation energy, which provides a measure of how much of the expected normal-modes strength is observed in the analysis. Figure 5.20(a) and (b) show the extracted ratios after quasifree-continuum subtraction, while Figure 5.20(c) and (d) shows the same analysis before quasifree-continuum subtraction. In the former case, monopole contribution at excitation energy between 20 to 50 MeV was found to be 8% of the expected strength from the normal-modes calculation. It is therefore likely the background subtraction removed a fraction of the isovector spin giant monopole strength.

In the latter case, the strength distribution shows no sign of resonance structure, and three times the expected strength is extracted. This indicates that the removal of the quasifree-continuum is important. We conclude that in order to extract strengths for the IVGMR and IVSGMR, an experimental method for removing the quasifree-continuum is required. In the past, this has been achieved by requiring a coincidence between the (^{3}He,t) and protons at backward angles [2, 34, 149]. The reactions that contribute to the quasifree-continuum are associated with a proton emitted at the

forward scattering angles. Protons emitted follow the excitation of the IVGMR/IVSGMR and are distributed isotropically. Hence the coincidence with protons at backward angles provides a good filter for reactions in which the giant resonances are excited.

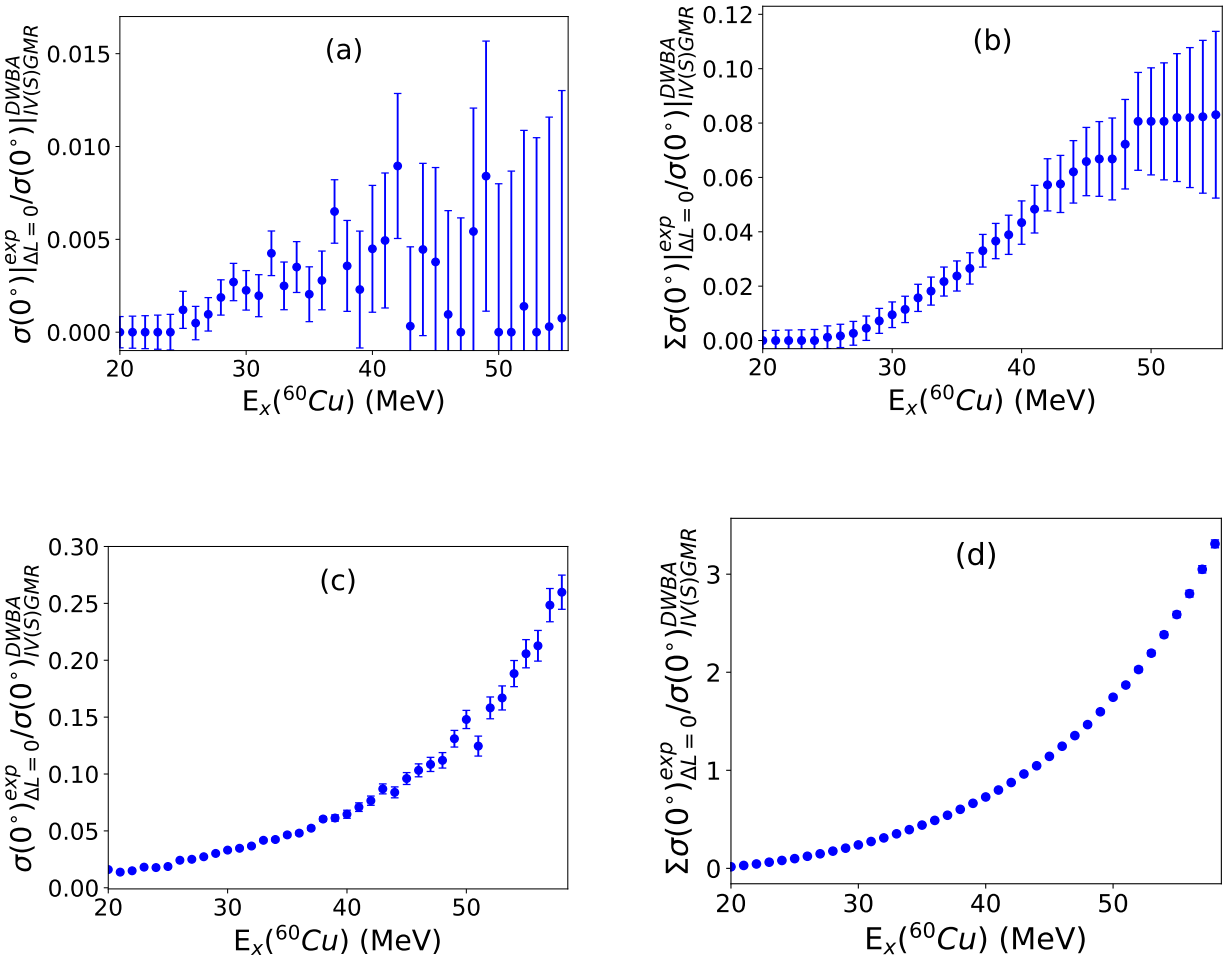

Figure 5.20 Figure (a) and (b) shows the extracted ratios of $\sigma(0^\circ)|^{exp}_{dL=0}$ to $\sigma(0^\circ)|^{DWBA}_{IVSGMR,IVGMR}$ from ^{60}Ni(^{3}He,t) reaction at 140 MeV/u after the quasifree-continuum subtraction. Conversely, Figures (c) and (d) illustrate the same ratios derived from the original data without the quasifree-continuum subtraction. In Figure (b) we observe that the anticipated resonance strength for IVSGMR/IVGMR is 8% of the expected normal-modes strength, while in Figure (d) more than 300% of expected normal-modes strength is observed.

5.6 Extraction of the Isovector Spin Giant Dipole Strength

As previously discussed in section 2.5, the IV(S)GDR consists of three components (0^-, 1^-, and 2^-). However, in the data, these components are not distinguishable from one another due to their overlap and equal ΔL value and angular distribution. The summed strength peaks at around 18 MeV.

Here, we compared the differential cross sections extracted for $\Delta L = 1$ transitions with the DWBA calculations using the normal-mode framework. The comparison is performed for $35 \leq \Theta_{t,lab} < 40$ mrad, where the dipole transitions peak. As was done in the previous section 5.5 for the IVGMR/IVSGMR, the results from the analysis with and without subtraction of the quasifree-continuum were compared. The results are shown in Figure 5.21. With the removal of the quasifree-continuum, a strong resonance is observed that peaks at $E_x = 18$ MeV. The ratio between the extracted and theoretical cross sections is about 1.25, suggesting that the quasifree-continuum subtraction works quite well. Since, the $\Delta L = 1$ excitations peak at backward angles, unlike the quasifree-continuum, systematic uncertainties induced by the subtraction of the quasifree-continuum appear less severe than for the monopole transitions. Without the subtraction of the quasifree-continuum, a large amount of excess cross section above $E_x = 30$ MeV is seen, indicating that the subtraction of the quasifree-continuum is necessary.

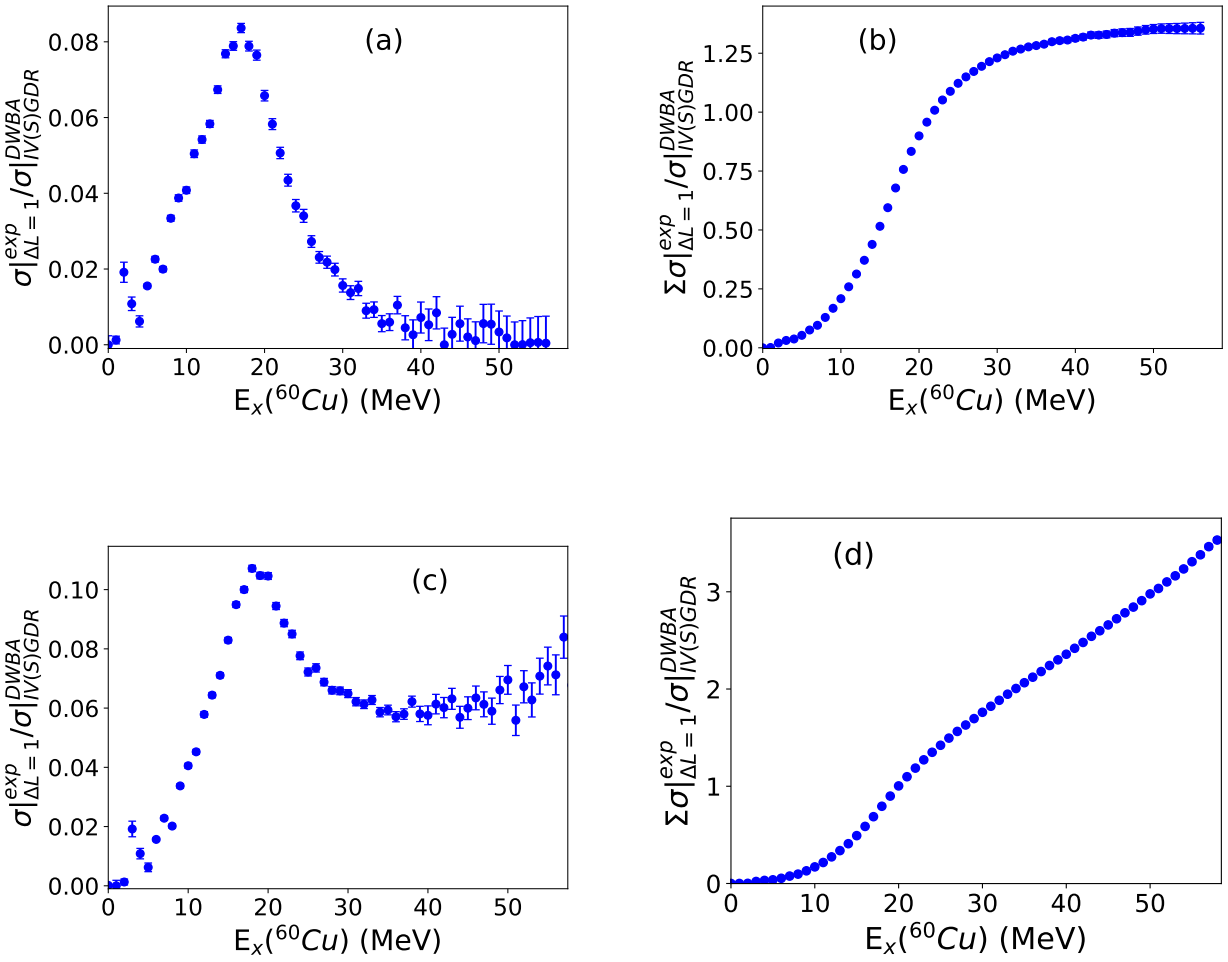

Figure 5.21 The isovector spin giant dipole strength was extracted from the ^{60}Ni(^{3}He,t) reaction at 140 MeV/u. In Figure (a), we depict the ratios of $dL = 1$ components at 0° derived from both the measured differential cross sections (MDA) and the theoretical calculation using DWBA. Figure (b) showcases the cumulative ratio of the results presented in Figure (a). In contrast, Figures (c) and (d) depict the identical ratios calculated from the original data without quasifree-continuum subtraction.

CHAPTER 6

CONCLUSION AND OUTLOOK

6.1 Summary

This dissertation focused on probing isovector giant resonances in ^{60}Cu up to high excitation energies (60 MeV) using the (^{3}He,t) reaction at 140 MeV/u. The experiment was performed at the Grand Raiden Spectrometer at Osaka University's Research Center for Nuclear Physics (RCNP). The method involved directing a ^{3}He beam of 420 MeV with an intensity of 4 pnA onto a ^{60}Ni foil target of 2 mg/cm^2. The tritons were identified and analyzed in the focal plane. From the measured position and angles in the focal plane, the momentum vector of the triton was deduced, from which the excitation energy in ^{60}Cu and scattering angle were determined.

To investigate the Gamow-Teller strengths, the isobaric analog state, the isovector (spin) monopole, and dipole giant resonances, a multiple decomposition analysis (MDA) was performed. The differential cross sections were fitted with a linear combination of the angular distributions associated with different angular momentum transfer ΔL ($\Delta L = 0, 1, 2, ...$) calculated in distorted wave Born approximation.

Different giant resonances were observed at different excitation energies. For the (^{3}He,t) reaction at 140 MeV/u, the GTR, IAS, and monopole excitations are associated with $\Delta L = 0$, so they peak at 0° scattering angle and their presence is strongly enhanced in the spectrum gated on scattering angles between 0 and 5 mrad. Dipole excitations peak at small but finite angles and their features are enhanced at scattering angles between 35 and 45 mrad. The IAS was found to reside at $E_x(^{60}\text{Cu}) = 2.55$ MeV, and the main component of the GTR appears at excitation energies of $\sim$ 10 MeV. The IVSGDR peaks at an excitation energy of about 18 MeV. The IVSGMR and IVGMR were seen at the excitation energies of about 35 MeV and are not easy to identify due to their large widths.

For excitation energies up to 20 MeV, the MDA analysis resulted in a total GT strength of 10.6 ± 1.45 (stat.) ± 1.19 (syst.). At higher excitation energy additional strength is found that is associated with $\Delta L = 0$ and likely contains additional GT strength. However, at high excitation energies

contributions from IVSGMR are also expected. The study compared the extracted Gamow-Teller Strength B(GT) running sum with shell-model calculations using the GXPF1A interaction. Various truncation levels were applied to calculate strength distributions, and all calculations were scaled by a factor of 0.56 to address quenching effects. The comparison of the GT strengths revealed reasonable agreement between experiment and shell-model calculations.

Gamow-Teller strengths for T_0 + 1 states were extracted. The extracted B(GT) for the T_0 + 1 state at 14.4 MeV was found to be 0.86 ± 0.09 (stat.) ± 0.08 (syst.), consistent with results from the ^{60}Ni(p,n) experiment. Additional GT transitions to T_0 + 1 states above 14.4 MeV in ^{60}Cu were investigated. Several peaks, apart from the 14.4 MeV peak, were observed. To confirm that these states are T_0 + 1 states, their excitation energies were compared with known T_0 + 1 states from ^{60}Ni(p, p') and ^{60}Ni(e, e') reactions. Up to about 16.5 MeV, multiple T_0 + 1 states were identified. However, beyond this energy, there is no available data to conclusively determine if the observed peaks via ^{60}Ni(^{3}He,t) data and shell-model calculations correspond to T_0 + 1 states.

The contributions from the GT and IVGMR/IVSGMR excitations were extracted simultaneously as all are characterized by $\Delta L = 0$ transitions. While some GT strength likely appears above 20 MeV, it lacks a resonant nature. To separate the IVSGMR/IVGMR from GT transitions, an assumption was made that at low excitation energy ($\leq$ 20 MeV) $\Delta L = 0$ cross sections correspond to GT states, $\Delta L = 0$ strength at high excitation energies ($>$ 20 MeV) is due to the excitation of the IVSGMR/IVGMR. After quasifree-continuum subtraction, monopole contributions at 20-50 MeV were found to be 8% of the normal-mode strength, indicating that the continuum removal also removed a portion of the isovector spin giant monopole strength. Without the quasifree-continuum subtraction, the strength distribution lacks resonance structure and is three times the expected strength highlighting the importance of continuum removal. To obtain a better result for the IVSGMR, an experimental technique to remove the continuum must be used. This is possible by requiring coincidences with protons from the decay of the IVSGMR, as pursued in the experiments.

The contributions from the dipole resonances were extracted, and the differential cross sections for $\Delta L = 1$ transitions were compared with DWBA calculations using the normal-mode framework.

Similar to the analysis for the IVGMR/IVSGMR, results with and without quasifree-continuum subtraction were compared. With continuum subtraction, a strong resonance around $E_x = 18$ MeV was observed, with a ratio of extracted to theoretical cross sections at about 1.25, suggesting that the continuum subtraction is reasonable. Systematic uncertainties from continuum subtraction are less severe for $\Delta L = 1$ excitations due to their backward-angle peaking behavior, in contrast to monopole transitions. Without continuum subtraction, significant excess cross section above $E_x = 30$ MeV emphasizes the necessity of the subtraction.

6.2 Future Outlook

In this work, it has been shown that the (^{3}He,t) reaction at 140 MeV/u is a valuable tool for extracting information about isovector giant resonances. However, the analysis is complicated by the presence of the quasifree-continuum, and future studies with this probe would benefit from the measurement of protons emitted from the excited nucleus. While the quasifree-continuum is associated with protons directed at forward scattering angles, the decay after the excitation of isovector monopole giant resonances is associated with protons emitted isotropically. Therefore a coincidence measurement with protons at backward angles removes the contribution from the continuum. Such experiments have been performed successfully in the past, but require thick silicon detectors that are difficult to produce. It is well-kown that the extraction of the Gamow-Teller strengths via the (^{3}He,t) reaction provides high-quality tests of theoretical models. In the experiment studied here, the excitation energy resolution was modest (0.11 MeV) [FWHM]. By applying the dispersion matching techniques [130], superior resolutions can be achieved ($\sim$ 30 keV), which would be helpful for the study of T_0 + 1 Gamow-Teller states observed at high excitation energies.

The CE group at FRIB is preparing for the next (^{3}He,t) experiment at RCNP. The target will be ^{92}Zr and the goals will be to study transitions that are important for understanding the production site of ^{92}Nb in the universe. Due to its long lifetime (^{92}Nb) is a potential cosmochronometer, but the production site is still unknown, which makes its use as a cosmochronometer difficult. Many of the techniques used in this thesis will also be used in the next experiment.

BIBLIOGRAPHY

[1] M. N. Harakeh and A. van der Woude. *Giant Resonances: Fundamental High-Frequency Modes of Nuclear Excitation*, volume 24. Oxford University Press, 2001.

[2] R. G. T. Zegers, S. Brandenburg, M. N. Harakeh, S. Y. Van der Werf, J. Jänecke, T. OḊonnell, D. A. Roberts, S. Shaheen, G. P. A. Berg, C. C. Foster, T. Rinckel, and E.J. Stephenson. Search for isovector giant monopole resonances via the ^{124}Sn(^{3}He, tn) reaction. *Phys. Rev. C*, 61:054602, 2000.

[3] R. G. T. Zegers. *Search for Isovector Giant Monopole Resonances. dissertation*. PhD thesis, University of Groningen, 1999.

[4] F. Osterfeld. Nuclear spin and isospin excitations. *Reviews of Modern Physics*, 64(2):491, 1992.

[5] K. Goeke and J. Speth. Theory of giant resonances. *Annual Review of Nuclear and Particle Science*, 32(1):65–115, 1982.

[6] A. Bohr and B. R. Mottelson. Nuclear structure, volume iwa benjamin. *New York, Amsterdam*, 1969.

[7] A. N. Bohr and B. R. Mottelson. *Nuclear Structure (in 2 volumes)*. World Scientific Publishing Company, 1998.

[8] W. G. Hitt, R. G. T. Zegers, C. Sullivan, M. Scott, K. Miki, R. Titus, B. A. Brown, B. Gao, S. Lipschutz, et al. 10. the ^{64}Zn(t, ^{3}He) charge-exchange reaction at 115 MeV per nucleon and application to ^{64}Zn stellar electron-capture. *Phys. Rev. C*, 98(015804):015804, 2018.

[9] P. E. Hodgson. *Nuclear reactions and nuclear structure*, volume 426. Clarendon Press Oxford, 1971.

[10] K. Ikeda, S. Fujii, and J. I. Funjita. The (p, n) reactions and beta decays. *Phys. Lett.*, 3, 1963.

[11] B. M. Loc, D. T. Khoa, and R. G. T. Zegers. Charge-exchange scattering to the isobaric analog state at medium energies as a probe of the neutron skin. *Phys. Rev. C*, 89:024317, 2014.

[12] P. Danielewicz and J. Lee. Symmetry energy ii: Isobaric analog states. *Nuc. Phys. A*, 922:1–70, 2014.

[13] T. N. Taddeucci, C. A. Goulding, T. A. Carey, R. C. Byrd, C. D. Goodman, C. Gaarde, J. Larsen, D. Horen, J. Rapaport, and E. Sugarbaker. The (p, n) reaction as a probe of beta decay strength. *Nuc. Phys. A*, 469(1):125–172, 1987.

[14] M. Ichimura, H. Sakai, and T. Wakasa. Spin–isospin responses via (p,n) and (n,p) reactions. *Progress in Particle and Nuc. Phys.*, 56(2):446–531, 2006.

[15] K. Langanke, G. Martínez-Pinedo, and R. G. T. Zegers. Electron capture in stars. *Reports on Progress in Physics*, 84(6):066301, 2021.

[16] K. Langanke and G. Martínez-Pinedo. Nuclear weak-interaction processes in stars. *Rev. Mod. Phys.*, 75:819–862, 2003.

[17] A. J. Mayer, M. Wieser, M. Alanssari, D. Frekers, W. Matthews, J. Dilling, and R. T. Thompson. Isotope abundance measurement of the half-life of the β-decaying nucleus ^{96}Zr from a 2.68 gyr zircon sample. *Phys. Rev. C*, 98(2):024617, 2018.

[18] D. Frekers and M. Alanssari. Charge-exchange reactions and the quest for resolution. *The European Physical Journal A*, 54(10):1–77, 2018.

[19] R. G. T. Zegers, T. Adachi, H. Akimune, Sam M. Austin, A. M. van den Berg, B. A. Brown, Y. Fujita, M. Fujiwara, S. Galès, C. J. Guess, M. N. Harakeh, H. Hashimoto, K. Hatanaka, R. Hayami, G.W. Hitt, M.E. Howard, M. Itoh, T. Kawabata, K. Kawase, M. Kinoshita, M. Matsubara, K. Nakanishi, S. Nakayama, S. Okumura, T. Ohta, Y. Sakemi, Y. Shimbara, Y. Shimizu, C. Scholl, C. Simenel, Y. Tameshige, A. Tamii, M. Uchida, T. Yamagata, and M. Yosoi. Extraction of weak transition strengths via the (^{3}He, t) reaction at 420 MeV. *Phys. Rev. Lett.*, 99:202501, 2007.

[20] R. G. T. Zegers, H. Akimune, Sam M. Austin, D. Bazin, A. M.van den Berg, G. P. A. Berg, B. A. Brown, J. Brown, A. L. Cole, I. Daito, Y. Fujita, M. Fujiwara, S. Galès, M. N. Harakeh, H. Hashimoto, R. Hayami, G. W. Hitt, M. E. Howard, M. Itoh, J. Jänecke, T. Kawabata, K. Kawase, M. Kinoshita, T. Nakamura, K. Nakanishi, S. Nakayama, S. Okumura, W. A. Richter, D. A. Roberts, B. M. Sherrill, Y. Shimbara, M. Steiner, M. Uchida, H. Ueno, T. Yamagata, and M. Yosoi. The (t,^{3}He) and (^{3}He,t) reactions as probes of Gamow-Teller strength. *Phys. Rev. C*, 74:024309, 2006.

[21] A. Arima. History of giant resonances and quenching. *Nuc. Phys. A*, 649(1-4):260–270, 1999.

[22] H. Sakai and K. Yako. Experimental determination of gamow-teller quenching value, landau-migdal parameterg nδ and pion condensation. *Nuc. Phys. A*, 731:94–105, 2004.

[23] K. Yako, H. Sakai, M. B. Greenfield, K. Hatanaka, M. Hatano, J. Kamiya, H. Kato, Y. Kitamura, Y. Maeda, C. L. Morris, H. Okamura, J. Rapaport, T. Saito, Y. Sakemi, K. Sekiguchi, Y. Shimizu, K. Suda, A. Tamii, N. Uchigashima, and T. Wakasa. Determination of the Gamow–Teller quenching factor from charge-exchange reactions on ^{90}Zr. *Phys. Lett. B*, 615(3):193–199, 2005.

[24] B. D. Anderson, A. R. Baldwin, P. Baumann, B. A. Brown, F. Didierjean, C. C. Foster, L. A. C. Garcia, A. Huck, A. Knipper, R. Madey, D. M. Manley, G. Marguier, M. Ramdhane, H. Ravn, C. Richard-Serre, G. Walter, and J. W. Watson. Gamow-Teller strength to ^{38}K from the ^{38}Ar(p,n) reaction and ^{38}Ca(β^+) decay. *Phys. Rev. C*, 54:602–612, 1996.

[25] R. G. T. Zegers, H. Abend, H. Akimune, A.M. Berg, D. Van, H. Fujimura, H. Fujita, Y. Fujita, M. Fujiwara, S. Gales, K. Hara, M. N. Harakeh, T. Ishikawa, T. Kawabata, K. Kawase, T. Mibe, K. Nakanishi, S. Nakayama, H. Toyokawa, M. Uchida, T. Yamagata, K. Yamasaki, and M. Yosoi. Excitation and decay of the isovector spin-flip giant monopole resonance via the ^{208}Pb (^{3}He,tp) reaction at 410 MeV. *Nuc. Phys. A*, 731:121–128, 2004.

[26] N. Auerbach and A. Klein. Structure of isovector spin excitations in nuclei. *Phys. Rev. C*, 30(3):1032, 1984.

[27] S. Fracasso and G. Colò. Fully self-consistent charge-exchange quasiparticle random-phase approximation and its application to isobaric analog resonances. *Phys. Rev. C*, 72:064310, 2005.

[28] N. Auerbach and A. Klein. Excitation of giant electric isovector resonances in pion charge-exchange reactions. *Phys. Rev. C*, 28:2075–2095, 1983.

[29] M. Scott, R. G. T. Zegers, R. Almus, Sam M. Austin, D. Bazin, B. A. Brown, C. Campbell, A. Gade, M. Bowry, S. Galès, U. Garg, M. N. Harakeh, E. Kwan, C. Langer, C. Loelius, S. Lipschutz, E. Litvinova, E. Lunderberg, C. Morse, S. Noji, G. Perdikakis, T. Redpath, C. Robin, H. Sakai, Y. Sasamoto, M. Sasano, C. Sullivan, J. A. Tostevin, T. Uesaka, and D. Weisshaar. Observation of the isovector giant monopole resonance via the ^{28}Si(^{10}Be,^{10} b*[1.74 MeV]) reaction at 100 aMeV. *Phys. Rev. Lett.*, 118:172501, 2017.

[30] J. D. Bowman, E. Lipparini, and S. Stringari. Isovector monopole excitation energies. *Phys. Lett. B*, 197(4):497–499, 1987.

[31] G. Colò, M. A. Nagarajan, P. Van Isacker, and A. Vitturi. Isospin mixing in proton-rich N=Z nuclei. *Phys. Rev. C*, 52:R1175–R1178, 1995.

[32] B. A. Brown. Neutron radii in nuclei and the neutron equation of state. *Phys. Rev. Lett*, 85(25):5296, 2000.

[33] B. G. Todd-Rutel and J. Piekarewicz. Neutron-rich nuclei and neutron stars: A new accurately calibrated interaction for the study of neutron-rich matter. *Phys. Rev. lett*, 95(12):122501, 2005.

[34] R. G. T. Zegers, A. M. van den Berg, S. Brandenburg, M. Fujiwara, J. Guillot, M. N. Harakeh, H. Laurent, S. Y. van der Werf, A. Willis, and H. W. Wilschut. Excitation of the isovector giant monopole resonances via the $^{\text{nat}}$Pb(^{3}He, tp) reaction. *Phys. Rev. C*, 63:034613, 2001.

[35] R. G. T. Zegers, H. Abend, H. Akimune, A. M. van den Berg, H. Fujimura, H. Fujita, Y. Fujita, M. Fujiwara, S. Galès, K. Hara, M. N. Harakeh, T. Ishikawa, T. Kawabata, K. Kawase, T. Mibe, K. Nakanishi, S. Nakayama, H. Toyokawa, M. Uchida, T. Yamagata, K. Yamasaki, and M. Yosoi. Excitation and decay of the isovector giant monopole resonances via the ^{208}Pb(^{3}He, tp) reaction at 410 MeV. *Phys. Rev. Lett.*, 90:202501, 2003.

[36] C. J. Guess, T. Adachi, H. Akimune, A. Algora, S. M. Austin, D. Bazin, B. A. Brown, C. Caesar, J. M. Deaven, H. Ejiri, et al. The ^{150}Nd(^{3}He, t) and ^{150}Sm(t,^{3}He) reactions with applications to β decay of ^{150}Nd. *arXiv preprint arXiv:1105.0677*, 2011.

[37] W. G. Love and M. A. Franey. Effective nucleon-nucleon interaction for scattering at intermediate energies. *Phys. Rev. C*, 24(3):1073, 1981.

[38] D. L. Prout, J. Rapaport, E. Sugarbaker, D. Cooper, S. Delucia, B. Luther, C. D. Goodman, B. K. Park, L. Rybarcyk, T. N. Taddeucci, and J. Ullmann. Observation of the spin isovector monopole resonance using the Pb($\vec{p}$, $\vec{n}$)Bi reaction at 795 MeV. *Phys. Rev. C*, 63:014603, 2000.

[39] J. Guillot, S. Galès, D. Beaumel, S. Fortier, E. Rich, N. Van Giai, G. Colò, A. M. van den Berg, S. Brandenburg, B. Davids, M. N. Harakeh, M. Hunyadi, M. de Huu, S. Y. van der Werf, H. J. Wörtche, C. Bäumer, D. Frekers, E.-W. Grewe, P. Haefner, B. C. Junk, and M. Fujiwara. The (t,^{3}He) reaction at 43 MeV/nucleon on ^{48}Ca and ^{58}Ni: Results and microscopic interpretation. *Phys. Rev. C*, 73:014616, 2006.

[40] K. Miki, H. Sakai, T. Uesaka, H. Baba, C. L. Bai, G. P. A. Berg, N. Fukuda, D. Kameda, T. Kawabata, S. Kawase, T. Kubo, S. Michimasa, H. Miya, S. Noji, T. Ohnishi, S. Ota, A. Saito, Y. Sasamoto, H. Sagawa, M. Sasano, S. Shimoura, H. Takeda, H. Tokieda, K. Yako, Y. Yanagisawa, and R. G. T. Zegers. Identification of the β^+ isovector spin monopole resonance via the ^{208}Pb and ^{90}Zr(t,^{3} He) reactions at 300 MeV/u. *Phys. Rev. Lett.*, 108:262503, 2012.

[41] M. A. Franey and W. G. Love. Nucleon-nucleon t-matrix interaction for scattering at intermediate energies. *Phys. Rev. C*, 31(2):488, 1985.

[42] A. Erell, J. Alster, J. Lichtenstadt, M. A. Moinester, J. D. Bowman, M.D Cooper, F. Irom, H. S. Matis, E. Piasetzky, and U. Sennhauser. Measurements on isovector giant resonances in pion charge-exchange. *Phys. Rev. C*, 34(5):1822, 1986.

[43] A. Erell, J. Alster, J. Lichtenstadt, M.A. Moinester, J.D. Bowman, M.D. Cooper, F. Irom, H.S. Matis, E. Piasetzky, U. Sennhauser, et al. Properties of the isovector monopole and other giant resonances in pion charge-exchange. *Phys. Rev. lett*, 52(24):2134, 1984.

[44] F. Irom, J. D. Bowman, G. O. Bolme, E. Piasetzky, U. Sennhauser, J. Alster, J. Lichtenstadt, M. Moinester, J. N. Knudson, S. H. Rokni, et al. Excitation of isovector giant resonances in pion single-charge-exchange at 120, 165, and 230 MeV. *Phys. Rev. C*, 34(6):2231, 1986.

[45] J. M. Eisenberg, A. Erell, and R. R. Silbar. Nucleon-nucleon force in a skyrmion model stabilized by omega exchange. *Phys. Rev. C*, 33(4):1531, 1986.

[46] S. Nakayama, H. Akimune, Y. Arimoto, I. Daito, H. Fujimura, Y. Fujita, M. Fujiwara, K. Fushimi, H. Kohri, N. Koori, K. Takahisa, T. Takeuchi, A. Tamii, M. Tanaka, T. Yamagata, Y. Yamamoto, K. Yonehara, and H. Yoshida. Isovector electric monopole resonance in ^{60}Ni. *Phys. Rev. Lett.*, 83:690–693, 1999.

[47] A. Krasznahorkay, M. Fujiwara, P. van Aarle, H. Akimune, I. Daito, H. Fujimura, Y. Fujita, M. N. Harakeh, T. Inomata, J. Jänecke, S. Nakayama, A. Tamii, M. Tanaka, H. Toyokawa, W. Uijen, and M. Yosoi. Excitation of isovector spin-dipole resonances and neutron skin of nuclei. *Phys. Rev. Lett.*, 82:3216–3219, 1999.

[48] K. Miki, R. G. T. Zegers, Sam M. Austin, D. Bazin, B. A. Brown, A. C. Dombos, R. K. Grzywacz, M. N. Harakeh, E. Kwan, S. N. Liddick, S. Lipschutz, E. Litvinova, M. Madurga,

M. T. Mustonen, W. J. Ong, S .V. Paulauskas, G. Perdikakis, J. Pereira, W. A. Peters, C. Robin, M. Scott, A. Spyrou, C. Sullivan, and R. Titus. Isovector excitations in ^{100}Nb and their decays by neutron emission studied via the ^{100}Mo(t,^{3}He+n) reaction at 115 MeV/u. *Phys. Lett. B*, 769:339–344, 2017.

[49] M. H. Urin. Direct-decay properties of giant resonances. *Nuc. Phys. A*, 811(1-2):107–126, 2008.

[50] S. Noji, H. Sakai, N. Aoi, H. Baba, G. P. A. Berg, P. Doornenbal, M. Dozono, N. Fukuda, N. Inabe, D. Kameda, T. Kawabata, S. Kawase, Y. Kikuchi, K. Kisamori, T. Kubo, Y. Maeda, H. Matsubara, S. Michimasa, K. Miki, H. Miya, H. Miyasako, S. Sakaguchi, Y. Sasamoto, S. Shimoura, M. Takaki, H. Takeda, S. Takeuchi, H. Tokieda, T. Ohnishi, S. Ota, T. Uesaka, H. Wang, K. Yako, Y. Yanagisawa, N. Yokota, K. Yoshida, and R. G. T. Zegers. Excitation of the isovector spin monopole resonance via the exothermic ^{90}Zr(^{12}N,^{12}C) reaction at 175 MeV/u. *Phys. Rev. Lett.*, 120:172501, 2018.

[51] M. Goldhaber and E. Teller. On nuclear dipole vibrations. *Phys. Rev.*, 74:1046–1049, 1948.

[52] T. Wakasa, H. Sakai, H. Okamura, H. Otsu, S. Fujita, S. Ishida, N. Sakamoto, T. Uesaka, Y. Satou, M. B. Greenfield, and K. Hatanaka. Gamow-teller strength of ^{90}Nb in the continuum studied via multipole decomposition analysis of the ^{90}Zr(p,n) reaction at 295 MeV. *Phys. Rev. C*, 55:2909–2922, 1997.

[53] A. Bohr and B.R. Mottelson. Nuclear structure. Vol 2 (W.A. Benjamin, inc., New York, 1975).

[54] J. Speth. Electric and magnetic giant resonances in nuclei. 7, 1991.

[55] D .H. Youngblood, H. L. Clark, and Y. W. Lui. Compressibility of nuclear matter from the giant monopole resonance. *Nuc. Phys. A*, 649(1-4):49–56, 1999.

[56] M. N Harakeh, K. Van der Borg, T. Ishimatsu, and H. P. Morsch. A. van der aloude and FE bertrand. *Phys. Rev. Lett*, 38:676, 1977.

[57] M. N. Harakeh, B B. Van Heyst, K. Van der Borg, and A. Van der Woude. Isoscalar excitations in the lead region observed in inelastic α-scattering at E (α) = 120 MeV. *Nuc. Phys. A*, 327(2):373–396, 1979.

[58] D. H. Youngblood, H. L. Clark, and Y. W. Lui. Incompressibility of nuclear matter from the giant monopole resonance. *Phys. Rev. lett*, 82(4):691, 1999.

[59] D. H. Youngblood, H. L. Clark, and Y. W. Lui. Incompressibility of nuclear matter from the giant monopole resonance. *Phys. Rev. lett*, 82(4):691, 1999.

[60] U. Garg and G. Colo. The compression-mode giant resonances and nuclear incompressibility. *Progress in Particle and Nuc. Phys.*, 101:55–95, 2018.

[61] M. J. Scott. *Search for the Isovector Giant Monopole Resonance via the* ^{28}Si(^{10}Be, ^{10}B + γ) *reaction at 100 MeV/u*. PhD thesis, Michigan State University, 2015.

[62] H. Steinwedel and J. H. D. Jensen. Hydrodynamik von kerndipolschwingungen. *Zeitschrift für Naturforschung A*, 5(8):413–420, 1950.

[63] B. L. Berman and S. C. Fultz. Measurements of the giant dipole resonance with monoenergetic photons. *Rev. Mod. Phys.*, 47:713–761, 1975.

[64] S. D. Bloom, N. K. Glendenning, and S. A. Moszkowski. Proton-neutron interaction and the (p, n) reaction in mirror nuclei. *Phys. Rev. lett*, 3(2):98, 1959.

[65] W. P. Alford and B. M. Spicer. Nucleon charge-exchange reactions at intermediate energy. *Advances in Nuc. Phys.*, pages 1–82, 2002.

[66] C. Gaarde, J. Rapaport, T. N. Taddeucci, C. D. Goodman, C. C. Foster, D. E. Bainum, C. A. Goulding, M. B. Greenfield, D. J. Hören, and E. Sugarbaker. Excitation of giant spin-isospin multipole vibrations. *Nuc. Phys. A*, 369(2):258–280, 1981.

[67] A. Brockstedt, I. Bergquist, L. Carlén, L. P. Ekström, B. Jakobsson, C. Ellegaard, C. Gaarde, J. S. Larsen, C. Goodman, M. Bedjidian, D. Contardo, J. Y. Grossiord, A. Guichard, J. R. Pizzi, D. Bachelier, J. L. Boyard, T. Hennino, J. C. Jourdain, M. Roy-Stephan, M. Boivin, T. Hasegawa, and P. Radvanyi. The (3he, t) reaction at intermediate energies: Spin-isospin multipole transitions. *Nuc. Phys. A*, 530(3):571–604, 1991.

[68] R. G. T. Zegers. *Excitation of Isovector Giant Resonance through charge-exchange reactions*. PhD thesis, University of Groningen, 2021.

[69] C. Scholl, Y. Fujita, T. Adachi, P. von Brentano, H. Fujita, M. Górska, H. Hashimoto, K. Hatanaka, H. Matsubara, K. Nakanishi, T. Ohta, Y. Sakemi, Y. Shimbara, Y. Shimizu, Y. Tameshige, A. Tamii, M. Yosoi, and R. G. T. Zegers. High-resolution study of the ^{9}Be(^{3}He,t)^{9}B reaction up to the ^{9}B triton threshold. *Phys. Rev. C*, 84:014308, 2011.

[70] C. A. Douma, C. Agodi, H. Akimune, M. Alanssari, F. Cappuzzello, D. Carbone, M. Cavallaro, G. Colo, F. Diel, H. Ejiri, et al. Gamow-Teller strength distributions of ^{116}Sb and ^{122}Sb using the (^{3}He,t) charge-exchange reaction Gamow-Teller strength distributions of ^{116}Sb and ^{112}Ni using the (^{3}He,t) charge-exchange reaction,2020. .

[71] Y. Fujita, T. Adachi, H. Akimune, A.D. Bacher, G. P. A. Berg, T. Black, I. Daito, C. C. Foster, H. Fujimura, H. Fujita, et al. Isospin symmetry-structure study at new high-resolution course of RCNP. *Nuc. Phys.. A, Nuclear and hadronic physics*, 687(1-2):311–320, 2001.

[72] Y. Fujita. Gamow-teller strengths from (^{3}He,t) charge-exchange reaction. In *Journal of Physics: Conference Series*, volume 49, page 007. IOP Publishing, 2006.

[73] Y. Kalmykov, T. Adachi, G. P. A. Berg, H. Fujita, K. Fujita, Y. Fujita, K. Hatanaka, J. Kamiya, K. Nakanishi, P. von Neumann-Cosel, V. Y. Ponomarev, A. Richter, N. Sakamoto, Y. Sakemi, A. Shevchenko, Y. Shimbara, Y. Shimizu, F. D. Smit, T. Wakasa, J. Wambach, and M. Yosoi. Fine structure of the gamow-teller resonance in ^{90}Nb and level density of 1^{+} states. *Phys. Rev. Lett.*, 96:012502, 2006.

[74] N. Auerbach, F. Osterfeld, and T. Udagawa. The spin isovector monopole strength and the (3he,t) reaction. *Phys. Lett. B*, 219(2):184–188, 1989.

[75] H. Ohnuma, K. Hatanaka, S. I. Hayakawa, M. Hosaka, T. Ichihara, S. Ishida, S. Kato, T. Niizeki, M. Ohura, H. Okamura, H. Orihara, H. Sakai, H. Shimizu, Y. Tajima, H. Toyokawa, H. Y. Yoshida, and M. Yosoi. (d,^{2}he) reactions at e_d=260 MeV as a possible probe to nuclear spin-isospin excitation. *Phys. Rev. C*, 47:648–651, 1993.

[76] H. Okamura, S. Fujita, Y. Hara, K. Hatanaka, T. Ichihara, S. Ishida, K. Katoh, T. Niizeki, H. Ohnuma, H. Otsu, H. Sakai, N. Sakamoto, Y. Satou, T. Uesaka, T. Wakasa, and T. Yamashita. Tensor analyzing power of the (d, 2he) reaction at 270 MeV. *Phys. Lett. B*, 345(1):1–5, 1995.

[77] H. M. Xu, G. K. Ajupova, A. C. Betker, C. A. Gagliardi, B. Kokenge, Y. W. Lui, and A. F. Zaruba. (d,^{2}He) reactions at Ed= 125.2 MeV. *Phys. Rev. C*, 52(3):R1161, 1995.

[78] S. Rakers, C. Bäumer, D. Frekers, R. Schmidt, A. M. van den Berg, V. M. Hannen, M. N. Harakeh, M. A. de Huu, H. J. Wörtche, D. De Frenne, M. Hagemann, J. Heyse, E. Jacobs, and Y. Fujita. Gamow-teller matrix elements from the ^{12}C(d,^{2}He) and ^{24}Mg(d,^{2}He) reactions at 170 MeV. *Phys. Rev. C*, 65:044323, 2002.

[79] S. Rakers, F. Ellinghaus, R. Bassini, C. Bäumer, A. M. van den Berg, D. Frekers, D. De Frenne, M. Hagemann, V. M Hannen, M. N Harakeh, M. Hartig, R. Henderson, J. Heyse, M. A de Huu, E. Jacobs, M. Mielke, J. M. Schippers, R. Schmidt, S. Y. van der Werf, and H. J. Wörtche. Measuring the (d,^{2}He) reaction with the focal-plane detection system of the BBS magnetic spectrometer at AGOR. *Nuclear Instruments and Methods in Physics Research Section A: Accelerators, Spectrometers, Detectors and Associated Equipment*, 481(1):253–261, 2002.

[80] H. Ueno, Y. Fujita, H. Fujita, T. Shinada, Y. Kanzaki, M. Yosoi, A. Tamii, K. Takahisa, F. Ihara, H. Kohri, T. Yamagata, and K. Katori. (^{6}Li,^{6}He) reaction at 100 MeV/u as a probe of spin-excitation strengths. *Phys. Lett. B*, 465(1):67–73, 1999.

[81] H. Laurent, S. Galès, D. Beaumel, G. M. Crawley, J. E Finck, S. Fortier, J. M. Maison, C. P. Massolo, D. J. Mercer, J. S. Winfield, and G. H. Yoo. Spin-isospin multipole excitations by means of the (^{6}Li,^{6}He) reaction at 100 A.MeV. *Nuc. Phys. A*, 569(1):297–302, 1994.

[82] T. Annakkage, J. Jänecke, J. S. Winfield, G. P. A. Berg, J. A. Brown, G. Crawley, S. Danczyk, M. Fujiwara, D. J. Mercer, K. Pham, D. A. Roberts, J. Stasko, and G. H. Yoo. Isovector giant resonances in ^{6}He, ^{12}B, ^{90}Y, ^{120}In, and ^{208}T observed in the (^{7}Li,^{7}Be) charge-exchange reaction. *Nuc. Phys. A*, 648(1):3–44, 1999.

[83] J. S. Winfield, D. Beaumel, S. Galès, H. Laurent, I. Lhenry, J. M. Maison, G. M. Crawley, S. Danczyk, S. E. Hirzebruch, J. C. Staszko, and T. Suomijärvi. The (^{7}Li,^{7}Beγ) reaction and isovector spin strength in ^{40}Ca. *Phys. Rev. C*, 54:125–131, 1996.

[84] S. Nakayama, H. Akimune, I. Daito, H. Fujimura, Y. Fujita, M. Fujiwara, K. Fushimi, T. Inomata, K. Ishibashi, H. Kohri, N. Koori, K. Takahisa, A. Tamii, M. Tanaka, H. Toyokawa,

and T. Yamagata. Gamow-teller transitions in the (^{7}Li, ^{7}Be) reaction at 65AMeV. *Phys. Rev. C*, 60:047303, 1999.

[85] N. Anantaraman, J. S. Winfield, Sam M. Austin, J. A. Carr, C. Djalali, A. Gillibert, W. Mittig, J. A. Nolen, and Z. W. Long. (^{12}C,^{12}B) and (^{12}C,^{12}N) reactions at E/A=70 MeV as spin probes: Calibration and application to 1^{+} states in ^{56}Mn. *Phys. Rev. C*, 44:398–414, 1991.

[86] T. Ichihara, M. Ishihara, H. Ohnuma, T. Niizeki, Y. Tajima, T. Yamamoto, Y. Fuchi, S. Kubono, M. H. Tanaka, H. Okamura, S. Ishida, S. Miyamoto, and H. Toyokawa. Charge-exchange reaction ^{12}C(^{12}C,^{12}N)^{12}B at EA = 135 MeV. *Phys. Lett. B*, 323(3):278–283, 1994.

[87] H. G. Bohlen, B. Gebauer, D. Kolbert, S. Kubono, W. von Oertzen, P. O. Pellegrin, E. Stiliaris, M. Wllpert, T. Wilpert, H. Lenske, H. H. Wolter, A. Miczaika, N. Alamanos, J. Barrette, B. Berthier, B. Fernandez, J. Gastebois, C. Berat, M. Buenerd, J. Y. Hostachy, Ph. Martin, and W. Mittig. The mechanism of the (^{12}C,^{12}N) charge-exchange reaction on ^{12}C between 30 and 100 MeV/u. *Nuc. Phys. A*, 488:89–94, 1988.

[88] T. Ichihara, M. Ishihara, H. Ohnuma, T. Niizeki, T. Yamamoto, K. Katoh, T. Yamashita, Y. Fuchi, S. Kubono, M. H. Tanaka, H. Okamura, S. Ishida, and T. Uesaka. Excitation of spin-dipole states by the ^{12}C(^{12}C,^{12}N)^{12}B reaction at E/A = 135 MeV. *Nuc. Phys. A*, 577(1):93–98, 1994. Proceeding of the International Symposium on Spin-Isospin Responses and Weak Processes in Hadrons and Nuclei.

[89] T. Ichihara, M. Ishihara, H. Ohnuma, T. Niizeki, Y. Satou, H. Okamura, S. Kubono, M. H. Tanaka, and Y. Fuchi. Isovector quadrupole resonance observed in the ^{60}Ni(^{13}C,^{13} N)^{60}Co reaction at E/A=100 MeV. *Phys. Rev. Lett.*, 89:142501, 2002.

[90] C. Bérat, M. Buénerd, J. Y. Hostachy, P. Martin, J. Barrette, B. Berthier, B. Fernandez, A. Miczaïka, A. Villari, H. G. Bohlen, S. Kubono, E. Stiliaris, and W. von Oertzen. Electric isovector nuclear response from ^{13}C induced charge-exchange reactions. *Nuc. Phys. A*, 555(2):455–476, 1993.

[91] M. D. Cooper, H. W. Baer, R. Bolton, J. D. Bowman, F. Cverna, N. S. P. King, M. Leitch, J. Alster, A. Doron, A. Erell, et al. Angular distribution for ^{15}N(π+, π 0)^{15}O (gs) at T π= 48 MeV. *Phys. Rev. lett*, 52(13):1100, 1984.

[92] T. Uesaka, H. Matsubara, K. Miki, S. Noji, H. Sakai, Y. Sasamoto, S. Shimoura, M. Takaki, and K. Yako. New experimental studies of nuclear spin-isospin responses. *Progress of Theoretical Physics Supplement*, 196:150–157, 2012.

[93] T. Uesaka, S. Shimoura, and H. Sakai. The sharaq spectrometer. *Progress of Theoretical and Experimental Physics*, 2012(1), 2012.

[94] Y. Satou, T. Nakamura, Y. Kondo, N. Matsui, Y. Hashimoto, T. Nakabayashi, T. Okumura, M. Shinohara, N. Fukuda, T. Sugimoto, H. Otsu, Y. Togano, T. Motobayashi, H. Sakurai, Y. Yanagisawa, N. Aoi, S. Takeuchi, T. Gomi, M. Ishihara, S. Kawai, H.J. Ong, T. K. Onishi, S. Shimoura, M. Tamaki, T. Kobayashi, Y. Matsuda, N. Endo, and M. Kitayama. ^{14}Be(p,n)^{14}B reaction at 69 MeV in inverse kinematics. *Phys. Lett. B*, 697(5):459–462, 2011.

[95] T. Teranishi, S. Shimoura, Y. Ando, M. Hirai, N. Iwasa, T. Kikuchi, S. Moriya, T. Motobayashi, H. Murakami, T. Nakamura, T. Nishio, H. Sakurai, T. Uchibori, Y. Watanabe, Y. Yanagisawa, and M. Ishihara. Isobaric analog state of ^{11}Li. *Phys. Lett. B*, 407(2):110–114, 1997.

[96] Z. Li, W. Liu, X. Bai, Y. Wang, G. Lian, Z. Li, and S. Zeng. First observation of neutron–proton halo structure for the 3.563 MeV 0^+ state in ^{6}Li via ^{1}H(^{6}He,^{6}Li)n reaction. *Phys. Lett. B*, 527(1):50–54, 2002.

[97] M. D. Cortina-Gil, P. Roussel-Chomaz, N. Alamanos, J. Barrette, W. Mittig, F. Auger, Y. Blumenfeld, J. M. Casandjian, M. Chartier, V. Fekou-Youmbi, B. Fernandez, N. Frascaria, A. Gillibert, H. Laurent, A. Lépine-Szily, N. A. Orr, V. Pascalon, J. A. Scarpaci, J. L. Sida, and T. Suomijärvi. Search for the signature of a halo structure in the p(^{6}He,^{6}Li)n reaction. *Phys. Lett. B*, 371(1):14–18, 1996.

[98] M. D. Cortina-Gil, A. Pakou, N. Alamanos, W. Mittig, P. Roussel-Chomaz, F. Auger, J. Barrette, Y. Blumenfeld, J. M. Casandjian, M. Chartier, F. Dietrich, V. Fekou-Youmbi, B. Fernandez, N. Frascaria, A. Gillibert, H. Laurent, A. Lepine-Szily, N. Orr, V. Pascalon, J. A. Scarpaci, J. L. Sida, and T. Suomijarvi. Charge-exchange reaction induced by ^{6}He and nuclear densities. *Nuc. Phys. A*, 641(3):263–270, 1998.

[99] J. A. Brown, D. Bazin, W. Benenson, J. Caggiano, M. Fauerbach, M. Hellström, J. H. Kelley, R. A. Kryger, R. Pfaff, B. M. Sherrill, M. Steiner, D. J. Morrissey, and C. F. Powell. Measurement of the ^{1}H(^{6}He,^{6} Li)n reaction in inverse kinematics. *Phys. Rev. C*, 54:R2105–R2108, 1996.

[100] S. Shimoura, T. Teranishi, Y. Ando, M. Hirai, N. Iwasa, T. Kikuchi, S. Moriya, T. Motobayashi, T. Murakami, T. Nakamura, T. Nishio, H. Sakurai, T. Uchibori, Y. Wabanabe, Y. Yanagisawa, and M. Ishihara. charge-exchange reaction of the neutron-halo nucleus ^{11}Li. *Nuc. Phys. A*, 616(1):208–214, 1997. Radioactive Nuclear Beams.

[101] S. Shimoura, T. Teranishi, Y. Ando, M. Hirai, N. Iwasa, T. Kikuchi, S. Moriya, T. Motobayashi, T. Murakami, T. Nakamura, T. Nishio, H. Sakurai, T. Uchibori, Y. Wabanabe, Y. Yanagisawa, and M. Ishihara. Isobaric analog state of ^{11}Li. *Nuc. Phys. A*, 630(1):387–393, 1998. Nucleus-Nucleus Collisions.

[102] G. Perdikakis, Sam M. Austin, D. Bazin, C. Caesar, J. M. Deaven, C. J. Guess, G. W. Hitt, R. T. Meharchand, D. T. Nguyen, Y. Shimbara, K. Thorne, and R. G. T. Zegers. Lenda: A low energy neutron detector array for studies of (p, n) reactions with radioactive beams. *IEEE Transactions on Nuclear Science*, 56(3):1174–1178, 2009.

[103] M. Sasano, G. Perdikakis, R. G. T. Zegers, Sam M. Austin, D. Bazin, B. A. Brown, C. Caesar, A. L. Cole, J. M. Deaven, N. Ferrante, C. J. Guess, G. W. Hitt, R. Meharchand, F. Montes, J. Palardy, A. Prinke, L. A. Riley, H. Sakai, M. Scott, A. Stolz, L. Valdez, and K. Yako. Gamow-teller transition strengths from ^{56}Ni. *Phys. Rev. Lett.*, 107:202501, 2011.

[104] J. Yasuda, M. Sasano, R. G. T. Zegers, H. Baba, D. Bazin, W. Chao, M. Dozono, N. Fukuda, N. Inabe, T. Isobe, G. Jhang, D. Kameda, M. Kaneko, K. Kisamori, M. Kobayashi,

N. Kobayashi, T. Kobayashi, S. Koyama, Y. Kondo, A. J. Krasznahorkay, T. Kubo, Y. Kubota, M. Kurata-Nishimura, C. S. Lee, J. W. Lee, Y. Matsuda, E. Milman, S. Michimasa, T. Motobayashi, D. Muecher, T. Murakami, T. Nakamura, N. Nakatsuka, S. Ota, H. Otsu, V. Panin, W. Powell, S. Reichert, S. Sakaguchi, H. Sakai, M. Sako, H. Sato, Y. Shimizu, M. Shikata, S. Shimoura, L. Stuhl, T. Sumikama, H. Suzuki, S. Tangwancharoen, M. Takaki, H. Takeda, T. Tako, Y. Togano, H. Tokieda, J. Tsubota, T. Uesaka, T. Wakasa, K. Yako, K. Yoneda, and J. Zenihiro. Extraction of the Landau-Migdal Parameter from the Gamow-Teller Giant Resonance in ^{132}Sn. *Phys. Rev. Lett.*, 121:132501, 2018.

[105] S. I. Lipschutz. *The (p, n) charge-exchange reaction in inverse kinematics as a probe for isovector giant resonances in exotic nuclei*. PhD thesis, Michigan State University, 2018.

[106] R. G. T. Zegers, R. Meharchand, Y. Shimbara, Sam M. Austin, D. Bazin, B. A. Brown, C. Aa. Diget, A. Gade, C. J. Guess, M. Hausmann, G. W. Hitt, M. E. Howard, M. King, D. Miller, S. Noji, A. Signoracci, K. Starosta, C. Tur, C. Vaman, P. Voss, D. Weisshaar, and J. Yurkon. ^{34}P(^{7}Li,^{7}Be+γ) Reaction at 100A MeV in inverse kinematics. *Phys. Rev. Lett.*, 104:212504, 2010.

[107] R. Meharchand, S.M. Austin, T. Baugher, D. Bazin, B. A. Brown, J. Deaven, A. Gade, G. F. Grinyer, C. J. Guess, H. Iwasaki, S. McDaniel, K. Meierbachtol, G. Perdikakis, J. Pereira, A. M. Prinke, A. Ratkiewicz, A. J. Signoracci, S. Stroberg, L. Uher, P. Voss, K. A. Walsh, D. Weisshaar, R. Winkler, R. G. T. Zegers, and M. E. Howard. Spectroscopy of ^{12}Be using the (^{7}Li, ^{7}Be) reaction in inverse kinematics. In *APS Division of Nuc. Phys. Meeting Abstracts*, APS Meeting Abstracts, page MG.004, 2010.

[108] S. Giraud, J. Zamora, M. Denudt, R.G.T. Zegers, D. Bazin, Y. Ayyad, S. Beceiro-Novo, J. Chen, M. Cortesi, C. Maher, W. Mittig, F. Ndayisabye, S. Noji, J. Pereira, Z. Rahman, J. Schmitt, M. Serikow, J. Surbrook, L. Sun, N. Watwood, and T. Wheeler. Constraining the electron-capture rates of neutron rich nuclei with (d,^{2}He) reaction in inverse kinematics. In *APS Division of Nuc. Phys. Meeting Abstracts*, volume 2021 of *APS Meeting Abstracts*, page PD.002, 2021.

[109] Y. Ayyad, N. Abgrall, T. Ahn, H. Álvarez Pol, D. Bazin, S. Beceiro-Novo, L. Carpenter, R. J. Cooper, M. Cortesi, A. O. Macchiavelli, W. Mittig, B. Olaizola, J. S. Randhawa, C. Santamaria, N. Watwood, J. C. Zamora, and R. G. T. Zegers. Next-generation experiments with the active target time projection chamber (AT-TPC). *Nuclear Instruments and Methods in Physics Research Section A: Accelerators, Spectrometers, Detectors and Associated Equipment*, 954:161341, 2020. Symposium on Radiation Measurements and Applications XVII.

[110] F. Ndayisabye. *Thesis, Software Tool for Performing the Calibration of the AT-TPC Electronics Channels*. Michigan State University, 2019.

[111] J. Cook, J. Carr, Computer program FOLD Florida State University (unpublished) based on F. Petrovich, D. Stanley., S. Fracasso, and G. Colo modified as described in J. Cook et al. . *and Phys. Rev. C 30, 1538 (1984)*, and R. G. T. Zegers (2005) unpublished.

[112] B. Bonin, N. Alamanos, B. Berthier, G. Bruge, H. Faraggi, D. Legrand, J.C. Lugol, W. Mittig, L. Papineau, A.I. Yavin, D.K. Scott, M. Levine, J. Arvieux, L. Farvacque, and M. Buenerd. Response functions of ^{58}Ni, ^{116}Sn and ^{208}Pb to the excitation of intermediate-energy α-particles. *Nuc. Phys. A*, 430(2):349–396, 1984.

[113] T. Wakasa, H. Sakai, H. Okamura, H. Otsu, S. Fujita, S. Ishida, N. Sakamoto, T. Uesaka, Y. Satou, M. B. Greenfield, and K. Hatanaka. Gamow-Teller strength of ^{90}Nb in the continuum studied via multipole decomposition analysis of the ^{90}Zr(p,n) reaction at 295 MeV. *Phys. Rev. C*, 55:2909–2922, 1997.

[114] F. Petrovich and D. Stanley. Microscopic interpretation of ^{7}Li + ^{24}Mg inelastic scattering at 34 MeV. *Nuc. Phys. A*, 275(2):487–508, 1977.

[115] S. Y. van der Werf. Normod. . .

[116] V. A. Madsen. A formalism for direct inelastic scattering and charge-exchange. *Nuc. Phys.*, 80(1):177–197, 1966.

[117] B. A. Brown and W. D. M. Rae. The Shell-Model code Nushellx@msu. *Nuclear Data Sheets*, 120:115–118, 2014.

[118] B. Alex Brown. New skyrme interaction for normal and exotic nuclei. *Phys. Rev. C*, 58:220–231, 1998.

[119] J. Kamiya, K. Hatanaka, T. Adachi, K. Fujita, K. Hara, T. Kawabata, T. Noro, H. Sakaguchi, N. Sakamoto, Y. Sakemi, Y. Shimbara, Y. Shimizu, S. Terashima, M. Uchida, T. Wakasa, Y. Yasuda, H.P. Yoshida, and M. Yosoi. Cross section and induced polarization in ^{3}He elastic scattering at 443 MeV. *Phys. Rev. C*, 67:064612, 2003.

[120] S. C. Pieper, R. B. Wiringa, Annu. Rev. Nucl. Part. Sci.51, 53, (2001), and R. B. Wiring. *private communication*. .

[121] D. Ackermann, F. Scarlassara, P. Bednarczyk, S. Beghini, L. Corradi, G. Montagnoli, L. Miiller, D. R. Napoli, K. M. Petrache, F. Soramel, et al. . *Nuc. Phys. A*, 590:841–926, 1995.

[122] S. Y. van der Werf, S. Brandenburg, P. Grasdijk, W. A. Sterrenburg, M. N. Harakeh, M. B. Greenfield, B. A. Brown, and M. Fujiwara. The effective ^{3}He-nucleon force in a microscopic dwba approach to the (^{3}He, t) charge-exchange reaction. *Nucl. Phys. A;(Netherlands)*, 496(2), 1989.

[123] T. N. Taddeucci, C. A. Goulding, T. A. Carey, R. C. Byrd, C. D. Goodman, C. Gaarde, J. Larsen, D. Horen, J. Rapaport, and E. Sugarbaker. The (p, n) reaction as a probe of beta decay strength. *Nuc. Phys. A*, 469(1):125–172, 1987.

[124] I. J. Thompson and F. M. Nunes. *Nuclear reactions for astrophysics: principles, calculation and applications of low-energy reactions*. Cambridge University Press, 2009.

[125] H. Akimune, I. Daito, Y. Fujita, M. Fujiwara, M. B. Greenfield, M.N. Harakeh, T. Inomata, J. Jänecke, K. Katori, S. Nakayama, H. Sakai, Y. Sakemi, M. Tanaka, and M. Yosoi. (^{3}He,t) charge-exchange reactions at E(^{3}He) = 450 MeV, = 0°. *Nuc. Phys. A*, 569(1):245–254, 1994.

[126] C. J. Guess. *The* ^{150}Sm*(t,*^{3}He*)*^{150}Pm *and* ^{150}Nd*(*^{3}He*,t)*^{150}Pm *reactions and applications for 2ν and 0ν double beta decay*. PhD thesis, Michigan State University, 2010.

[127] D. Frekers, H. Ejiri, H. Akimune, T. Adachi, B. Bilgier, B.A. Brown, B.T. Cleveland, H. Fujita, Y. Fujita, M. Fujiwara, E. Ganioğlu, V.N. Gavrin, E.-W. Grewe, C.J. Guess, M.N. Harakeh, K. Hatanaka, R. Hodak, M. Holl, C. Iwamoto, N.T. Khai, H.C. Kozer, A. Lennarz, A. Okamoto, H. Okamura, P.P. Povinec, P. Puppe, F. Šimkovic, G. Susoy, T. Suzuki, A. Tamii, J.H. Thies, J. Van de Walle, and R.G.T. Zegers. The ^{71}Ga(^{3}He,t) reaction and the low-energy neutrino response. *Phys. Lett. B*, 706(2):134–138, 2011.

[128] T Wakasa, K Hatanaka, Y Fujita, G.P.A Berg, H Fujimura, H Fujita, M Itoh, J Kamiya, T Kawabata, K Nagayama, T Noro, H Sakaguchi, Y Shimbara, H Takeda, K Tamura, H Ueno, M Uchida, M Uraki, and M Yosoi. High resolution beam line for the grand raiden spectrometer. *Nuclear Instruments and Methods in Physics Research Section A: Accelerators, Spectrometers, Detectors and Associated Equipment*, 482(1):79–93, 2002.

[129] M Fujiwara, H Akimune, I Daito, H Fujimura, Y Fujita, K Hatanaka, H Ikegami, I Katayama, K Nagayama, N Matsuoka, S Morinobu, T Noro, M Yoshimura, H Sakaguchi, Y Sakemi, A Tamii, and M Yosoi. Magnetic spectrometer grand raiden. *Nuclear Instruments and Methods in Physics Research Section A: Accelerators, Spectrometers, Detectors and Associated Equipment*, 422(1):484–488, 1999.

[130] Y. Fujita, K. Hatanaka, G.P.A. Berg, K. Hosono, N. Matsuoka, S. Morinobu, T. Noro, M. Sato, K. Tamura, and H. Ueno. Matching of a beam line and a spectrometer new beam line project at rcnp. *Nuclear Instruments and Methods in Physics Research Section B: Beam Interactions with Materials and Atoms*, 126(1):274–278, 1997. International Conference on Electromagnetic Isotope Separators and Techniques Related to Their Applications.

[131] Y. Shimbara. *High resolution study of Gamow-Teller transitions by* ^{37}Cl(^{3}He,t)^{37}Ar *reaction*. PhD thesis, Osaka University, 2005.

[132] K. Dennis, H. Akimune, G. P. A. Berg, S. Chang, B. Davis, M. Fujiwara, M. N. Harakeh, J. Jänecke, J. Liu, K. Pham, D. A. Roberts, and E. J. Stephenson. Atomic charge-exchange between fast helium ions and targets from carbon to bismuth at β=0.36. *Phys. Rev. A*, 50:3992–3999, 1994.

[133] A. L. Cole, H. Akimune, Sam M. Austin, D. Bazin, A. M. Van den Berg, G. P. A. Berg, J. Brown, I. Daito, Y. Fujita, M. Fujiwara, S. Gupta, K. Hara, M. N. Harakeh, J. Jänecke, T. Kawabata, T. Nakamura, D. A. Roberts, B. M. Sherrill, M. Steiner, H. Ueno, and R. G. T. Zegers. Measurement of the Gamow-Teller strength distribution in ^{58}Co via the ^{58}Ni(t,^{3}He) reaction at 115 MeV/nucleon. *Phys. Rev. C*, 74:034333, 2006.

[134] C. A. Douma, N. Kalantar-Nayestanaki, M. N. Harakeh, H. Akimune, H. Ejiri, D. Frekers, T. Agodi, M. Alanssari, D. Carbono, M. Cavallaro, et al. Gamow–teller strength distributions

of 116 sb and 122 sb using the (3 he, t) charge-exchange reaction. *The European Physical Journal A*, 56(2):51, 2020.

[135] K. Nakanishi. Isovector spin resonances in ^{90}Nb studied via the ^{90}Zr(^{3}He3, t+p) reaction. 2006.

[136] G. Perdikakis, R. G. T. Zegers, Sam M. Austin, D. Bazin, C. Caesar, J. M. Deaven, A. Gade, D. Galaviz, G. F. Grinyer, C. J. Guess, C. Herlitzius, G. W. Hitt, M. E. Howard, R. Meharchand, S. Noji, H. Sakai, Y. Shimbara, E. E. Smith, and C. Tur. Gamow-teller unit cross sections for (t,^{3}He) and (^{3}He, t) reactions. *Phys. Rev. C*, 83:054614, 2011.

[137] M. Horoi, B. A. Brown, T. Otsuka, M. Honma, and T. Mizusaki. Shell model analysis of the ^{56}Ni spectrum in the full *pf* model space. *Phys. Rev. C*, 73:061305, 2006.

[138] A. L. Cole, T. S. Anderson, R. G. T. Zegers, Sam M. Austin, B. A. Brown, L. Valdez, S. Gupta, G. W. Hitt, and O. Fawwaz. Gamow-teller strengths and electron-capture rates for pf-shell nuclei of relevance for late stellar evolution. *Phys. Rev. C*, 86:015809, 2012.

[139] N. Anantaraman, Sam M. Austin, B. A. Brown, G. M. Crawley, A. Galonsky, R. G. T. Zegers, B. D. Anderson, A. R. Baldwin, B. S. Flanders, R. Madey, J. W. Watson, and C. C. Foster. Electron capture strength for ^{60,62}Ni and ^{58,60,62,64}Ni(p, n)^{58,60,62,64}Cu reactions at 134.3 MeV. *Phys. Rev. C*, 78:065803, 2008.

[140] C. Djalali, N. Marty, M. Morlet, A. Willis, J.C. Jourdain, N. Anantaraman, G.M. Crawley, A. Galonsky, and P. Kitching. Systematics of the excitation of m1 resonances in medium heavy nuclei by 200 MeV proton inelastic scattering. *Nuc. Phys. A*, 388(1):1–18, 1982.

[141] R. A. Lindgren, W. L. Bendel, E. C. Jones, L. W. Fagg, X. K. Maruyama, J. W. Lightbody, and S. P. Fivozinsky. Electroexcitation of the T_0 + 1 giant M1 resonance in ^{58,60}Ni. *Phys. Rev. C*, 14:1789–1799, 1976.

[142] E. H. L. Aarts, R. K. Bhowmik, R. J. De Meijer, and S. Y. van der Werf. The continuum part of (^{3}He,t) spectra at E(^{3}He) = 52 MeV. *Phys. Lett. B*, 102(5):307–311, 1981.

[143] O. Bousshid, H. Machner, C. Alderliesten, U. Bechstedt, A. Djaloeis, P. Jahn, and C. Mayer-Böricke. Gross structure in triton spectra from ^{3}He-induced reactions. *Phys. Rev. Lett.*, 45:980–982, 1980.

[144] S. Gopal, A. Djaloeis, J. Bojowald, O. Bousshid, W. Oelert, N. G. Puttaswamy, P. Turek, and C. Mayer-Böricke. Broad structure in t spectra from (^{3}He,t) reactions at E(^{3}He)=130 MeV: Its angle and target-mass dependence. *Phys. Rev. C*, 23:2459–2462, 1981.

[145] J. Jänecke, K. Pham, D. A. Roberts, D. Stewart, M. N. Harakeh, G. P. A. Berg, C. C. Foster, J. E. Lisantti, R. Sawafta, E. J. Stephenson, A. M. van den Berg, S. Y. van der Werf, S. E. Muraviev, and M. H. Urin. Fragmentation of gamow-teller strength observed in ^{117,120}Sn(^{3}He,t)^{117,120}Sb charge-exchange reactions. *Phys. Rev. C*, 48:2828–2839, 1993.

[146] I. Bergqvist, A. Brockstedt, L. Carlén, L.P. Ekström, B. Jakobsson, C. Ellegaard, C. Gaarde, J. S. Larsen, C. Goodman, M. Bedjidian, D. Contardo, J. Y. Grossiord, A. Guichard, R. Haroutunian, J. R. Pizzi, D. Bachelier, J. L. Boyard, T. Hennino, J. C. Jourdain, M. Roy-Stephan, M. Boivin, and P. Radvanyi. The (^{3}He,t) reaction at intermediate energies: Spin-isospin transitions to states in ^{12}N and ^{13}N. *Nuc. Phys. A*, 469(4):648–668, 1987.

[147] D. L. Prout, C. Zafiratos, T. N. Taddeucci, J. Ullmann, R. C. Byrd, T. A. Carey, P. Lisowski, J. B. McClelland, L. J. Rybarcyk, W. Sailor, W. Amian, M. Braunstein, D. Lind, D. J. Mercer, D. Cooper, S. DeLucia, B. Luther, D. G. Marchlenski, E. Sugarbaker, J. Rapaport, B. K. Park, E. Gülmez, C. A. Whitten, C. D. Goodman, W. Huang, D. Ciskowski, and W. P. Alford. Cross sections and analyzing powers for quasielastic scattering at 795 and 495 MeV using the (p→,n) reaction. *Phys. Rev. C*, 52:228–242, 1995.

[148] K. Pham, J. Jänecke, D. A. Roberts, M. N. Harakeh, G. P. A. Berg, S. Chang, J. Liu, E. J. Stephenson, B. F. Davis, H. Akimune, and M. Fujiwara. Fragmentation and splitting of gamow-teller resonances in Sn(^{3}He,t)Sb charge-exchange reactions, A=112–124. *Phys. Rev. C*, 51:526–540, 1995.

[149] H. Akimune, I. Daito, Y. Fujita, M. Fujiwara, M. B. Greenfield, M. N. Harakeh, T. Inomata, J. Jänecke, K. Katori, S. Nakayama, H. Sakai, Y. Sakemi, M. Tanaka, and M. Yosoi. Direct proton decay from the gamow-teller resonance in ^{208}Bi. *Phys. Rev. C*, 52:604–615, 1995.

APPENDIX A

FULL INPUT FILE IN THE WSAW CODE

Table A.1 The file with full input parameters in WSAW input program for ^{60}Ni(^{3}He,t) reaction as described in Table 3.1.

```
0.1  20.   1  150   0
Ni60Cu60
59.   28.  60.   .65   1.25   1.25   7.0
1.0   1.   1.    2.    1.     1.5    .5
59.   28.  60.   .65   1.25   1.25   7.0
1.0   1.   1.    2.    1.     0.5    .5
59.   28.  60.   .65   1.25   1.25   7.0
1.0   1.   3.    1.    1.     3.5    .5
59.   28.  60.   .65   1.25   1.25   7.0
1.0   1.   3.    1.    1.     2.5    .5
59.   28.  60.   .65   1.25   1.25   7.0
1.0   1.   5.    0.    1.     4.5    .5
59.   28.  60.   .65   1.25   1.25   7.0
1.0   1.   5.    0.    1.     5.5    .5
59.   28.  60.   .65   1.25   1.25   7.0
1.0   1.   0.    2.    1.     0.5    .5
59.   28.  60.   .65   1.25   1.25   7.0
1.0   1.   2.    1.    1.     1.5    .5
59.   28.  60.   .65   1.25   1.25   7.0
1.0   1.   2.    1.    1.     2.5    .5
59.   28.  60.   .65   1.25   1.25   7.0
1.0   1.   4.    0.    1.     3.5    .5
59.   28.  60.   .65   1.25   1.25   7.0
1.0   1.   4.    0.    1.     4.5    .5
59.   28.  60.   .65   1.25   1.25   7.0
2.9   1.   1.    1.    1.     0.5    .5
59.   28.  60.   .65   1.25   1.25   7.0
4.8   1.   1.    1.    1.     1.5    .5
59.   28.  60.   .65   1.25   1.25   7.0
1.9   1.   3.    0.    1.     2.5    .5
```

Table A.2 The file with full input parameters in WSAW input program continuation.

```
59.   28.  60.   .65   1.25   1.25   7.0
8.6   1.   3.    0.    1.     3.5    .5
59.   28.  60.   .65   1.25   1.25   7.0
14.7  1.   0.    1.    1.     0.5    .5
59.   28.  60.   .65   1.25   1.25   7.0
13.4  1.   2.    0.    1.     1.5    .5
59.   28.  60.   .65   1.25   1.25   7.0
17.9  1.   2.    0.    1.     2.5    .5
59.   28.  60.   .65   1.25   1.25   7.0
24.7  1.   1.    0.    1.     0.5    .5
59.   28.  60.   .65   1.25   1.25   7.0
26.8  1.   1.    0.    1.     1.5    .5
59.   28.  60.   .65   1.25   1.25   7.0
35.4  1.   0.    0.    1.     0.5    .5
59.   28.  60.   .65   1.25   1.25   7.0
1.0   1.   1.    2.    0.     1.5    .5
59.   28.  60.   .65   1.25   1.25   7.0
1.0   1.   1.    2.    0.     0.5    .5
59.   28.  60.   .65   1.25   1.25   7.0
1.0   1.   3.    1.    0.     3.5    .5
59.   28.  60.   .65   1.25   1.25   7.0
1.0   1.   3.    1.    0.     2.5    .5
59.   28.  60.   .65   1.25   1.25   7.0
3.0   1.   5.    0.    0.     4.5    .5
59.   28.  60.   .65   1.25   1.25   7.0
3.0   1.   5.    0.    0.     5.5    .5
59.   28.  60.   .65   1.25   1.25   7.0
1.0   1.   0.    2.    0.     0.5    .5
59.   28.  60.   .65   1.25   1.25   7.0
1.0   1.   2.    1.    0.     1.5    .5
59.   28.  60.   .65   1.25   1.25   7.0
1.0   1.   2.    1.    0.     2.5    .5
59.   28.  60.   .65   1.25   1.25   7.0
1.0   1.   4.    0.    0.     3.5    .5
59.   28.  60.   .65   1.25   1.25   7.0
5.4   1.   4.    0.    0.     4.5    .5
```

Table A.3 The file with full input parameters in WSAW input program continuation.

```
59.   28.  60.   .65   1.25   1.25   7.0
8.3   1.   1.    1.    0.     0.5    .5
59.   28.  60.   .65   1.25   1.25   7.0
10.2  1.   1.    1.    0.     1.5    .5
59.   28.  60.   .65   1.25   1.25   7.0
8.7   1.   3.    0.    0.     2.5    .5
59.   28.  60.   .65   1.25   1.25   7.0
15.4  1.   3.    0.    0.     3.5    .5
59.   28.  60.   .65   1.25   1.25   7.0
20.   1.   0.    1.    0.     0.5    .5
59.   28.  60.   .65   1.25   1.25   7.0
20.1  1.   2.    0.    0.     1.5    .5
59.   28.  60.   .65   1.25   1.25   7.0
24.6  1.   2.    0.    0.     2.5    .5
59.   28.  60.   .65   1.25   1.25   7.0
30.7  1.   1.    0.    0.     0.5    .5
59.   28.  60.   .65   1.25   1.25   7.0
32.9  1.   1.    0.    0.     1.5    .5
59.   28.  60.   .65   1.25   1.25   7.0
40.   1.   0.    0.    0.     0.5    .5
```

APPENDIX B

INPUT AND OUTPUT FILES IN THE NORMOD CODE

Table B.1 The file with full input parameters in NORMOD input program for ^{60}Ni(^{3}He, t) reaction as described in Table 3.2. The outputs are One-body transition densities (OBTDs).

```
1
14
1 1  3 1.0 1 3 10
0 3  5 1.0 1 3 11
1 1  1 1.0 1 3 12
0 4  9 1.0 1 4 13
0 4  7 1.0 1 4 14
1 2  5 1.0 1 4 15
1 2  3 1.0 1 4 16
2 0  1 1.0 1 4 17
0 5 11 1.0 1 5 18
0 5  9 1.0 1 5 19
1 3  7 1.0 1 5 20
1 3  5 1.0 1 5 21
2 1  3 1.0 1 5 22
2 1  1 1.0 1 5 23
11
0 0  1 1.0 0 0 1
0 1  3 1.0 0 1 2
0 1  1 1.0 0 1 3
0 2  5 1.0 0 2 4
1 0  1 1.0 0 2 5
0 2  3 1.0 0 2 6
0 3  7 1.0 0 3 7
1 1  3 1.0 0 3 8
0 3  5 0.0 0 3 9
1 1  1 0.0 0 3 10
0 4  9 0.0 0 4 11
0 0  1 60 1  1 0 0
```

Table B.2 The file with full input parameters in NORMOD input program.

```
 0 1  1 60 1  1 0 0
 0 0 -1 60 1  1 1 1
 0 1 -1 60 1  1 1 1
 0 2 -1 60 1  1 1 1
 0 2  1 60 1  1 0 2
 0 1  1 60 1  1 0 2
 0 2  1 60 1  1 0 2
 0 3  1 60 1  1 0 2
 2 0  1 60 1  1 2 2
 2 1  1 60 1  1 2 2
 0 3 -1 60 1  1 1 1
```

Table B.3 The OBTDs for IAS , $\Delta J = 0^+$. P stand for proton and H is hole (neutron). The NP stand for principle quantum (n) number of a single-particle (proton), LP is the orbital quantum number of particle, 2JP is twice total angular momentum of particle and LP, 2JH have the same meaning but for hole (neutron). TYPE =1, for proton and 0 for neutron.

NP	LP	2JP	TYPE	NH	LH	2JH	TYPE	S=0 L=0	S= 1 L=-1	S=1 L=0	S=1 L=1
1	1	3	1	1	1	3	0	-1.0000	0.0000	0.0000	0.0000
0	3	5	1	0	3	5	0	-0.0000	0.0000	0.0000	0.0000
1	1	1	1	1	1	1	0	-0.0000	0.0000	0.0000	0.0000
0	4	9	1	0	4	9	0	-0.0000	0.0000	0.0000	0.0000

Table B.4 The OBTDs for Gamow-Teller transition, $\Delta J = 1^+$.

NP	LP	2JP	TYPE	NH	LH	2JH	TYPE	S=0 L=1	S=1 L=0	S=1 L=1	S=1 L=2
1	1	3	1	1	1	3	0	0.0000	-0.5092	0.0000	-0.2267
1	1	3	1	0	3	5	0	0.0000	-0.0000	0.0000	-0.0000
1	1	3	1	1	1	1	0	0.0000	0.0000	0.0000	-0.0000
0	3	5	1	0	3	7	0	0.0000	-0.7303	0.0000	0.4064
0	3	5	1	1	1	3	0	0.0000	-0.0000	0.0000	0.8481
0	3	5	1	0	3	5	0	0.0000	0.0000	0.0000	0.0000
1	1	1	1	1	1	3	0	0.0000	-0.4554	0.0000	0.2534
1	1	1	1	1	1	1	0	0.0000	0.0000	0.0000	0.0000
0	4	9	1	0	4	9	0	0.0000	-0.0000	0.0000	-0.0000
0	4	7	1	0	4	9	0	0.0000	-0.0000	0.0000	0.0000

Table B.5 The OBTDs for dipole transition, $\Delta J = 0^-$.

NP	LP	2JP	TYPE	NH	LH	2JH	TYPE	S=0 L=0	S=1 L=-1	S=1 L=0	S=1 L=1
1	1	3	1	0	2	3	0	0.0000	0.0000	0.0000	0.2236
0	3	5	1	0	2	5	0	0.0000	0.0000	0.0000	-0.5123
1	1	1	1	1	0	1	0	0.0000	0.0000	0.0000	0.2500
0	4	7	1	0	3	7	0	0.0000	0.0000	0.0000	-0.6708
1	2	5	1	0	3	5	0	0.0000	0.0000	0.0000	0.0000
1	2	3	1	1	1	3	0	0.0000	0.0000	0.0000	-0.4183
2	0	1	1	1	1	1	0	0.0000	0.0000	0.0000	0.0000
0	5	9	1	0	4	9	0	0.0000	0.0000	0.0000	-0.0000

Table B.6 The OBTDs for dipole transition, $\Delta J = 1^-$, where values of states with $\Delta S = 1$, $\Delta L = 1$ and $\Delta S = 0$, $\Delta L = 1$ were used.

NP	LP	2JP	TYPE	NH	LH	2JH	TYPE	S=0 L=1	S=1 L=0	S=1 L=1	S=1 L=2
1	1	3	1	0	2	5	0	-0.2108	0.0000	-0.1338	0.0000
1	1	3	1	1	0	1	0	-0.2485	0.0000	0.1577	0.0000
1	1	3	1	0	2	3	0	-0.0703	0.0000	0.1784	0.0000
0	3	5	1	0	2	5	0	0.1054	0.0000	0.4015	0.0000
0	3	5	1	0	2	3	0	-0.3944	0.0000	-0.2504	0.0000
1	1	1	1	1	0	1	0	0.1757	0.0000	0.2230	0.0000
1	1	1	1	0	2	3	0	-0.1571	0.0000	0.0998	0.0000
0	4	9	1	0	3	7	0	-0.6086	0.0000	0.3863	0.0000
0	4	7	1	0	3	7	0	0.1029	0.0000	0.5224	0.0000
0	4	7	1	0	3	5	0	-0.0000	0.0000	-0.0000	0.0000
1	2	5	1	0	3	7	0	-0.2520	0.0000	-0.1600	0.0000
1	2	5	1	1	1	3	0	-0.3944	0.0000	0.2504	0.0000
1	2	5	1	0	3	5	0	-0.0000	0.0000	0.0000	0.0000
1	2	3	1	1	1	3	0	0.1315	0.0000	0.3338	0.0000
1	2	3	1	0	3	5	0	-0.0000	0.0000	0.0000	0.0000
1	2	3	1	1	1	1	0	-0.0000	0.0000	-0.0000	0.0000
2	0	1	1	1	1	3	0	-0.2222	0.0000	-0.1411	0.0000
2	0	1	1	1	1	1	0	-0.0000	0.0000	0.0000	0.0000
0	5	11	1	0	4	9	0	-0.0000	0.0000	0.0000	0.0000
0	5	9	1	0	4	9	0	0.0000	0.0000	0.0000	0.0000
1	3	7	1	0	4	9	0	-0.0000	0.0000	-0.0000	0.0000

Table B.7 The OBTDs for dipole transition, $\Delta J = 2^-$ ($\Delta L = 1$).

NP	LP	2JP	TYPE	NH	LH	2JH	TYPE	S=0 L=2	S=1 L=1	S=1 L=2	S=1 L=3
1	1	3	1	0	2	5	0	0.0000	-0.2024	0.0000	-0.0597
1	1	3	1	1	0	1	0	0.0000	-0.3492	0.0000	0.0000
1	1	3	1	0	2	3	0	0.0000	0.0883	0.0000	-0.1367
0	3	5	1	0	2	5	0	0.0000	-0.2164	0.0000	0.2152
0	3	5	1	1	0	1	0	0.0000	-0.0000	0.0000	0.3537
0	3	5	1	0	2	3	0	0.0000	0.1623	0.0000	0.2870
0	3	5	1	0	4	9	0	0.0000	0.0000	0.0000	-0.0000
1	1	1	1	0	2	5	0	0.0000	-0.2164	0.0000	0.0558
1	1	1	1	0	2	3	0	0.0000	0.0442	0.0000	0.2734
0	4	9	1	0	3	7	0	0.0000	-0.4795	0.0000	-0.2120
0	4	9	1	0	3	5	0	0.0000	0.0000	0.0000	-0.0000
0	4	7	1	0	3	7	0	0.0000	-0.2892	0.0000	0.3515
0	4	7	1	1	1	3	0	0.0000	0.0000	0.0000	0.6213
0	4	7	1	0	3	5	0	0.0000	0.0000	0.0000	0.0000
1	2	5	1	0	3	7	0	0.0000	-0.2125	0.0000	-0.1252
1	2	5	1	1	1	3	0	0.0000	-0.3787	0.0000	-0.1036
1	2	5	1	0	3	5	0	0.0000	0.0000	0.0000	-0.0000
1	2	5	1	1	1	1	0	0.0000	0.0000	0.0000	-0.0000
1	2	3	1	0	3	7	0	0.0000	-0.2833	0.0000	0.0939
1	2	3	1	1	1	3	0	0.0000	-0.1653	0.0000	0.2374
1	2	3	1	0	3	5	0	0.0000	0.0000	0.0000	0.0000
1	2	3	1	1	1	1	0	0.0000	0.0000	0.0000	0.0000
2	0	1	1	1	1	3	0	0.0000	-0.3123	0.0000	0.0000
2	0	1	1	0	3	5	0	0.0000	-0.0000	0.0000	-0.0000
0	5	11	1	0	4	9	0	0.0000	-0.0000	0.0000	-0.0000
0	5	9	1	0	4	9	0	0.0000	-0.0000	0.0000	0.0000
1	3	7	1	0	4	9	0	0.0000	-0.0000	0.0000	-0.0000
1	3	5	1	0	4	9	0	0.0000	-0.0000	0.0000	0.0000

Table B.8 The OBTDs for the IVGQR and IVSGQR transitions with $\Delta J = 2^+$.

NP	LP	2JP	TYPE	NH	LH	2JH	TYPE	S=0 L=2	S=1 L=1	S=1 L=2	S=1 L=3
1	1	3	1	0	1	3	0	-0.0746	0.0000	0.0000	0.0000
1	1	3	1	0	1	1	0	-0.0746	0.0000	0.0844	0.0000
1	1	3	1	0	3	7	0	0.2830	0.0000	0.2136	0.0000
1	1	3	1	1	1	3	0	0.2122	0.0000	-0.0000	0.0000
1	1	3	1	0	3	5	0	0.0000	0.0000	-0.0000	0.0000
1	1	3	1	1	1	1	0	0.0000	0.0000	-0.0000	0.0000
0	3	5	1	0	1	3	0	0.0913	0.0000	0.1724	0.0000
0	3	5	1	0	1	1	0	-0.1709	0.0000	-0.1290	0.0000
0	3	5	1	0	3	7	0	-0.1134	0.0000	-0.2997	0.0000
0	3	5	1	1	1	3	0	-0.1155	0.0000	-0.2180	0.0000
0	3	5	1	0	3	5	0	0.0000	0.0000	-0.0000	0.0000
0	3	5	1	1	1	1	0	0.0000	0.0000	0.0000	0.0000
1	1	1	1	0	1	3	0	0.0746	0.0000	0.0844	0.0000
1	1	1	1	1	1	3	0	-0.2122	0.0000	-0.2403	0.0000
1	1	1	1	0	3	5	0	0.0000	0.0000	-0.0000	0.0000
0	4	9	1	0	2	5	0	-0.3537	0.0000	0.2670	0.0000
0	4	9	1	0	4	9	0	0.0000	0.0000	-0.0000	0.0000
0	4	7	1	0	2	5	0	0.1001	0.0000	0.2643	0.0000
0	4	7	1	0	2	3	0	-0.3002	0.0000	-0.2266	0.0000
0	4	7	1	0	4	9	0	-0.0000	0.0000	-0.0000	0.0000
1	2	5	1	0	2	5	0	-0.1155	0.0000	-0.0000	0.0000
1	2	5	1	1	0	1	0	-0.1709	0.0000	0.1290	0.0000
1	2	5	1	0	2	3	0	-0.0578	0.0000	0.1090	0.0000
1	2	5	1	0	4	9	0	0.0000	0.0000	0.0000	0.0000
1	2	3	1	0	2	5	0	0.0578	0.0000	0.1090	0.0000
1	2	3	1	1	0	1	0	0.1395	0.0000	0.1580	0.0000
1	2	3	1	0	2	3	0	-0.0882	0.0000	-0.0000	0.0000
2	0	1	1	0	2	5	0	-0.0817	0.0000	-0.0617	0.0000
2	0	1	1	0	2	3	0	-0.0667	0.0000	0.0755	0.0000
0	5	11	1	0	3	7	0	-0.5003	0.0000	0.3776	0.0000
0	5	9	1	0	3	7	0	0.1092	0.0000	0.3708	0.0000
0	5	9	1	0	3	5	0	-0.0000	0.0000	-0.0000	0.0000
1	3	7	1	0	3	7	0	-0.1544	0.0000	-0.0000	0.0000
1	3	7	1	1	1	3	0	-0.3002	0.0000	0.2266	0.0000
1	3	7	1	0	3	5	0	-0.0000	0.0000	0.0000	0.0000

Table B.9 The OBTDs for the IVGQR and IVSGQR transitions with $\Delta J = 2^+$ continuation.

1	3	5	1	0	3	7	0	0.0535	0.0000	0.1413	0.0000
1	3	5	1	1	1	3	0	0.1225	0.0000	0.2312	0.0000
1	3	5	1	0	3	5	0	-0.0000	0.0000	0.0000	0.0000
1	3	5	1	1	1	1	0	-0.0000	0.0000	-0.0000	0.0000
2	1	3	1	0	3	7	0	-0.1070	0.0000	-0.0807	0.0000
2	1	3	1	1	1	3	0	-0.1248	0.0000	0.0000	0.0000
2	1	3	1	0	3	5	0	-0.0000	0.0000	0.0000	0.0000
2	1	3	1	1	1	1	0	-0.0000	0.0000	0.0000	0.0000
2	1	1	1	1	1	3	0	0.1248	0.0000	0.1413	0.0000
2	1	1	1	0	3	5	0	-0.0000	0.0000	0.0000	0.0000

Table B.10 The OBTDs for the IVSGQR transition, $\Delta J = 1^+$.

NP	LP	2JP	TYPE	NH	LH	2JH	TYPE	S=0 L=1	S=1 L=0	S=1 L=1	S=1 L=2
1	1	3	1	0	1	3	0	0.0000	-0.0000	0.0000	0.0314
1	1	3	1	0	1	1	0	0.0000	0.0000	0.0000	0.0351
1	1	3	1	1	1	3	0	0.0000	-0.5092	0.0000	-0.0894
1	1	3	1	0	3	5	0	0.0000	-0.0000	0.0000	-0.0000
1	1	3	1	1	1	1	0	0.0000	0.0000	0.0000	-0.0000
0	3	5	1	0	1	3	0	0.0000	0.0000	0.0000	-0.2644
0	3	5	1	0	3	7	0	0.0000	-0.7303	0.0000	0.1603
0	3	5	1	1	1	3	0	0.0000	-0.0000	0.0000	0.3345
0	3	5	1	0	3	5	0	0.0000	0.0000	0.0000	0.0000
1	1	1	1	0	1	3	0	0.0000	-0.0000	0.0000	-0.0351
1	1	1	1	0	1	1	0	0.0000	0.0000	0.0000	-0.0993
1	1	1	1	1	1	3	0	0.0000	-0.4554	0.0000	0.0999
1	1	1	1	1	1	1	0	0.0000	0.0000	0.0000	0.0000
0	4	9	1	0	4	9	0	0.0000	-0.0000	0.0000	-0.0000
0	4	7	1	0	2	5	0	0.0000	-0.0000	0.0000	-0.4240
0	4	7	1	0	4	9	0	0.0000	-0.0000	0.0000	0.0000
1	2	5	1	0	2	5	0	0.0000	0.0000	0.0000	0.0596
1	2	5	1	0	2	3	0	0.0000	-0.0000	0.0000	0.0557
1	2	3	1	0	2	5	0	0.0000	0.0000	0.0000	-0.0557
1	2	3	1	1	0	1	0	0.0000	-0.0000	0.0000	-0.1971
1	2	3	1	0	2	3	0	0.0000	-0.0000	0.0000	-0.1115
2	0	1	1	1	0	1	0	0.0000	0.0000	0.0000	0.0000
2	0	1	1	0	2	3	0	0.0000	-0.0000	0.0000	0.0942
0	5	9	1	0	3	7	0	0.0000	0.0000	0.0000	-0.6051
1	3	7	1	0	3	7	0	0.0000	0.0000	0.0000	0.0872
1	3	7	1	0	3	5	0	0.0000	-0.0000	0.0000	0.0000
1	3	5	1	0	3	7	0	0.0000	0.0000	0.0000	-0.0755
1	3	5	1	1	1	3	0	0.0000	0.0000	0.0000	-0.3547
1	3	5	1	0	3	5	0	0.0000	-0.0000	0.0000	-0.0000
2	1	3	1	1	1	3	0	0.0000	-0.0000	0.0000	0.0526
2	1	3	1	0	3	5	0	0.0000	0.0000	0.0000	0.0000
2	1	3	1	1	1	1	0	0.0000	0.0000	0.0000	0.0000
2	1	1	1	1	1	3	0	0.0000	-0.0000	0.0000	-0.0588
2	1	1	1	1	1	1	0	0.0000	0.0000	0.0000	-0.0000

Table B.11 The OBTDs for IVSGQR transition, $\Delta J = 3^+$ ($\Delta L = 2$).

NP	LP	2JP	TYPE	NH	LH	2JH	TYPE	S=0 L=3	S=1 L=2	S=1 L=3	S=1 L=4
1	1	3	1	0	1	3	0	0.0000	-0.1321	0.0000	-0.0000
1	1	3	1	0	3	7	0	0.0000	0.2445	0.0000	0.0541
1	1	3	1	1	1	3	0	0.0000	0.3758	0.0000	0.0000
1	1	3	1	0	3	5	0	0.0000	-0.0000	0.0000	0.0000
0	3	5	1	0	1	3	0	0.0000	-0.0576	0.0000	0.0956
0	3	5	1	0	1	1	0	0.0000	0.0322	0.0000	0.1710
0	3	5	1	0	3	7	0	0.0000	0.2264	0.0000	-0.1377
0	3	5	1	1	1	3	0	0.0000	0.0729	0.0000	-0.1814
0	3	5	1	0	3	5	0	0.0000	-0.0000	0.0000	-0.0000
0	3	5	1	1	1	1	0	0.0000	-0.0000	0.0000	-0.0000
1	1	1	1	0	3	7	0	0.0000	0.2823	0.0000	-0.0468
1	1	1	1	0	3	5	0	0.0000	-0.0000	0.0000	-0.0000
0	4	9	1	0	2	5	0	0.0000	-0.2617	0.0000	-0.0772
0	4	9	1	0	2	3	0	0.0000	0.3866	0.0000	-0.0522
0	4	9	1	0	4	9	0	0.0000	0.0000	0.0000	0.0000
0	4	7	1	0	2	5	0	0.0000	-0.0998	0.0000	0.2023
0	4	7	1	1	0	1	0	0.0000	0.0000	0.0000	0.3258
0	4	7	1	0	2	3	0	0.0000	0.0865	0.0000	0.2337
0	4	7	1	0	4	9	0	0.0000	0.0000	0.0000	-0.0000
1	2	5	1	0	2	5	0	0.0000	-0.1339	0.0000	-0.0395
1	2	5	1	1	0	1	0	0.0000	-0.2255	0.0000	-0.0000
1	2	5	1	0	2	3	0	0.0000	0.0729	0.0000	-0.0725
1	2	5	1	0	4	9	0	0.0000	0.0000	0.0000	0.0000
1	2	3	1	0	2	5	0	0.0000	-0.0729	0.0000	0.0725
1	2	3	1	0	2	3	0	0.0000	0.0223	0.0000	0.2369
1	2	3	1	0	4	9	0	0.0000	0.0000	0.0000	-0.0000
2	0	1	1	0	2	5	0	0.0000	-0.1078	0.0000	0.0000
0	5	11	1	0	3	7	0	0.0000	-0.3401	0.0000	-0.1504
0	5	11	1	0	3	5	0	0.0000	0.0000	0.0000	-0.0000
0	5	9	1	0	3	7	0	0.0000	-0.1461	0.0000	0.3501
0	5	9	1	1	1	3	0	0.0000	-0.0000	0.0000	0.6238
0	5	9	1	0	3	5	0	0.0000	0.0000	0.0000	0.0000
1	3	7	1	0	3	7	0	0.0000	-0.1533	0.0000	-0.0904
1	3	7	1	1	1	3	0	0.0000	-0.2594	0.0000	-0.0722
1	3	7	1	0	3	5	0	0.0000	0.0000	0.0000	-0.0000

Table B.12 The OBTDs for IVSGQR transition, $\Delta J = 3^+$ ($\Delta L = 2$) Continuation.

1	3	5	1	0	3	7	0	0.0000	-0.1067	0.0000	0.1298
1	3	5	1	1	1	3	0	0.0000	-0.0773	0.0000	0.2422
2	1	3	1	0	3	7	0	0.0000	-0.0924	0.0000	-0.0409
2	1	3	1	1	1	3	0	0.0000	-0.2210	0.0000	-0.0000
2	1	1	1	0	3	7	0	0.0000	-0.1067	0.0000	0.0354

Table B.13 The OBTDs for IVGMR transition, $\Delta J = 0^+$, where only values of state with $\Delta S = 0$ and $\Delta L = 0$ was used.

NP	LP	2JP	TYPE	NH	LH	2JH	TYPE	S=0 L=0	S=1 L=-1	S=1 L=0	S=1 L=1
1	1	3	1	0	1	3	0	0.2840	0.0000	0.0000	0.0000
1	1	1	1	0	1	1	0	0.2008	0.0000	0.0000	0.0000
1	2	5	1	0	2	5	0	0.4115	0.0000	0.0000	0.0000
1	2	3	1	0	2	3	0	0.3360	0.0000	0.0000	0.0000
2	0	1	1	1	0	1	0	0.2840	0.0000	0.0000	0.0000
1	3	7	1	0	3	7	0	0.5388	0.0000	0.0000	0.0000
1	3	5	1	0	3	5	0	0.0000	0.0000	0.0000	0.0000
2	1	3	1	1	1	3	0	0.4752	0.0000	0.0000	0.0000
2	1	1	1	1	1	1	0	0.0000	0.0000	0.0000	0.0000

Table B.14 The OBTDs for IVSGMR transition, $\Delta J = 1^+$.

NP	LP	2JP	TYPE	NH	LH	2JH	TYPE	S=0 L=1	S=1 L=0	S=1 L=1	S=1 L=2
1	1	3	1	0	1	3	0	0.0000	0.2117	0.0000	0.0350
1	1	3	1	0	1	1	0	0.0000	-0.1893	0.0000	0.0392
0	3	5	1	0	1	3	0	0.0000	0.0000	0.0000	-0.1896
1	1	1	1	0	1	3	0	0.0000	0.1893	0.0000	-0.0392
1	1	1	1	0	1	1	0	0.0000	-0.0669	0.0000	-0.1108
0	4	7	1	0	2	5	0	0.0000	-0.0000	0.0000	-0.3715
1	2	5	1	0	2	5	0	0.0000	0.2811	0.0000	0.0854
1	2	5	1	0	2	3	0	0.0000	-0.3005	0.0000	0.0799
1	2	3	1	0	2	5	0	0.0000	0.3005	0.0000	-0.0799
1	2	3	1	1	0	1	0	0.0000	-0.0000	0.0000	-0.2355
1	2	3	1	0	2	3	0	0.0000	-0.1503	0.0000	-0.1599
2	0	1	1	1	0	1	0	0.0000	0.2840	0.0000	0.0000
2	0	1	1	0	2	3	0	0.0000	-0.0000	0.0000	0.1576
0	5	9	1	0	3	7	0	0.0000	0.0000	0.0000	-0.6267
1	3	7	1	0	3	7	0	0.0000	0.3527	0.0000	0.1529
1	3	7	1	0	3	5	0	0.0000	-0.0000	0.0000	0.0000
1	3	5	1	0	3	7	0	0.0000	0.4073	0.0000	-0.1324
1	3	5	1	1	1	3	0	0.0000	0.0000	0.0000	-0.4804
1	3	5	1	0	3	5	0	0.0000	-0.0000	0.0000	-0.0000
2	1	3	1	1	1	3	0	0.0000	0.3542	0.0000	0.0921
2	1	3	1	0	3	5	0	0.0000	0.0000	0.0000	0.0000
2	1	3	1	1	1	1	0	0.0000	-0.0000	0.0000	0.0000
2	1	1	1	1	1	3	0	0.0000	0.3168	0.0000	-0.1030
2	1	1	1	1	1	1	0	0.0000	-0.0000	0.0000	-0.0000

Table B.15 The OBTDs for the IVSGOR and IVGOR with $\Delta J = 3^-$.

NP	LP	2JP	TYPE	NH	LH	2JH	TYPE	S=0 L=3	S=1 L=2	S=1 L=3	S=1 L=4
1	1	3	1	0	2	5	0	0.1606	0.0000	0.0466	0.0000
1	1	3	1	0	2	3	0	0.1967	0.0000	-0.2281	0.0000
1	1	3	1	0	4	9	0	-0.0000	0.0000	-0.0000	0.0000
0	3	5	1	0	2	5	0	-0.1577	0.0000	-0.2744	0.0000
0	3	5	1	1	0	1	0	-0.2277	0.0000	-0.2640	0.0000
0	3	5	1	0	2	3	0	0.1932	0.0000	0.0560	0.0000
0	3	5	1	0	4	9	0	0.0000	0.0000	0.0000	0.0000
1	1	1	1	0	2	5	0	-0.1796	0.0000	-0.2083	0.0000
0	4	9	1	0	3	7	0	0.4037	0.0000	-0.1170	0.0000
0	4	9	1	1	1	3	0	0.4554	0.0000	-0.3960	0.0000
0	4	9	1	0	3	5	0	0.0000	0.0000	-0.0000	0.0000
0	4	7	1	0	3	7	0	-0.1805	0.0000	-0.4186	0.0000
0	4	7	1	1	1	3	0	-0.2037	0.0000	-0.3542	0.0000
0	4	7	1	0	3	5	0	0.0000	0.0000	0.0000	0.0000
0	4	7	1	1	1	1	0	0.0000	0.0000	0.0000	0.0000
1	2	5	1	0	3	7	0	0.2666	0.0000	0.0773	0.0000
1	2	5	1	1	1	3	0	0.2791	0.0000	-0.0809	0.0000
1	2	5	1	0	3	5	0	0.0000	0.0000	-0.0000	0.0000
1	2	5	1	1	1	1	0	0.0000	0.0000	-0.0000	0.0000
1	2	3	1	0	3	7	0	-0.1539	0.0000	-0.2678	0.0000
1	2	3	1	1	1	3	0	-0.3418	0.0000	-0.3963	0.0000
1	2	3	1	0	3	5	0	0.0000	0.0000	-0.0000	0.0000
2	0	1	1	0	3	7	0	0.2352	0.0000	0.2045	0.0000
2	0	1	1	0	3	5	0	0.0000	0.0000	-0.0000	0.0000
0	5	11	1	0	4	9	0	0.0000	0.0000	-0.0000	0.0000
0	5	9	1	0	4	9	0	-0.0000	0.0000	-0.0000	0.0000
1	3	7	1	0	4	9	0	0.0000	0.0000	0.0000	0.0000
1	3	5	1	0	4	9	0	-0.0000	0.0000	-0.0000	0.0000
2	1	3	1	0	4	9	0	0.0000	0.0000	0.0000	0.0000

APPENDIX C

FULL INPUT FILES IN THE FOLD CODE

Table C.1 The file with full input parameters in FOLD input program for GT transition as described in Table 3.3.

```
    1    1FOLDNIB
  600 0.03      420.         3.          1   1   1
      0.5+      0.5+
  0.5      +0.5        0.5      -0.5
    3    3  0.000
    1    1    1  0.0       0.707
   -1   -1
HE3H3
      1.0+      0.0+
  1.0      1.0       2.0       2.0
    3    3  0.000
    8    8    1  0.0       -0.5092
    9   10    1  0.0       -0.7303
    7    8    1  0.0       -0.4554
  -1   -1
Ni60Cu60
 0.939     2.650     1.000    love_140
    2
    0    1    1   -1
 1.00      1.00      1.00     1.00     1.00     1.00     1.00
 1.00      1.00      1.00     1.00     1.00     1.00     1.00
    2    1    1   -1
 1.00      1.00      1.00     1.00     1.00     1.00     1.00
 1.00      1.00      1.00     1.00     1.00     1.00     1.00
```

Table C.2 The file with full input parameters in FOLD input program for IAS as described in Table 3.3.

```
    1    1FOLDNIA
  600 0.03      420.         3.          1   1   1
      0.5+      0.5+
  0.5      +0.5        0.5      -0.5
    3    3  0.000
    1    1    0  0.0       0.707
   -1   -1
HE3H3
      0.0+      0.0+
  2.0      1.0       2.0       2.0
    3    3  0.000
    8    8    0  0.0       -1.0
  -1   -1
Ni60Cu60
 0.939     2.650     1.000    love_140
    1
    0    0    0   -1
 1.00      1.00      1.00     1.00     1.00     1.00     1.00
 1.00      1.00      1.00     1.00     1.00     1.00     1.00
```

Table C.3 The file with full input parameters in the FOLD input program for IVSGDR with $\Delta J = 1, \Delta S = 1$ as described in Table 3.3.

```
    1    1FOLDNIE
  600 0.03      420.         3.          1   1   1
      0.5+      0.5+
  0.5      +0.5        0.5      -0.5
    3    3  0.000
    1    1    1  0.0       0.707
   -1   -1
HE3H3
       1.0-      0.0+
  1.0      1.0       2.0       2.0
    3    3  0.000
    8    6    1  0.0       -0.1338
    8    4    1  0.0        0.1577
    8    5    1  0.0        0.1784
    9    6    1  0.0        0.4015
    9    5    1  0.0       -0.2504
    7    4    1  0.0        0.2230
    7    5    1  0.0        0.0998
   15   10    1  0.0        0.3863
   14   10    1  0.0        0.5224
   13   10    1  0.0       -0.1600
   13    8    1  0.0        0.2504
   12    8    1  0.0        0.3338
   11    8    1  0.0       -0.1411
  -1   -1
Ni60Cu60
 0.939     2.650     1.000    love_140
    1
    1    1    1   -1
 1.00      1.00      1.00     1.00     1.00     1.00     1.00
 1.00      1.00      1.00     1.00     1.00     1.00     1.00
```

Table C.4 The file with full input parameters in FOLD input program for IVSGQR with ΔJ = 3 as described in Table 3.3.

```
    1    1FOLDNIM
  600 0.03      420.         3.          1   1   1
      0.5+      0.5+
  0.5      +0.5        0.5      -0.5
    3    3  0.000
    1    1    1  0.0       0.707
   -1   -1
HE3H3
       3.0+      0.0+
  1.0      1.0       2.0       2.0
    3    3  0.000
    8    3    3  0.0       -0.1321
    8   10    3  0.0        0.2445
    8    8    3  0.0        0.3758
    9    3    3  0.0       -0.0576
    9    2    3  0.0        0.0322
    9   10    3  0.0        0.2264
    9    8    3  0.0        0.0729
    7   10    3  0.0        0.2823
   15    6    3  0.0       -0.2617
   15    5    3  0.0        0.3866
   14    6    3  0.0       -0.0998
   14    5    3  0.0        0.0865
   13    6    3  0.0       -0.1339
   13    4    3  0.0       -0.2255
   13    5    3  0.0        0.0729
   12    6    3  0.0       -0.0729
   .     .    .  .             .
   .     .    .  .             .
  -1   -1
Ni60Cu60
 0.939     2.650     1.000    love_140
    1
    2    1    3   -1
 1.00      1.00      1.00     1.00     1.00     1.00     1.00
 1.00      1.00      1.00     1.00     1.00     1.00     1.00
```

Table C.5 The file with full input parameters in FOLD input program for IVGMR as described in Table 3.3.

```
    1    1FOLDNIN
  600 0.03      420.         3.          1   1   1
      0.5+      0.5+
  0.5      +0.5        0.5      -0.5
    3    3  0.000
    1    1    0  0.0       0.707
   -1   -1
HE3H3
      0.0+      0.0+
  1.0      1.0       2.0       2.0
    3    3  0.000
    8    3    0  0.0        0.2840
    7    2    0  0.0        0.2008
   13    6    0  0.0        0.4115
   12    5    0  0.0        0.3360
   11    4    0  0.0        0.2840
   19   10    0  0.0        0.5388
   17    8    0  0.0        0.4752
  -1   -1
Ni60Cu60
 0.939     2.650     1.000    love_140
    1
    0    0    0   -1
 1.00      1.00      1.00     1.00     1.00     1.00     1.00
 1.00      1.00      1.00     1.00     1.00     1.00     1.00
```

Table C.6 The file with full input parameters in FOLD input program for IVSGMR as described in Table 3.3.

```
    1    1FOLDNIO
  600 0.03      420.         3.          1   1   1
      0.5+      0.5+
  0.5      +0.5        0.5      -0.5
    3    3  0.000
    1    1    1  0.0       0.707
   -1   -1
HE3H3
      1.0+      0.0+
  1.0      1.0       2.0       2.0
    3    3  0.000
    8    3    1  0.0        0.2117
    8    2    1  0.0       -0.1893
    7    3    1  0.0        0.1893
    7    2    1  0.0       -0.0669
   13    6    1  0.0        0.2811
   13    5    1  0.0       -0.3005
   12    6    1  0.0        0.3005
   12    5    1  0.0       -0.1503
   11    4    1  0.0        0.2840
   19   10    1  0.0        0.3527
   18   10    1  0.0        0.4073
   17    8    1  0.0        0.3542
   16    8    1  0.0        0.3168
  -1   -1
Ni60Cu60
 0.939     2.650     1.000    love_140
    2
    0    1    1   -1
 1.00      1.00      1.00     1.00     1.00     1.00     1.00
 1.00      1.00      1.00     1.00     1.00     1.00     1.00
    2    1    1   -1
 1.00      1.00      1.00     1.00     1.00     1.00     1.00
 1.00      1.00      1.00     1.00     1.00     1.00     1.00
```

Table C.7 The file with full input parameters in FOLD input program for IVSGOR with $\Delta J = 3, \Delta S = 1$ transition as described in Table 3.3.

```
    1    1FOLDNIP
  600 0.03      420.         3.          1   1   1
      0.5+      0.5+
  0.5      +0.5        0.5      -0.5
    3    3  0.000
    1    1    1  0.0       0.707
   -1   -1
HE3H3
       3.0-      0.0+
  1.0      1.0       2.0       2.0
    3    3  0.000
    8    6    3  0.0        0.0466
    8    5    3  0.0       -0.2281
    9    6    3  0.0       -0.2744
    9    4    3  0.0       -0.2640
    9    5    3  0.0        0.0560
    7    6    3  0.0       -0.2083
   15   10    3  0.0       -0.1170
   15    8    3  0.0       -0.3960
   14   10    3  0.0       -0.4186
   14    8    3  0.0       -0.3542
   13   10    3  0.0        0.0773
   13    8    3  0.0       -0.0809
   12   10    3  0.0       -0.2678
   12    8    3  0.0       -0.3963
   11   10    3  0.0        0.2045
  -1   -1
Ni60Cu60
 0.939     2.650     1.000    love_140
    1
    3    1    3   -1
 1.00      1.00      1.00     1.00     1.00     1.00     1.00
 1.00      1.00      1.00     1.00     1.00     1.00     1.00
```

APPENDIX D

FULL INPUT FILES IN THE DWHI CODE

Table D.1 The file with full input parameters in DWHI input program for IAS transition as described in Table 3.6.

```
1210000041000000    MG26(C,B) STATE 1 ROUSSEL-CHOMAZ (O+SI) POTL
FOLDNIA
  40.    0.     0.2
160  1  1  1  0  0
 0.03    600
 420.   3.    2.     60.    28.   1.25   1.     0.
 1.     -35.16 1.32   0.84   0.    -44.43 1.021  1.018  0.   0.
 0.
 -6.2   3.    1.     60.    29.   1.25   1.     0.
 1.     -29.89 1.32   0.84   0.    -37.77 1.021  1.018  0.   0.
 0.
  0  0  0
 0.     0.     0.     1.
IAS.plot
```

Table D.2 The file with full input parameters in DWHI input program for GT transition as described in Table 3.3.

```
210000041000000    MG26(C,B) STATE 1 ROUSSEL-CHOMAZ (O+SI) POTL
FOLDNIB
  40.    0.     0.2
160  2  1  1  0  2
 0.03    600
 420.   3.    2.     60.    28.   1.25   1.     0.
 1.     -35.16 1.32   0.84   0.    -44.43 1.021  1.018  0.   0.
 0.
 -6.2   3.    1.     60.    29.   1.25   1.     0.
 1.     -29.89 1.32   0.84   0.    -37.77 1.021  1.018  0.   0.
 0.
  0  2  2
 0.     0.     0.     1.
  2  2  2
 0.     0.     0.     1.
GTA.plot
```

Table D.3 The file with full input parameters in DWHI input program for IVGMR with $\Delta J = 0, \Delta S = 0$ transition as described in Table 3.3.

```
1210000041000000    MG26(C,B) STATE 1 ROUSSEL-CHOMAZ (O+SI) POTL
FOLDNIN
  40.    0.     0.2
160  1  1  1  0  0
 0.03    600
 420.   3.    2.     60.    28.    1.25   1.     0.
 1.    -35.16  1.32   0.84   0.    -44.43 1.021  1.018   0.   0.
 0.
 -6.2   3.    1.     60.    29.    1.25   1.     0.
 1.    -29.89  1.32   0.84   0.    -37.77 1.021  1.018   0.   0.
 0.
  0  0  0
 0.     0.     0.     1.
IVGMR.plot
```

Table D.4 The file with full input parameters in DWHI input program for IVSGMR with $\Delta J = 1$, $\Delta S = 1$ as described in Table 3.3.

```
1210000041000000    MG26(C,B) STATE 1 ROUSSEL-CHOMAZ (O+SI) POTL
FOLDNIO
  40.    0.     0.2
160  2  1  1  0  2
 0.03    600
 420.   3.    2.     60.    28.    1.25   1.     0.
 1.    -35.16  1.32   0.84   0.    -44.43 1.021  1.018   0.   0.
 0.
 -6.2   3.    1.     60.    29.    1.25   1.     0.
 1.    -29.89  1.32   0.84   0.    -37.77 1.021  1.018   0.   0.
 0.
  0  2  2
 0.     0.     0.     1.
  2  2  2
 0.     0.     0.     1.
IVSGMRa.plot
```

Table D.5 The file with full input parameters in DWHI input program for IVSGDR with ΔJ = 0, ΔS = 1 as described in Table 3.6.

```
1210000041000000    MG26(C,B) STATE 1 ROUSSEL-CHOMAZ (O+SI) POTL
FOLDNID
  40.    0.     0.2
160  1  1  1  0  0
 0.03    600
 420.   3.    2.     60.    28.    1.25   1.     0.
 1.    -35.16  1.32   0.84   0.    -44.43 1.021  1.018   0.   0.
 0.
 -6.2   3.    1.     60.    29.    1.25   1.     0.
 1.    -29.89  1.32   0.84   0.    -37.77 1.021  1.018   0.   0.
 0.
  1  2  0
 0.     0.     0.     1.
DT0.plot
```

Table D.6 The file with full input parameters in DWHI input program for IVSGDR with ΔJ = 1, ΔS = 1 as described in Table 3.6.

```
1210000041000000    MG26(C,B) STATE 1 ROUSSEL-CHOMAZ (O+SI) POTL
FOLDNIE
  40.    0.     0.2
160  1  1  1  0  2
 0.03    600
 420.   3.    2.     60.    28.    1.25   1.     0.
 1.    -35.16  1.32   0.84   0.    -44.43 1.021  1.018   0.   0.
 0.
 -6.2   3.    1.     60.    29.    1.25   1.     0.
 1.    -29.89  1.32   0.84   0.    -37.77 1.021  1.018   0.   0.
 0.
  1  2  2
 0.     0.     0.     1.
DT1A.plot
```

Table D.7 The file with full input parameters in DWHI input program for IVSGDR with ΔJ = 1, ΔS = 0 as described in Table 3.6.

```
1210000041000000    MG26(C,B) STATE 1 ROUSSEL-CHOMAZ (O+SI) POTL
FOLDNIF
  40.    0.     0.2
160  1  1  1  0  2
 0.03    600
 420.   3.    2.     60.    28.    1.25   1.     0.
 1.    -35.16  1.32   0.84   0.    -44.43 1.021  1.018   0.   0.
 0.
 -6.2   3.    1.     60.    29.    1.25   1.     0.
 1.    -29.89  1.32   0.84   0.    -37.77 1.021  1.018   0.   0.
 0.
  1  0  2
 0.     0.     0.     1.
DT1B.plot
```

Table D.8 The file with full input parameters in DWHI input program for IVSGDR with ΔJ = 2, ΔS = 1 as described in Table 3.6.

```
1210000041000000    MG26(C,B) STATE 1 ROUSSEL-CHOMAZ (O+SI) POTL
FOLDNIZ
  40.    0.     0.2
160  1  1  1  0  4
 0.03    600
 420.   3.    2.     60.    28.    1.25   1.     0.
 1.    -35.16  1.32   0.84   0.    -44.43 1.021  1.018   0.   0.
 0.
 -6.2   3.    1.     60.    29.    1.25   1.     0.
 1.    -29.89  1.32   0.84   0.    -37.77 1.021  1.018   0.   0.
 0.
  1  2  4
 0.     0.     0.     1.
DT2.plot
```

Table D.9 The file with full input parameters in DWHI input program for IVSGQR with ΔJ = 1, ΔS = 1 as described in Table 3.6.

```
1210000041000000    MG26(C,B) STATE 1 ROUSSEL-CHOMAZ (O+SI) POTL
FOLDNIJ
  40.    0.     0.2
160  1  1  1  0  2
 0.03    600
 420.   3.    2.     60.    28.    1.25   1.     0.
 1.    -35.16  1.32   0.84   0.    -44.43 1.021  1.018   0.   0.
 0.
 -6.2   3.    1.     60.    29.    1.25   1.     0.
 1.    -29.89  1.32   0.84   0.    -37.77 1.021  1.018   0.   0.
 0.
  2  2  2
 0.     0.     0.     1.
IVSGQR1.plot
```

Table D.10 The file with full input parameters in DWHI input program for IVSGQR with ΔJ = 2, ΔS = 1 as described in Table 3.6.

```
1210000041000000    MG26(C,B) STATE 1 ROUSSEL-CHOMAZ (O+SI) POTL
FOLDNIK
  40.    0.     0.2
160  1  1  1  0  4
 0.03    600
 420.   3.    2.     60.    28.    1.25   1.     0.
 1.    -35.16  1.32   0.84   0.    -44.43 1.021  1.018   0.   0.
 0.
 -6.2   3.    1.     60.    29.    1.25   1.     0.
 1.    -29.89  1.32   0.84   0.    -37.77 1.021  1.018   0.   0.
 0.
  2  2  4
 0.     0.     0.     1.
IVSGQR2a.plot
```

Table D.11 The file with full input parameters in DWHI input program for IVSGQR with ΔJ = 2, ΔS = 0 as described in Table 3.6.

```
1210000041000000    MG26(C,B) STATE 1 ROUSSEL-CHOMAZ (O+SI) POTL
FOLDNIG
  40.    0.     0.2
160  1  1  1  0  4
 0.03    600
 420.   3.    2.     60.    28.    1.25   1.     0.
 1.    -35.16  1.32   0.84   0.    -44.43 1.021  1.018   0.   0.
 0.
 -6.2   3.    1.     60.    29.    1.25   1.     0.
 1.    -29.89  1.32   0.84   0.    -37.77 1.021  1.018   0.   0.
 0.
  2  0  4
 0.     0.     0.     1.
IVGQRa.plot
```

Table D.12 The file with full input parameters in DWHI input program for IVSGQR with ΔJ = 3, ΔS = 1 as described in Table 3.6.

```
1210000041000000    MG26(C,B) STATE 1 ROUSSEL-CHOMAZ (O+SI) POTL
FOLDNIM
  40.    0.     0.2
160  1  1  1  0  6
 0.03    600
 420.   3.    2.     60.    28.    1.25   1.     0.
 1.    -35.16  1.32   0.84   0.    -44.43 1.021  1.018   0.   0.
 0.
 -6.2   3.    1.     60.    29.    1.25   1.     0.
 1.    -29.89  1.32   0.84   0.    -37.77 1.021  1.018   0.   0.
 0.
  2  2  6
 0.     0.     0.     1.
IVSGQR3.plot
```

Table D.13 The file with full input parameters in DWHI input program for IVGOR with ΔJ = 3, ΔS = 0 as described in Table 3.6.

```
1220000041000000    MG26(C,B) STATE 1 ROUSSEL-CHOMAZ (O+SI) POTL
FOLDNIL
  40.    0.     0.2
160  1  1  1  0  6
 0.03    600
 420.   3.    2.     60.    28.    1.25   1.     0.
 1.    -35.16  1.32   0.84   0.    -44.43 1.021  1.018   0.   0.
 0.
 -6.2   3.    1.     60.    29.    1.25   1.     0.
 1.    -29.89  1.32   0.84   0.    -37.77 1.021  1.018   0.   0.
 0.
  3  0  6
 0.     0.     0.     1.
Octupole3b.plot
```

Table D.14 The file with full input parameters in DWHI input program for IVSGOR with ΔJ = 3, ΔS = 1 as described in Table 3.6.

```
1220000041000000    MG26(C,B) STATE 1 ROUSSEL-CHOMAZ (O+SI) POTL
FOLDNIP
  40.    0.     0.2
160  1  1  1  0  6
 0.03    600
 420.   3.    2.     60.    28.    1.25   1.     0.
 1.    -35.16  1.32   0.84   0.    -44.43 1.021  1.018   0.   0.
 0.
 -6.2   3.    1.     60.    29.    1.25   1.     0.
 1.    -29.89  1.32   0.84   0.    -37.77 1.021  1.018   0.   0.
 0.
  3  2  6
 0.     0.     0.     1.
Octupole3a.plot
```

APPENDIX E

PROPORTIONALITY RELATION BETWEEN dp AND dk

We can show that $\frac{dp}{p} \approx \frac{dk}{2k}$: where p is the momentum and k is kinetic energy.

For $p = \sqrt{E^2 - m^2}$ and $E = k + m$

$$p = \sqrt{(k+m)^2 - m^2} = \sqrt{k^2 + 2km} \tag{E.1}$$

If **m** >> **k**, then: $p \approx \sqrt{2km} \implies m = \frac{p^2}{2k}$

$$\frac{dp}{dk} = \frac{2m}{2\sqrt{2km}} = \frac{m}{\sqrt{2km}} = \frac{p^2}{2kp} = \frac{p}{2k} \tag{E.2}$$

$$\frac{dp}{p} = \frac{dk}{2k} \tag{E.3}$$